Country-specific Ground-based Bistatic Radar Clutter Analysis of Rural Environments

Dissertation

der Mathematisch-Naturwissenschaftlichen Fakultät

der Eberhard Karls Universität Tübingen

zur Erlangung des Grades eines

Doktors der Naturwissenschaften

(Dr. rer. nat.)

vorgelegt von

M.Sc. Michael Kohler

aus Bühl

Tübingen

2020

Gedruckt mit Genehmigung der Mathematisch-Naturwissenschaftlichen Fakultät
der Eberhard Karls Universität Tübingen.

Tag der mündlichen Qualifikation: 26.03.2021
Stellvertretender Dekan: Prof. Dr. József Fortágh
1. Berichterstatter: Prof. Dr. Oliver Bringmann
2. Berichterstatter: Prof. Dr. Chris Baker

Ground-based Bistatic Radar Clutter Analysis of Rural Environments

Michael Kohler

A dissertation submitted in partial fulfillment

of the requirements for the degree of

Dr. rer. nat.

of

Eberhard Karls University of Tübingen.

Faculty of Science

Eberhard Karls University of Tübingen

2020

I, Michael Kohler, confirm that the work presented in this thesis is my own. Where information has been derived from other sources, I confirm that this has been indicated in the work.

Abstract

This thesis presents a novel statistical analysis of bistatic radar rural ground clutter for different terrain types of German rural environments under low grazing angles. A country-specific clutter analysis for subgroups of rural environments rather than for the rural environment as a whole will be presented. Therefore, the rural environment is divided into four dominant subgroup terrain types, namely fields with low vegetation, fields with high vegetation, plantations of small trees and forest environments, representing a typical rural German or even Central European environment. The thesis will present the bistatic clutter characteristics for both the summer and the winter vegetation. Therefore, bistatic measurement campaigns have been carried out during the summer 2019 and the winter of 2019/20 in the aforementioned four different rural terrain types. The measurements were carried out according to a designed bistatic measurement methodology to obtain comparable results and to be used for different radar applications in the radar relevant X-band at a center frequency of 8.85 GHz and over a bandwidth of 100 MHz, according to available transmit permissions. The distinction of the rural terrain into different subgroups enables a more precise and accurate clutter analysis and modeling of the statistical properties as will be shown in the presented results. A clear separation of the different types of rural terrain and the influence of the seasons was worked out. Additionally, model functions for the relevant parameters, characterizing the the bistatic clutter, are presented for their analytical description. The statistical properties are derived from the clutter regions of processed range-Doppler domain data, using an improved range-Doppler processing approach, for each of the four terrain types and the corresponding seasons. The data basis for the clutter analysis are the

processed range-Doppler maps from the bistatic radar measurements using a dual-channel measurement approach, with a separate reference and surveillance channel. According to the authors' current knowledge, a similar investigation based on real bistatic radar measurement data with the division into terrain subgroups and additionally for different season has not yet been carried out and published for a German rural environment. The presented data and results therefore have a significant impact on the research field of bistatic ground clutter, in which there are currently only very few results in the frequency range discussed in this thesis.

Abstract

In dieser Arbeit wird eine neuartige statistische Analyse von bistatischem Radar-Bodenclutter, für verschiedene Geländetypen ländlicher Gebiete, unter niedrigem Beleuchtungswinkel vorgestellt. Es wird eine länderspezifische Clutter-Analyse für Untergruppen ländlicher Geländetypen, anstatt für die ländliche Umgebung als Ganzes, vorgestellt. Dazu wurde das Terrain in vier dominante Untergruppen, namentlich Felder mit geringer Vegetation, Felder mit hoher Vegetation, Plantagen mit kleinen Bäumen und Waldumgebungen unterteilt, die zusammen eine typische ländliche Deutsche oder sogar mitteleuropäische Umgebung repräsentieren. In der Dissertation werden sowohl für die Sommer- als auch für die Wintervegetation die bistatischen Cluttereigenschaften dargestellt, um den saisonalen Einfluss auszuarbeiten. Dazu wurden bistatische Messkampagnen im Sommer 2019 und im Winter 2019/20 in den oben genannten vier verschiedenen ländlichen Geländetypen durchgeführt. Die Messungen wurden nach einer speziell für die Durchführung entworfenen Messmethodik ausgeführt, um vergleichbare Ergebnisse zu erhalten und um die Resultate für verschiedene Radaranwendungen nutzen zu können. Die Messungen wurden im radarrelevanten X-Band bei einer Mittenfrequenz von 8,85 GHz und über eine Bandbreite von 100 MHz entsprechend der verfügbaren Sendegenehmigung durchgeführt. Die Unterteilung des ländlichen Geländes in verschiedene Untergruppen ermöglicht eine präzisere und genauere Clutter-Analyse und Modellierung der statistischen Eigenschaften, wie in den vorgestellten Ergebnissen ersichtlich wird. Eine klare Trennung der verschiedenen ländlichen Geländetypen und des Einflusses der Jahreszeiten auf den resultierenden biststischen Clutter wurde dadurch herausgearbeitet. Zusätzlich werden Modellfunktionen

für die relevanten Parameter, welche den Clutter charakterisieren, zu dessen analytischer Beschreibung und Synthese vorgestellt. Die statistischen Eigenschaften wurden aus den Clutter-Regionen der verarbeiteten Range-Doppler-Domänendaten, unter Verwendung einer verbesserten Range-Doppler Prozessierung, für jeden der vier Geländetypen und die entsprechende Jahreszeit abgeleitet. Datengrundlage für die Clutter-Analyse sind die prozessierten Range-Doppler-Karten aus den bistatischen Radarmessungen mit einem zweikanaligen Messansatz, einem jeweils separaten Referenz- und Überwachungskanal. Eine ähnliche Untersuchung auf der Basis realer bistatischer Radarmessdaten mit der Einteilung in Gelände-Untergruppen und zusätzlich für verschiedene Jahreszeiten ist nach derzeitigem Kenntnisstand des Autors für ein deutsches ländliches Umfeld noch nicht durchgeführt und veröffentlicht worden. Die präsentierten Daten und Ergebnisse haben daher einen signifikanten Einfluss auf das Forschungsfeld des bistatischen Bodenclutters, in welchem es aktuell zudem nur sehr wenige Ergebnisse für den in dieser Arbeit behandelten Frequenzbereich gibt.

Acknowledgements

The author would like to express his gratitude to Prof. Dr. Bringmann for his supervision and support in the preparation of this work over the last few years. Especially for the support after the change from the FZI Research Center for Information Technology in Karlsruhe to the Fraunhofer Institute for High Frequency Physics and Radar Techniques FHR in Wachtberg, I would like to express my deep gratitude. Further thanks go to Prof. Dr. O'Hagan in his function as head of the department for passive radar systems at the Fraunhofer Institute for High Frequency Physics and Radar Techniques FHR who made this work at the institute possible in the first place and provided scientific support. Also many thanks go to Josef Worms, my team-leader, as scientific mentor and discussion partner for radar relevant questions. Through Prof. Dr. O'Hagan and Josef Worms I experienced an enormous learning curve in many areas of radar technology, both theoretical and practical, and had the opportunity to work in an extremely competent environment equipped with modern hardware. Thanks to all supporting colleagues at the institute and at the University of Tübingen for their input to this work. Especially Alexander Saam, Jochen Schell and David Wegner for their hardware and measurement support during the years. Last but not least, I would also like to thank my family, my girlfriend and my friends. They all accompanied me on this exciting journey and especially "endured" me during the last months.

Dedicated to my parents Paul and Erika Kohler.

Contents

List of Abbreviations

ADC Analog-to-Digital Converter

CDF Cumulative Distribution Function

CNR Clutter-to-Noise Ratio

CFAR Constant False Alarm Rate

CPI Coherent Processing Interval

DAC Digital-to-Analog Converter

DSI Direct Signal Interference

FFT Fast Fourier-Transform

GPS Global Positioning System

IQR Interquartile Range

ISAR Inverse Synthetic Aperture Radar

LNA Low Noise Amplifier

MSE Mean Square Error

PBR Passive Bistatic Radar

PCC Pearson Correlation Coefficient

PCL Passive Coherent Location

PDF Probability Density Function

SAR Synthetic Aperture Radar

SNIR Signal-to-Interference-plus-Noise Ratio

SNR Signal-to-Noise Ratio

STAP Space-Time Adaptive Processing

RCS Radar Cross Section

List of Publications within the Scope of the presented Thesis

- **Journal-Article**: Michael Kohler, Daniel W. O'Hagan, Matthias Weiss, David Wegner, Josef Worms, and Oliver Bringmann. Statistical analysis of bistatic radar ground clutter for different german rural environments. *Sensors*, 20(11):3311, Jun 2020

- **2019 IEEE Radar Conference**: M. Ummenhofer, M. Kohler, J. Schell, and D. W. O'Hagan. Direction of arrival estimation techniques for passive radar based 3d target localization. In *2019 IEEE Radar Conference (RadarConf)*, pages 1–6, 2019

- **2019 IEEE SPA**: M. Kohler, A. Saam, J. Worms, D. W. O'Hagan, J. Novacek, and O. Bringmann. Delay estimation for time synchronization of a bistatic transfer function measurement setup to single received pulses. In *2019 Signal Processing: Algorithms, Architectures, Arrangements, and Applications (SPA)*, pages 62–66, 2019

- **2019 IEEE SPS**: M. Kohler, M. Weiss, A. Saam, J. Worms, D. W. O'Hagan, and O. Bringmann. External timebase trials for phase coherency of a bistatic transfer function measurement setup. In *2019 Signal Processing Symposium (SPSympo)*, pages 319–322, 2019

- **2020 IEEE IRS**: M. Kohler, V. Duk, M. Weiss, J. Worms, J. Schell, D. O'Hagan, and O. Bringmann. Statistical analysis of bistatic rural terrain clutter. In *2020 21st International Radar Symposium (IRS)*, pages 205–210, Oct 2020

- **2020 IEEE International Radar Conference**: M. Kohler, V. Duk, M. Weiss, W. Brodowski, J. Worms, D. O'Hagan, and O. Bringmann. A multifunctional broadband receiver for bistatic x-band radar measurements. In *2020 IEEE International Radar Conference (RADAR)*, pages 918–922, 2020

The results presented in this thesis were submitted to the scientific community in the above mentioned publications.

Radar Frequency Bands

Band Designation	Nominal Frequency Range	Wavelength ($c = 3 * 10^8 \frac{m}{s}$)
HF	3 MHz - 30 MHz	100 m -10 m
VHF	30 MHz - 300 MHz	10 m - 1 m
UHF	0.3 GHz - 1 GHz	1 m - 0.3 m
L	1 GHz - 2 GHz	0.3 m - 0.15 m
S	2 GHz - 4 GHz	15 cm - 7.5 cm
C	4 GHz - 8 GHz	7.7 cm - 3.75 cm
X	8 GHz - 12 GHz	3.75 cm - 2.5 cm
K_u	12 GHz - 18 GHz	2.5 cm - 1.67 cm
K	18 GHz - 27 GHz	1.67 cm - 1.11 cm
K_a	27 GHz - 40 GHz	1.11 cm - 0.75 cm
V	40 GHz - 75 GHz	7.5 mm - 4 mm
W	75 GHz - 110 GHz	4 mm - 2.73 mm
mm	110 GHz - 300 GHz	2.73 mm - 1 mm

List of Figures

List of Tables

Chapter 1

Introduction

Radio **d**etection **a**nd **r**anging or abbreviated as **radar**, is a key technology in the field of environmental detection and perception. Starting in 1904 with the work of Christian Hülsmeyer [7], radar technology has experienced an enormous technological leap. Nevertheless a radar always consists of a transmitter and a receiver unit. In general, two basic radar architectures have become established: The monostatic radar and bistatic radar. In a bistatic radar, unlike as in the monostatic radar, transmit and receive antennas are spatially separated. In most cases, the complete, transmit and receive units are separated by several hundred or even thousands of meters. If the used transmitter is non-cooperative, i.e. cannot be controlled directly in terms of waveform or frequencies, then the radar mode is called passive bistatic radar (PBR) or passive coherent location (PCL). In a PCL system instead, illuminators of opportunity are used for the illumination of a scene, rather than a cooperative transmitter like in a bistatic radar. Such illuminators of opportunity could be broadcast or communication transmitters e.g. DVB-T/T2/S2, GSM, LTE or FM [8, 9],[10]-[11],[12],[13]-[14],[15, 16, 17]. Bistatic and passive bistatic radar and its applications are currently the subjects of high research interest [18]-[19]. For combined applications of two transmitters and a directional information, please refer to [2].

Depending on where the transmitter and receiver units are located, whether on the ground, air, or even in space, whether they are stationary or moving, different

bistatic or passive bistatic radar modes can be distinguished. On the one hand, there are ground-based bistatic radar applications where the transmitter and receiver are located on the earth's surface including sea surfaces [20]. Airborne applications where either the transmitter, the receiver, or both are in the air, e.g. mounted on an aircraft [21]. A further arrangement of the bistatic radar units can be found in the space sector. Here the transmitter, receiver, or also even both are in space e.g. mounted on satellites [22]. Airborne and spaceborne bistatic radar are mainly used for imaging radar applications in the field of Synthetic Aperture Radar (SAR) or Inverse Synthetic Aperture Radar (ISAR). There are also imaging applications in the field of spaceborne-airborne bistatic radar [23], where e.g. the transmitter is located on a satellite and the receiver located on a moving aircraft. By using several transmitters or receivers, the bistatic arrangement becomes a multi-static radar arrangement. Provided that technical barriers are overcome, radar geometries can be extended as desired, e.g. by adding transmitter and receiver units on different frequency bands, thus creating a multi-static multi-frequency arrangement [24]. However, with the complexity of the geometry, the corresponding hardware and processing effort increases enormously and is offset by a potential benefit.

In general, the hardware architecture and processing in a bistatic radar is more complex than in a monostatic radar. This starts with the problem of the separated transmit and receive units and the access to transmit and receive signals, necessary for radar processing and ends with the more complex radar geometry resulting from this separation. Especially the synchronization of the transmitting and receiving units is a technical challenge [4, 25]. In addition to the more complex hardware and processing requirements due to the bistatic geometry, all bistatic radar applications inherently suffer from two dominant phenomena caused by its separated structure: First, the direct signal component on the receiver side. In addition to the desired object echos, the bistatic receiver also receives the signal emitted by the transmitter on direct propagation path. This direct signal component is usually decades higher in amplitude compared to an echo reflected by an illuminated object, because of the reduced attenuation by direct transmission. The resulting dynamic range may, there-

fore, be too large for the used hardware to detect weaker object reflections. Without appropriate direct signal suppression and cancellation either in hardware, software or both the detection performance can decrease due to echo masking. The second unwanted competitive signal components received by the bistatic radar receiver are the unwanted signal reflections caused by scatterers within the illuminated scene. For convention, in this thesis, points of reflected replicas of the transmitted signal are called scatterers. In the terminology of bistatic radar, these unwanted signal reflections and receptions are commonly known as bistatic clutter. For the sake of completeness, it should be mentioned that also monostatic radar geometries can suffers from the problem of a strong transmit signal component which can cross-couple to the receiver. However, this influence can be eliminated here for example by alternating transmission and reception operation. The simultaneous transmission and reception (STAR) is a separated current research topic [26]. The problem of arising clutter is also given with a monostatic radar setup. However, this influence can be reduced more easily due to the simpler geometry with the co-located transmit and receive units.

Depending on the strength and the behavior of the bistatic clutter, its appearance can drastically decrease the radar detection performance. Similar to the direct signal component, strong clutter can also severely restrict the dynamic range and thus make weak object reflections invisible. Initially, all unwanted signal reflections can be described as clutter. The clutter sources can be of different nature. Clutter can be caused by terrain objects, vegetation such as trees, buildings, other objects in the scene, precipitation such as rain or snow, water surfaces such as lakes or the sea. Especially clutter resulting from object movements, such as vegetation moving in the wind or moving sea surfaces, makes object detection more difficult due to its non-stationary behavior. In order to suppress the influence of the resulting clutter and so increase the radar performance in terms of detection performance, in every bistatic radar an appropriate clutter suppression is needed [27, 28, 29, 30, 31]. In order to carry out clutter suppression, a-priori knowledge of the corresponding clutter properties is necessary.

The work in this thesis describes the rural terrain clutter and its influence on ground-based bistatic radar applications where the transmitter and receiver units are stationary. The frequency range of interest here is the X-Band, the frequencies between 8 GHz and 12 GHz. There are numerous applications for ground-based bistatic radar, especially for this frequency range. For example, weather radars benefit from the bistatic geometry and back-scatter in the detection of rain and thunderstorm cells or the determination of wind vectors [32]. Ground-based bistatic radar applications for monitoring airspaces at airports as a replacement for classical secondary radar are another example. The monitoring of airspaces for collision avoidance is in general an increasingly relevant area of application. The *Parasol* system developed by Fraunhofer FHR for the demand-based anti-collision lighting of wind parks to avoid collisions with small aircraft is worth mentioning here [33]. In addition to the detection of aircraft, the detection of birds also plays an important role in collision avoidance [34]. Of great importance are also ground-based bistatic SAR (GB-SAR) or inverse SAR (GB-ISAR) applications in the field of environmental monitoring. This can include the structural monitoring of technical installations [35], i.e. also the monitoring of mines or mountain slopes to detect landslides [34]. GB-SAR/ISAR is also an important remote sensing instrument to detect displacements of buildings, bridges, or general constructions [17]. Further bistatic applications can be found in the field of environmental sensing e.g. crop sensing [36]. The determination of soil moisture using bistatic radar, is important for irrigation planning and the prediction of flash floods.[37]. Recently, there has been great interest in the detection of commercially available quadrocopters, which are increasingly entering secured areas such as airport facilities and endangering flight operations. X-band bistatic radar solutions to this novel problem are available in [38].

These and other radar applications are particularly influenced by ground clutter. The applications mentioned are mostly located in or surrounded by rural environments. These can be fields, trees or other vegetation which, due to wind movement, lead to non-stationary clutter behaviour and significantly reduce the detection

performance of the radar. The strong back-scattering in the X-band wavelength range by such structures then leads to distinctly pronounced clutter behaviour. In this thesis the focus is on country-specific bistatic rural ground clutter analysis caused by rural environments. The analysis therefore is valid for both bistatic and passive radar applications. Among others, the performance of a ground based bistatic radar in the context of object detection is particularly dependent on the characteristics and statistical parameters of this clutter. In general, rural ground clutter can be fluctuating or non-fluctuating. Accordingly, clutter can occur both in bistatic range and in Doppler dimension, decreasing object detection and object tracking performance. Due to movements of the illuminated scene e.g. movements of trees due to the wind, the clutter spreads also in the Doppler dimension. Depending on the clutter strength, a moving object echo can be masked, leading to a decrease in detection performance. Also, the clutter sidelobes in the bistatic range and Doppler domain can cause an object echo masking. In addition to the above and other reasons caused by clutter, a suppression is necessary.

The chapter **Motivation and Impact Statement** explains the significant contribution of this work to bistatic clutter analysis in X-band. Existing literature to underline the necessity of the results obtained here can be found in the chapter **Related Literature Review**. In the chapter **Necessary Bistatic Radar Fundamentals** the essential basics of the bistatic radar geometry are presented. These are necessary for understanding the work presented here. Also to understand how the measurement approach presented, differs in hardware as well as processing from others and why it is much more efficient. A selection of statistical parameters to describe the clutter obtained from the measured data is presented in the chapter **Descriptive Bistatic Rural Clutter Statistics**. The developed measurement methodology for the acquisition of measurement data, the used bistatic measurement setup for it and a specially adapted signal processing, as well as its advantages, are presented in the chapter **Measurement Methodology and Materials**. This chapter also presents the relevant parameters of the measurement campaigns, carried out in 2019 and 2020. The clutter properties obtained from the processed measurement data are presented

in the chapter **Rural Bistatic Clutter Analysis** together with the derived model functions to analytically describe the clutter and elaborated and evaluated in detail in the chapter **Discussion**. At the end of this thesis, the chapter **General Conclusions and Outlook on Future Work** gives an overview of future work. Some of the findings of this thesis are used in other projects at Fraunhofer FHR.

Chapter 2

Motivation and Impact Statement

As discussed in the previous chapter, the stationary and non-stationary clutter caused by rural environments leads to a reduction in the detection performance of a bistatic radar and clutter suppression is needed. This involves a-priori knowledge about the clutter characteristics. The a-priori knowledge of the clutter characteristics can also be exploited to adaptive illumination and waveform design. The adaptation and optimization of the radar waveform to an object in a given environment with respect to a certain criterion such as signal-to-interference-plus-noise ratio (SNIR) requires also knowledge of the clutter statistics [39]-[40] in order to optimize the waveform parameters. The results obtained from clutter analysis are also of great interest for applications in the field of adaptive detection, such as knowledge-aided space-time adaptive processing (STAP), since the clutter signal space can be modeled accordingly, rather than assuming homogeneous environments [41]. This also includes general detectors based on hypothesis testing, for example, since the disturbance in the form of the environmental clutter can be better modeled by derived statistical models which can be used to increase detection performance [42].

The technical measurement of clutter characteristics is very time-consuming and involves many individual measurements. This thesis presents a novel, low-grazing angle, interpreted as the angle between the scene and the illumination, statistical clutter analysis for German rural environments. Due to the geograph-

ical location of Germany, this analysis can also be considered representative for a Central European rural vegetation. The statistical parameters have been derived from real bistatic measurement data. Therefore, time-consuming individual ground-based bistatic radar measurements have been carried out in 2019 and 2020. The measurements have been performed at the radar relevant X-band frequency range over a bandwidth of 100 MHz and so this thesis presents statistical clutter models and analysis according to this frequency range. To investigate the seasonal influence on the rural clutter, the measurements were carried out both in summer and winter. A ground-based bistatic measurement setup, using a dual-channel approach has therefore been used to carry out the measurements. A dual-channel receiver was used as bistatic radar receiver for the measurements. The direct signal of the transmitter is delivered via the first receiving channel and the clutter echoes of the corresponding terrain under test are received with the second receiver channel. A cooperative X-band transmitter was used to illuminate the terrain during each measurement. The two-channel approach is much easier to realize than a bistaic design that requires a direct connection between receiver and transmitter. Instead, the transmitter signal is received over the air via the reference antenna. However, this approach requires additional processing steps to match the received radar pulses to the pulses of the surveillance channel. The presented measurement setup using two separated receive channels for the surveillance and reference channel together with the proposed coherent signal processing approach enables accurate and low-cost bistatic measurements, compared to setups where a physical connection between transmitter and receiver is needed. Therefore, in the context of this thesis an improved signal processing approach was developed which is also presented. The sampled data has then processed and clutter analysis was performed on the resulting range-Doppler map data.

A country-specific clutter analysis for subgroups of rural environments rather than for the rural environment as a whole will be presented. The idea of the subdivision of the rural environment has already been published in the author's papers

in [1, 5, 6]. According to the rural environments prevailing in Germany and Central Europe, the measurements took place in four dominant rural terrain subgroups. These four rural terrain subgroups, chosen by the author are listed below:

- Fields with low vegetation
- Fields with high vegetation
- Plantations with small trees
- Forest environments

Fields with low vegetation stand for areas which mainly consist of meadows, farmland or other agricultural areas with low vegetation. Fields with high vegetation are correspondingly the group of agricultural areas with high vegetation such as corn, wheat or grain fields. The third type of terrain is made up of plantations of small trees such as fruit tree plantations, vineyards or other arrangements of smaller trees. Forests form the fourth subgroup. Together, these four groups largely represent a typical German rural environment. A sample picture for each of the listed terrain types in shown in Figure 2.1.

A detailed justification for the selection of these types of terrain is given in the chapter **Measurement Methodology and Materials**.

According to the knowledge of the author, such measurement campaigns to collect data of low-grazing angle German rural terrain bistatic clutter is the first of its kind at the time of writing this thesis. The data obtained in this thesis for the characterization of the country-specific bistatic clutter thus form a significant basis for further analysis in the field of bistatic ground clutter research, modeling and clutter suppression. Together with the chosen subdivision into four dominant rural terrain groups, this work makes an important contribution to bistatic clutter analysis close to measurement data which are otherwise only available in very small quantities for bistatic ground clutter in the X-band frequency range. The technical and signal processing adaptations that were developed to be able to perform bistatic measurements with the used two-channel approach are also applied beyond the scope of this

(a) Fields with low vegetation

(b) Fields with high vegetation

(c) Plantations of small trees

(d) Forest environments

Figure 2.1: The four subgroups of rural terrain that mainly represent a typical German rural environment.

thesis. Due to the chosen low grazing and scattering angles during all measurements, which is the prevailing condition for ground-based approaches, also enables the use of the presented results for a wide variety of bistatic radar applications suffering especially from rural ground clutter. Therefore, the results obtained can also be used e.g. for SAR/ISAR applications in the area of airborne SAR affected by rural ground clutter under low grazing angles.

2.1 The main research questions and contributions of the thesis

Bistatic radar applications are inherently affected by the problem of clutter. In general, there are very few evaluations of measurement data on bistatic clutter and its characteristic features available in the current literature. There is an enormous

need for research to generate statistical parameters and models of the clutter from real measurement data, which are needed for clutter suppression, clutter reduction, adaptive radar modes and simulation purposes. Especially the clutter caused by rural environments has not been sufficiently researched so far and there is a lack of appropriate analyses of the occurring clutter in rural environments. Such rural environments cause a considerable amount of non-stationary clutter due to the vegetation they contain besides the stationary clutter caused by stationary objects like tree trunks and especially by moving elements like branches and leaves moved by wind. These results in clutter components with a Doppler component and the clutter forms spread in the range and Doppler domain. These non-deterministic clutter phenomena are described statistically in this thesis and therefore have a significant impact on the research field of bistatic radar and its applications. In addition to the pure data analysis, the focus of this thesis is the metrological data acquisition of clutter. The present work therefore makes a contribution to the following research questions:

- **In which dominant types of terrain can the prevailing rural environment be classified and the clutter occurring in it be metrologically investigated?**

  The clutter caused by rural environments is of great interest for bistatic radar applications in the 8 GHz to 12 GHz range due to its wavelength. The structural sizes of the different vegetation lead to distinct clutter characteristics. By movement of the vegetation the clutter gets an additional Doppler component. In this thesis four dominant terrain types are identified and investigated that cause a dominant bistatic clutter. The presented classification is a novelty in the field of bistatic clutter analysis. For this thesis a unique series of measurements was carried out over a period of two years to collect measurement data within the different types of rural terrain.

- **How can the rural bistatic clutter be efficiently measured and how is an appropriate measurement and data processing methodology structured?**

  For the measurement of the bistatic clutter a setup consisting of a spatially

separated transmitter and receiver unit was used and is presented in this thesis. A dual-channel approach is proposed, in which the reference signal necessary for the Range-Doppler based processing is received via a reference channel. Transmitter and receiver unit are synchronized for a coherent SNR-maximized processing via external GPS-disciplined oscillators. This allows a flexible measurement process in different terrain conditions. For the processing of the data, an improved processing based on the generalized cross-correlation was developed. This enables the reference signal detection required for range-Doppler processing even under low SNR conditions.Together with a waveform analysis, an optimized processing adapted to the problem and the hardware is presented.

- **What influence does the occurring rural clutter have on the detection performance of a bistatic radar?**
  Due to the different vegetation, the different clutter leads to an influence on the detection performance of a bistatic radar. A novel analysis is presented for the four rural terrain types to evaluate the characteristics of the clutter and its influence on the detection performance of moving objects.

- **What are the statistical characteristics of the clutter in the different types of terrain?**
  Clutter suppression or reduction and other adaptive processing applications require a-priori knowledge of the statistical clutter properties. This thesis presents for the first time a statistical analysis of the rural bistatic clutter properties in range and Doppler for the four dominant terrain types identified representing a typical German or Central European environment.

- **What influence do the seasons have on the statistical parameters?** The vegetation within the investigated terrain types is significantly influenced by the seasons. This influence is evaluated by means of statistical parameters for summer and winter measurement data. Therefore, a considerable number of measurement campaigns were carried out in the years 2019 and 2020 during

the summer and winter season.

- **Which model functions describe the occurring clutter in the different seasons?**

  Statistical model functions were derived from the measured data to describe the rural bistatic clutter in different types of terrain and at different seasons. The presented results provides a significant basis for the simulation of corresponding rural bistatic clutter.

- **What are the statistical relationships between the Clutter in different types of terrain and also between the seasons?**

  By means of correlation analysis, the relationships of clutter statistics and model functions between the different types of terrain and seasons were evaluated The presented results are a significant contribution to work in the field of classification and cognitive bistatic radar applications.

The new type of measurement and separate statistical analysis of the bistatic clutter in the four identified dominant rural terrain types are the novelty of the work presented here. Due to the very small number of published analyses in the field of bistatic radar, the above mentioned research questions and the results presented in this paper are an important basis for the research field of the bistatic cluster.

Chapter 3

Related Literature Review

The emphasis of this thesis is the investigation of bistatic ground clutter for the X-band of German rural environments under low grazing angles and the bistatic angle range from 60° to 80°. It should be mentioned that in clutter analysis the grazing angle is defined as the elevation angle between the antenna boresight and the clutter surface [43]. The back-scattering properties of the clutter source depend, among other things, on this angle. For ground-based bistatic applications, as treated in this thesis, small grazing angles are of interest. There are generally very few publications on bistatic ground clutter for the frequency range 8 GHz to 12 GHz.

There are several reasons for the absence of many bistatic measurements, in the frequency range from 8 GHz to 12 GHz from rural ground clutter for ground-based bistatic radar. Firstly, the purchase price of analog hardware components in this frequency range is significantly more expensive compared to lower frequency ranges. The single components like general amplifiers, low-noise amplifiers, power-amplifiers, filters or mixer-stages are connected with clearly increased costs. The same applies to antenna elements with corresponding antenna gain. The construction of a bistatic radar setup is also reflected in higher hardware costs. Dedicated transmitter and receiver units are required, which must be able to be set up separately over long distances. Measurements over a bandwidth of 100 MHz, as presented in this thesis, also require analog-to-digital converters (ADC) with a correspondingly high sampling rate. Sampling in higher Nyquist bands has even more

requirements on the ADC and analog frontend characteristics. The bistatic geometry also makes radar processing more difficult, since different bistatic angles have to be considered. A granular subdivision of a rural area, as carried out in this thesis, into four dominant subgroups is associated with a considerable measurement effort, which in this concrete example extended over the years 2019 and 2020. Since the commercial benefit for bistatic radar systems is not yet as advanced as for cheaper monostatic setups, this is an additional obstacle which, however, is being overcome more and more with decreasing costs. The Fraunhofer FHR made the presented bistatic clutter investigations possible due to its excellent equipment, by providing the transmitter and receiver units which were adapted in the context of this thesis and the commitment driven by its own interest in the corresponding measurement data, where many research is carried out for radar applications in this frequency range.

There are already numerous publications about monostatic rural ground clutter for the X-band frequency range. Since there are only very few publications on bistatic ground clutter for the frequency range from 8 GHz to 12 GHz, it is worth mentioning the corresponding work from the field of monostatic radar. Fundamental research on the influence of several composite North-American rural terrain types including, among others, farmland, forests, lakes or mountains under low grazing angles has been addressed in several publications by J. B. Billingsley [44, 45, 46]. The author presents clutter models including the histograms, momentum analysis and goodness-of-fit testing for various terrain types e.g., scrub desert, rangeland, cropland vegetation and forests according to the country-specific vegetation where the measurements have been carried out. Further statistical clutter analysis for windblown foliage also considering forest environments using spectral measurements has been presented in [47, 48, 49, 50]. The authors present amplitude models describing the clutter distribution for different types of terrain, terrain-dependent damping factors and analytical descriptions of Doppler models for different wind speeds. Gaussian, power-law and double-exponential spectral models are used to describe the clutter spread in the Doppler dimension for the windblown terrains.

The influence of the seasons on the clutter properties has also been investigated. For this purpose, measurements were carried out for different types of terrain in different seasons. Further statistical clutter parameters and probability density functions on the clutter influence for different specific forest components e.g., canopies or leaves and branches of the trees are presented in [51]. It was shown that the amplitude distribution of the clutter values for leaves smaller than the incident wavelength can be described by a Rayleigh distribution. For leaves in the order of magnitude of the incident wavelength, the amplitudes are distributed according to a Gamma distribution. The authors also describe the geometric simulation of the different plant characteristics. For further composite terrains also including farmland and other country-specific rural terrain types several statistical clutter parameters based on amplitude statistics are presented in [52]. The authors present a derived Poisson distribution to model the amplitude distribution with empirically adapted parameters to describe composite rural environments for high as well as low grazing angles. A key parameter is the clutter type, where the authors distinguish between weak, medium and strong back-scatterers. Statistical clutter models for spatial amplitude statistics of rural ground-based clutter are presented in [53]. Terrain-specific parameters of a Weibull distribution describing the clutter amplitudes for low grazing angles are presented, whereby a distinction is made between the terrain types general rural, open farmland, continuous forest and meadows. The distributions show a clear separation of meadows from the other types of terrain. Spectral component analysis of ground clutter for agricultural land, farmland and forest environments are described in [54]. One of the main statements of the work is the composition of the Doppler models. A distinction is made between a coherent and a diffuse component. According to the authors, the coherent component is mainly formed by unbalanced objects such as tree trunks, whereas the moving objects form the diffuse component. Grass- and soil-based clutter has been investigated in [55]. The authors describe the amplitude distributions with a Weibull distribution. In addition, the shift of the distribution with increasing grazing angle towards lower attenuation values was worked out. The influence of an illumination with a low grazing angle

range for Indian rural terrain on the statistical clutter properties is presented in [56]. A comprehensive database considering different clutter density functions can be found in [57] also for snow covered terrain. Another example for country-specific analysis are Doppler spectrum-based clutter models for South African urban terrain which can be found in [58]. Amplitude-based clutter models specific for different Saudi Arabian rural terrain are presented in [59] for low grazing angles. Clutter statistics for cultivated land, wooded hills and forest also for different seasons are presented in [60]. Further land clutter models and the corresponding probability density functions for bistatic applications are presented in [61]. The analysis of clutter caused by palm trees considering their unique structure has been addressed in [62].

The first bistatic clutter measurements were performed in 1965 by the antenna laboratory of Ohio State University [63]. Bistatic clutter was measured from terrain consisting mainly of sand, loam or soybeans. Fields with low vegetation consisting of grass and bean plantations were also measured. The measurements were performed for small, medium and large grazing angles. A bistatic angle range from 0° to 180° was thereby covered. The main focus of the measurements has been to investigate the back-scattering of the different types of terrain. A change of the back-scattering properties with increased terrain roughness could be shown. This was shown at a maximum bistatic angle of 180°. In the following years, A. R. Domville conducted several measurement campaigns in rural terrain [64]-[65]. This terrain consisted mainly of grasslands and trees. Bistatic ground measurements were also performed with an airborne receiver, with a stationary transmitter on the ground. The prevailing grazing and scattering angles during the measurements were also comparable to those of a completely ground-based setup. However, the measurements were carried out at only a few points. This kind of measurements underlines once more how the acquired data can also be used in other radar geometries (e.g. SAR/ISAR). In the late seventies, the University of Michigan carried out further bistatic clutter measurements in grasslands with cement taxiways [66]. Further experiments were carried out in terrain mainly consisting of weed and scrub

trees. The back scattering coefficients were determined over the measured bistatic angular range. Interesting measurement data but outside the X-band is available in [67]. The influence of trees and tree foliage on the bistatic clutter was investigated for the first time. Furthermore, sand and gravel covered terrain was also measured. In [68] clutter models in the frequency range from 9.75 GHz to 10.25 GHz are presented for a patch of land, consisting of long grass and twig-like branches. The measurements were focused on the influence of the bistatic angle, variying it from 2° to 30°. Among other things, Weibull distributions could be fitted to the measured data with lower bistatic angles. All in all, the work on rural bistatic clutter is very manageable. Therefore the present thesis makes a significant contribution to this area of bistatic clutter analysis.

In the following Table 3.1, the bistatic rural ground clutter measurements of the corresponding terrain and grazing, scattering and bistatic angles in this thesis are again compared to the above mentioned work. Only those works were included in the table which are considered significant by the author. The work of [67] was also entered in the table although it is outside the frequency range under consideration. However, these are the only published data concerning bistatic measurements in forest environments.

3.1 Critical Discussion

In the area of bistatic clutter, there is generally still a large gap in real measurement data compared to monostatic measurement campaigns. Here, the author explicitly refers again to the numerous experiments of J. B. Billingsley carried out over the years. However, especially this work indicates how complex and extensive such measurements and analyses are. The clutter properties depend on numerous influencing factors, which of course cannot be covered to a certain extent within the scope of a single dissertation. However, the results presented here provide a contribution in the area of bistatic clutter analysis for four elementary rural environment types. In this thesis, the results refer only to the bistatic angle range from 60° to 80° for grazing angles smaller than 5°. However, without wanting to anticipate results, it is already evident here that correlations to measurement campaigns of other scientists are available regarding Weibull distributions fitted to the clutter amplitudes. The analysis of the monostatic measurements of Billingsley also showed a Weibull distribution of the clutter amplitudes for terrain types consisting of flat farmland, meadows and for terrain types consisting of forests. G. Zhu was also able to derive Weibull distributions from his measured data for grasslands in his analyses, which compares to the terrain type of fields with low vegetation determined here. A. Mohan was also able to derive Weibull distributions from bistatic measurement data in the X-band for grassy areas. However, this referred to the bistatic angular range from 25° to 30°. In contrast to the work presented here, however, the data was not averaged over the corresponding range-Doppler bins, which is the case in this thesis due to limited recording capacity of the hardware. Interestingly, monostatic measurements by J. B. Billingsley showed a Rayleigh distribution of clutter amplitudes for trees moving in the wind of forest environments. Such investigations were not carried out in the context of this thesis, however, the influence of the seasons, summer and winter on the clutter characteristics was.

Table 3.1: Comparison of different relevant publications

Date	Organization	Author	Rural Terrain Types	Freq.	Pol.	Methodology	Scattering and Bistatic Angles
2020	Fraunhofer FHR	M. Kohler	country-specific for Germany/Central Europe: fields with low vegetation fields with high vegetation plantations of small trees forest environments summer and winter influence	8.8 GHz - 8.9 GHz	VV	Coherent dual-channel approach	$\phi_{GZ} \leq 5^\circ$ $\phi_{SZ} \leq 5^\circ$ $\beta = 60^\circ - 80^\circ$ (avg.)
2015	Ohio State University	A. Mohan	patch of land, consisting of long grass and twig-like branches	9.75 GHz - 10.25 GHz	VV	Coherent single-channel approach	$\phi_{GZ} = 10^\circ$ $\phi_{SZ} = 10^\circ$ $\beta = 2^\circ - 30^\circ$ in steps of 2°
1988	University of Michigan	Ulaby Et al.	desert terrain, gravel covered terrain, trees and tree foliage (mixed)	34 GHz - 35 GHz	VV & HH	Coherent single-channel approach	$\phi_{GZ} = 30^\circ$ $\phi_{SZ} = 10^\circ - 90^\circ$ $\beta = 0^\circ - 170^\circ$
1977	University of Michigan	Larson Et al.	grass covered terrain, terrain with taxiways, weed and scrub tree terrain	9.4 GHz	VV & HV	Coherent single-channel approach	$\phi_{GZ} =$ $10^\circ, 15^\circ, 20^\circ, 40^\circ$ $\phi_{SZ} = 5^\circ, 10^\circ, 20^\circ$ $\beta = 0^\circ - 180^\circ$

Chapter 4

Necessary Bistatic Radar Fundamentals

The bistatic radar geometry is more complex compared to a monostatic radar, where the transmitter and receiver are co-located. Therefore, this chapter gives the reader the necessary theoretical background about bistatic radar and bistatic radar clutter, to understand the work presented in this thesis. Starting with the fundamentals of the monostatic and bistatic radar geometry, through the bistatic range equation to bistatic range and Doppler, the necessary relationships are shown. Because the clutter analyses are performed on the data of the processed range-Doppler domain data, a detailed explanation about the latter is presented. Afterwards the bistatic clutter geometry is explained. The measurement approach used in this thesis and its advantages together with the processing developed for it, become more understandable through the theoretical foundations in this chapter and thus better show its significance.

4.1 Radar Geometries and its Parameters

This section provides the reader with an overview about fundamental radar geometries. Two basic radar geometries are presented, namely monostatic and bistatic.

The main difference between both geometries is the co-location between transmitter and receiver in a monostatic radar geometry, while they are dislocated in a bistatic radar. Depending on the bistatic radar application described in this thesis, only the transmit and receive antennas are physically separated but connected via a common analog front-end, digital-to-analog and analog-to-digital converter, as well as a common timebase reference and local oscillator. This simple case differs from the much more complex approach where the transmit and receive units are completely separated. Our complex approach is also used in this thesis as this was the reasonable way to perform the clutter measurements in different types of terrain with different dimensions. The spatial separation between transmitter and receiver allows a flexible setup according to the terrain conditions. With a dual-channel receiver a coherent radar processing is possible without a direct physical connection between transmitter and receiver.

4.1.1 The Monostatic Radar Geometry

In Figure 4.1 a monostatic radar geometry is shown. In a monostatic pulsed radar, the transmitter and receiver are co-located. During signal transmission the receiver is switched off because otherwise the much weaker object echo would be covered by the transmitted signal, coupling to the receive path. Instead, the receiver is switched on after the signal is transmitted. This is leading to a minimum distance in which such a radar can be operated called *blind range* because during the time the pulse is transmitted the receiver is turned off and no echos can be received with this range. After signal transmission, the signal reflected is received with a time delay corresponding to the range between the radar and the object. The illuminated object with a distance R to the receiver is leading to a time shifted signal reflection corresponding to the following delay:

$$\tau = \frac{2R}{c} \tag{4.1}$$

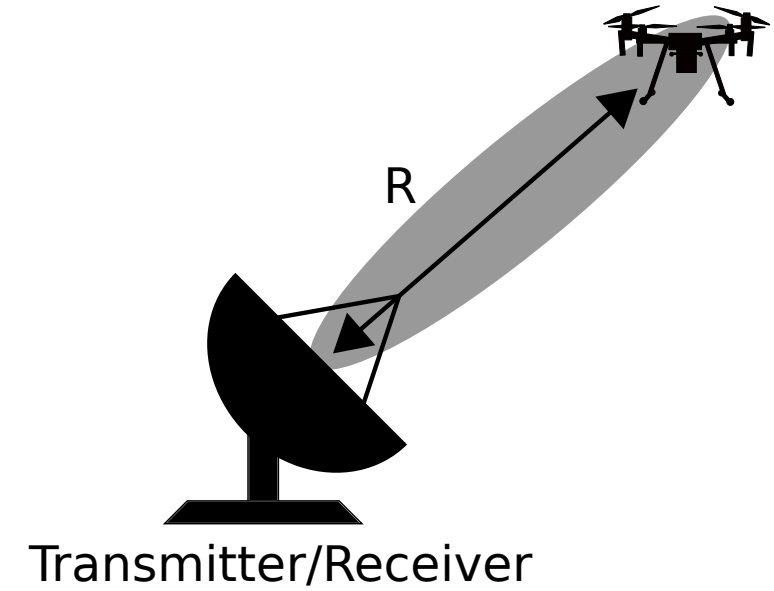

Figure 4.1: Geometry of a monostatic radar with co-located transmitter and receiver.

where c is the speed of light (approximately $3 * 10^8 \frac{m}{s}$). The factor of two in the equation above describes the overall round trip time of the transmitted signal. In a monostatic radar, the measured delay or equivalent range corresponds to the actual distance of the object from the receiver. Without additional direction of arrival information of the impinging signal, the object could be located somewhere on a circle with radius R around the antenna phase center. For additional angular information e.g. a steerable antenna with a pencil beam is needed to resolve the angular information.

4.1.2 The Bistatic Radar Geometry

In recent years there has been increasing research in the field of radar based on the concept of bistatic radar. The bistatic radar setup consists of at one transmitter and one dislocated receiver. Beside the bistatic radar geometry there are also multistatic radar geometries where one or multiple transmitters illuminate the area to be monitored and the scattered signals are received by one or multiple receivers. Nevertheless, in the bistatic radar, in contrast to the monostatic radar, the transmitter and receiver are spatial separated by a distance L which is commonly called the baseline. As already mentioned, sometimes only the antennas are spatially separated. The transmitter and receiver units then continue to share the same internal clock

and oscillators. Instead in this thesis a radar setup with the spatial separation of the transmit and receive units is considered. In Figure 4.2 a bistatic radar geometry is shown [69]. The transmitter covers the monitored area with its transmit antenna beam and the receiver collects the direct signal from the transmitter as well as the scattered signals by surrounding object with its receive antenna beam. According to Figure 4.2 an object inside the monitored area with a distance R_T to the transmitter is illuminated. The distance between the object and receiver is thereby R_R. The object reflection within the receive antenna beam impinges under the receive angle α_R. The angle under which the object is seen between the transmitter and receiver is called bistatic angle β. As well as any other radar, the bistatic setup measures a delay between transmitted and received signal corresponding to a certain distance. In contrast to a monostatic radar this delay is the detour over the distances from the transmitter to the object and to the receiver $R_T + R_R$, building up an ellipsoid rather than a circle compared to the monostatic radar. To calculate the true distance between the receiver and the object also the receive angle has the be known. This parameter can be determined by different techniques e.g time difference of arrival using a dual-channel receiver or an antenna arrangement with a steerable antenna beam. Together with the bistatic range and the knowledge of the object receive angle, as well as the distance between the transmitter and receiver, the true object distance can be calculated as follows:

$$R_R = \frac{(R_T + R_R)^2 - L^2}{2(R_T + R_R) + Lsin(\alpha_R)} \tag{4.2}$$

In a bistatic radar setup the transmitter and receiver form a contour of constant bistatic range defined by $R_T + R_R = const$ for a specific object distance. As aforementioned, the projected contour is an ellipse (see Figure 4.3), with the transmitter and receiver as the two focal points. Objects on any point of this contour result in the same bistatic range in the range-Doppler map. Objects on the baseline between transmitter an receiver result in zero bistatic range. This case is commonly know as forward scatter [70].

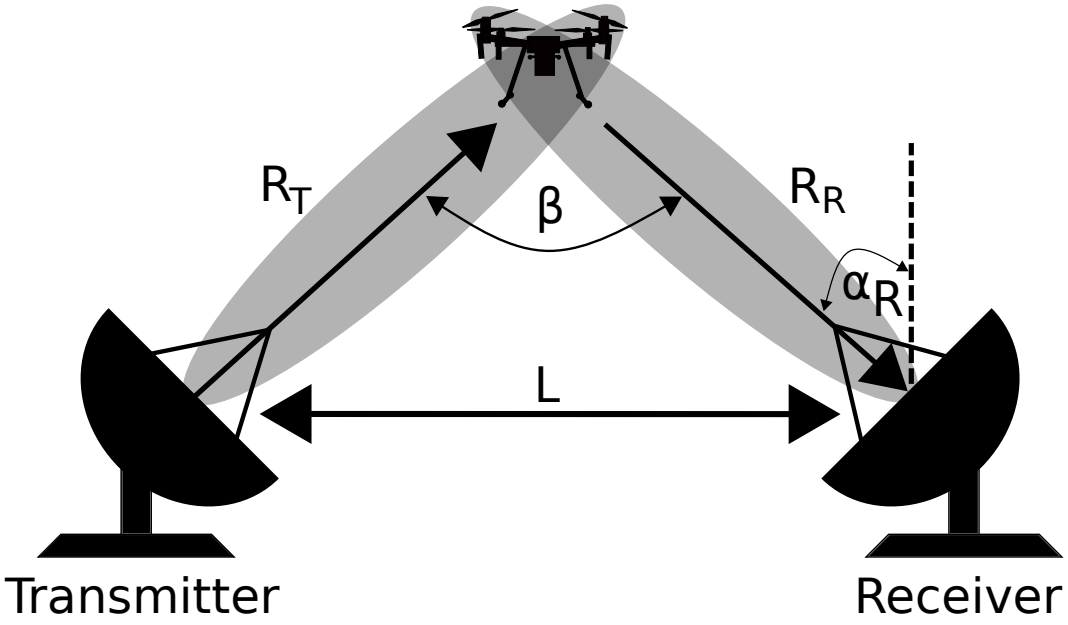

Figure 4.2: Geometry of a bistatic radar with separated transmitter and receiver.

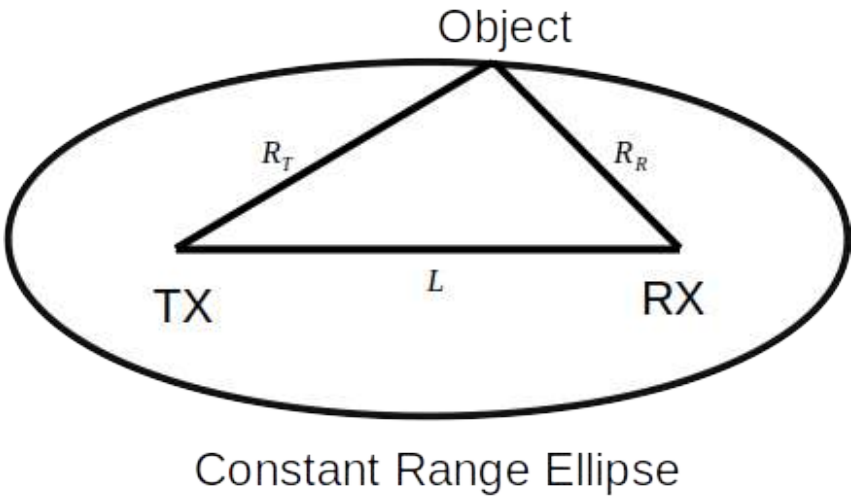

Figure 4.3: Contour of constant range.

In this thesis an approach with a dual-channel receiver is used. The two received channels are called the reference channel and the surveillance channel. The reference channel antenna is thereby steered towards the transmitter. The surveillance channel antenna is steered towards the scene under test. This approach is related to passive bistatic radar setups where the transmitted signal can be unknown. The reference channel receives thereby a copy of the transmitted signal on a direct propagation path, while the object reflection is received by the surveillance channel. In contrast to this proposed hardware setup also direct sampling of the transmitted signal sampling on the transmitter side is possible thus resulting in much higher hardware costs because of the sample based signal synchronization needed between the transmitter and receiver. A simple solution could be a physical connection between the transmitter and receiver. However, it is not possible to transmit a high-frequency signal over a longer distance without additional losses. Also the transmission of individual pulse parameters is connected with additional processing in the transmitter unit. Therefore, in the opinion of the author, this approach is unsuitable for bistatic clutter measurements, since the terrain dimensions require larger distances between the transmitter and receiver unit.

4.1.3 The Radar Range Equation

The radar performance with respect to the maximum range can be specified by the radar range equation. The radar range is mainly given by the system parameters such as transmission power and radar cross-section (RCS) as the back-scattered energy of the illuminated object.

4.1.3.1 The Monostatic Range Equation

The maximum distance of a monostatic radar can be calculated using the radar range equation. For the monostatic radar the range equation for a certain wavelength λ is defined as follows:

$$R_{max} = \sqrt[4]{\frac{P_T G^2 \lambda^2 \sigma}{P_R min (4\pi)^3 L_{tot}}} \tag{4.3}$$

where $P_R min$ defines the minimum required received power considering all

system losses L_{tot} and the illuminated radar cross-section σ of the object. P_T defines the transmit power, not including the antenna gain. Because the transmit and receive antenna are used for both, transmission and reception, the antenna gains G can be assumed to be equal. Otherwise different antenna gains have to be considered.

4.1.3.2 The Bistatic Range Equation

Because of the separation between transmitter and receiver, the distances from the transmitter to the illuminated object and from the object to the receiver are different. This difference compared to the monostatic geometry is leading to the bistatic range equation, defined for a certain wavelength λ as follows [69]:

$$(R_T R_R)_{max} = \sqrt{\frac{(P_T G_T G_R \lambda^2 \sigma)}{P_{Rmin}(4\pi)^3 L_{tot}}} \tag{4.4}$$

where R_T and R_R are the distance between the transmitter and the illuminated object and between the receiver and the illuminated object respectively. The object is assumed with the RCS value σ. P_T is the transmit signal power, not including the transmit antenna gain. The transmit antenna gain is labeled with G_T and the receive antenna gain with G_R. Compared to the monostatic range equation, two different antenna gains are considered, which is also the case for the hardware setup developed by Fraunhofer FHR and used within the scope of this thesis. Often a transmit antenna with a wide field of view, but therefore with lower gain is used to illuminate a broad area. The receive antenna often is chosen with a more narrow field of view but there with higher antenna gain. For the developed measurement setup two different antenna types were used, namely Vivaldi antenna elements for the reception and a Horn antenna element for the signal transmission. This made it possible to achieve a similarly high gain on the transmit and receive side and at the same time a larger field of view on the transmit side.

4.1.4 The Bistatic Range Resolution

The range resolution, however, describes the ability of a radar how two range cells can be resolved. In a monostatic radar, the range resolution ΔR_{mono} is inversely proportional to the bandwidth of the radiated waveform:

$$\Delta R_{mono} = \frac{c}{2bw} \tag{4.5}$$

where c is the speed of light and bw the the bandwidth of the radar waveform. Increasing the bandwidth, therefore leads to a higher range resolution. In a bistatic radar configuration, the range resolution also depends on the bistatic angle β [69]:

$$\Delta R_{bi} = \frac{c}{2bw} cos(\frac{\beta}{2}) = \Delta R_{mono} cos(\frac{\beta}{2}) \tag{4.6}$$

The bistatic range resolution ΔR_{bi} has its maximum in the monostatic case for a bistatic angle of $\beta = 0°$. In the measurements performed for this thesis, a radar waveform with a bandwidth of 100 MHz was radiated. In the monostatic case this leads to a maximum range resolution of 1.5 m.

4.1.5 The Bistatic Doppler

In this thesis only the stationary bistatic case is considered, where the transmitter and receiver unit are located stationary on the ground. For such a bistatic radar setup, where transmitter and receiver are not moving, the geometry of a moving abject within the illuminated scene e.g. a flying quadrocopter is shown in Figure 4.4. The moving object's velocity vector has a magnitude of v and aspect angle δ referenced to the bistatic angle β under which the object is illuminated and received.

The resulting Doppler frequency or Doppler shift is then defined as follows [69]:

$$f_D = \frac{2v}{\lambda} cos(\delta) cos(\frac{\beta}{2}) \tag{4.7}$$

where λ is the wavelength according to the center frequency of the transmitted radar waveform and v the radial speed of the moving object. For a bistatic angle of $\beta = 0°$, the Doppler frequency is equivalent to a monostatic radar:

$$f_D = \frac{2v}{\lambda} cos(\delta) \tag{4.8}$$

Whereas, for a bistatic angle of $\beta = 180°$ the forward scatter case occurs. For

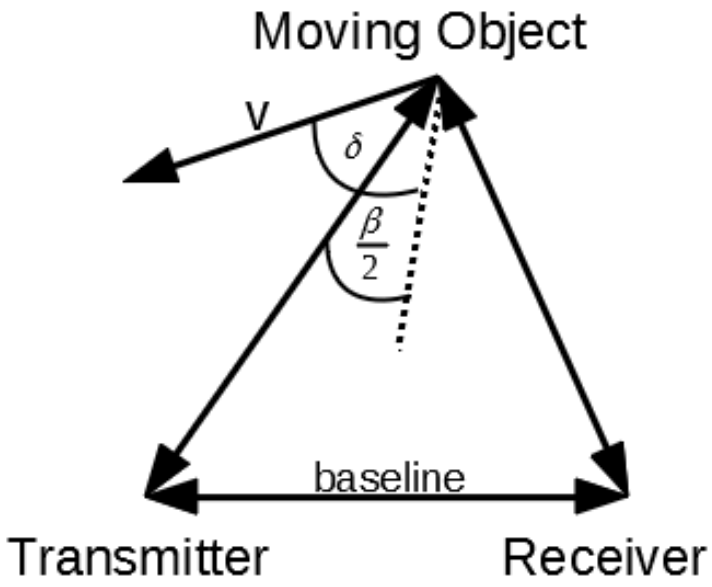

Figure 4.4: Bistatic Doppler geometry [69]

any aspect angle of δ the resulting Doppler frequency then is zero. For aspect angles of $\delta = +-90^\circ$ the the bistatic Doppler is also zero. The maximum Doppler frequency in the bistatic geometry occurs for aspect angles of $\delta = 0^\circ$ and $\delta = 180^\circ$. According to the transmit permission available for the measurements presented in this thesis, a center frequency of 8.85 GHz was chosen. This leads to a wavelength around 3.39 cm. A object e.g. quadrocopter, flying with a speed of 25 $\frac{km}{h}$ under an aspect angle of $\delta = 0^\circ$ is producing a maximum Doppler frequency of 409.72 Hz. Accordingly the presented range-Doppler maps in the chapter **Rural Bistatic Clutter Analysis**, using a quadrocopter as moving object, are cropped to this relevant Doppler range.

4.1.6 Doppler Resolution

The Doppler resolution, the ability of the radar to resolve the Doppler frequency domain, is determined by the coherent processing interval (CPI), the total integration time and the pulse repetition frequency (PRF) of the transmitted waveform. Each row of a single range-Doppler map is the range profile of a single receive pulse with a duration according to the pulse repetition interval (PRI) of the transmitted radar waveform. The inverse of the pulse repetition interval is the pulse repetition

frequency. For a pulsed waveform, the PRI is composed of the pulse on-time T_{on} and off-time T_{off} according to Figure 4.5:

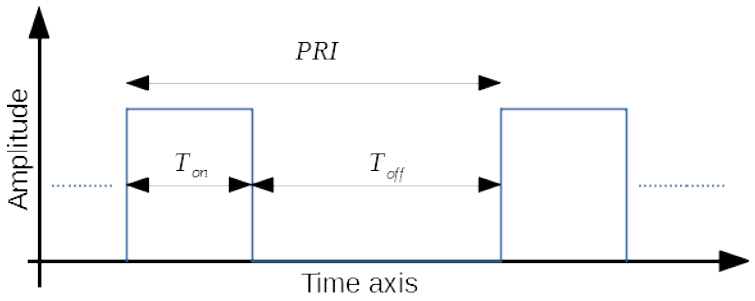

Figure 4.5: Pulse repetition interval of a pulsed waveform

The sampling frequency of the Doppler domain is equivalent to the inverse of the pulse repetition interval:

$$f_{sDoppler} = \frac{1}{T_{on} + T_{off}} = \frac{1}{PRI} = PRF \tag{4.9}$$

where T_{on} is the transmitted pulse on-time and T_{off} the off-time respectively. In the digital domain, the Doppler resolution $df_{Doppler}$ is then determined by the number of pulses N_{pulse} inside a single CPI:

$$df_{Doppler} = \frac{f_{sDoppler}}{N_{pulse}} = \frac{PRF}{N_{pulse}} \tag{4.10}$$

Thus the Doppler resolution can be improved by increasing the CPI or the number of pulses used for integration as well as a decrease of the pulse repetition frequency. However, this happens at the expense of a higher digital memory requirement and an increased processing effort due to the higher number of pulses and a decreased unambiguous range caused by the decreased PRF.

4.1.7 The Bistatic range-Doppler domain

After the basic bistatic parameters such as range and Doppler were explained in the previous sections, the bistatic range-Doppler domain is now introduced. The range-Doppler domain data was the starting point for further clutter analysis in this thesis and will therefore be explained in detail [71]. All presented clutter characteristics in this thesis were derived from the corresponding data of the range-Doppler domain

of the different terrain types and seasons. This domain is commonly presented in the form of a two-dimensional range-Doppler map. One dimension represents the bistatic Doppler frequency in Hertz [Hz] or equivalent speed in meters per second $[\frac{m}{s}]$. The second dimension represents the bistatic range in meters, derived from the measured detour time $\frac{R_R+R_T}{c}$ according equation 4.4 between reference and surveillance signal. The visual representation of a range-Doppler map in logarithmic scale is shown in Figure 4.6. The y-axis represents the bistatic range and the x-axis the Doppler frequency spectrum. The attentive reader should be informed at this point that the bistatic distances are plotted normalized in this thesis. This means that all distances have been reduced by the bistatic baseline and thus start at distance zero in all plots. This serves a better comparability due to the different terrain dimensions and baselines. The bistatic range dimension is also called fast-time [72]. This designation is based on the fact, that the columns of the range-Doppler matrix represent single range profiles. A range profile, in the context of the processing developed for this thesis, is the correlation between a single reference signal and surveillance signal pulse of a dual-channel receiver. So each range profile is sampled with the sampling frequency of the analog-to-digital (ADC) converter. The Doppler dimension is accordingly also know as slow-time dimension. Here, the sampling frequency is the pulse-repetition frequency which is much lower compared to the ADC sampling frequency, $f_{sDoppler} << f_{ADC}$. The range-Doppler domain can be represented as a matrix with M rows according to the number of range bins and N columns according to the number of pulses used for integration. Each cell contains the received energy for a certain range-Doppler pair.

The raw data for the processed and displayed range-Doppler map in Figure 4.6 were recorded with the dual-channel bistatic radar setup used for this thesis and evaluated with the developed coherent signal processing approach. The measurement geometry, including the antenna field of views and the transmitter-receiver distance of $L = 250\,\text{m}$ is shown in Figure 4.7. The resulting bistatic range-Doppler map in Figure 4.6 shows a strong line along the Doppler frequency of 0 Hz. This is the so called Doppler-zero line, representing all stationary object reflections. In the

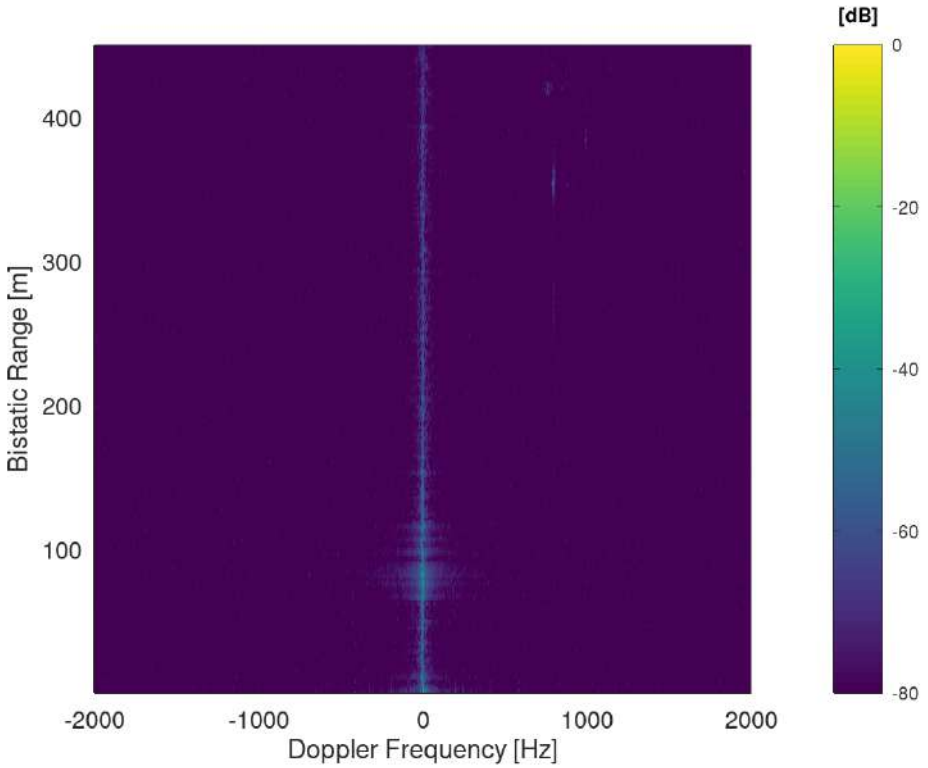

Figure 4.6: The bistatic range-Doppler map of a rural environment with an illuminated a traffic road with several moving cars on it. Range axis is normalized to bistatic baseline.

example, strong scatterers are visible at a bistatic range of 80 m to 120 m. This is a row of trees within the illuminated scene (see Figure 4.7). The trees are moving in the wind, causing a visible Doppler spread. These reflections in the Doppler domain are visible up to a Doppler frequency of 200 Hz. Also some moving cars are visible at a range of 350 m ,360 m and 410 m, with a Doppler frequency of 800 Hz (48.8 $\frac{km}{h}$), 1000 Hz (61.07 $\frac{km}{h}$) and 766 Hz (46.7 $\frac{km}{h}$) respectively. One can already see from this example that strongly disengaged ground clutter leads to a masking of the objects to be detected. The clutter spread generated by the trees has an amplitude similar to that of moving vehicles. At lower distances and speeds, these would no longer be detectable.

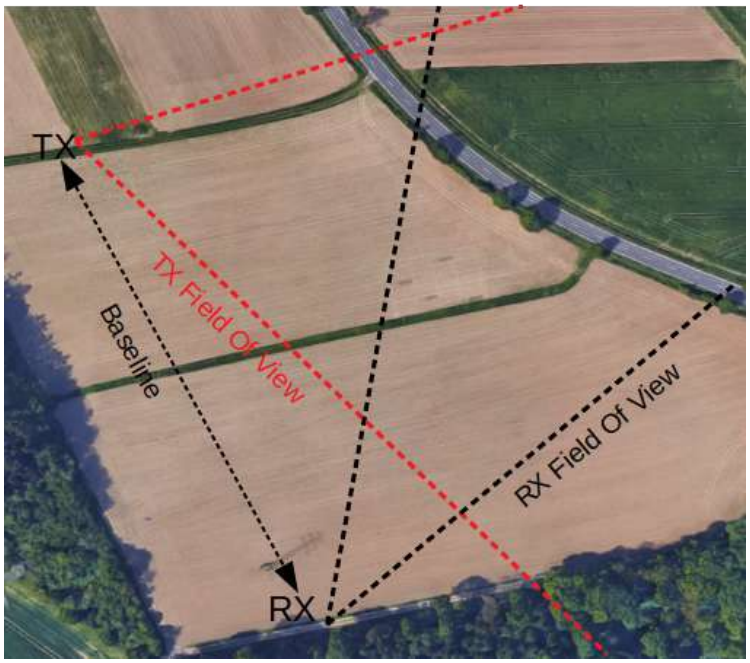

Figure 4.7: Carried out bistatic measurement in a rural environment, illuminating a traffic road with several moving cars on it.

4.2 Bistatic Clutter

In the terminology of a radar, unwanted signal reflections are called clutter. These signal reflections may occur by any object inside the illuminated area. The bistatic clutter geometry considering a single transmitter and receiver according to [69] is shown in Figure 4.8 [69].

The vector of the transmit signal $\overrightarrow{TX}$ is impinging on a single clutter scatterer or clutter patch under an elevation of ϕ_{GZ}. This angle is commonly known as grazing angle. In this thesis the special interest is focused on low grazing anlges with $\phi_{GZ} \leq 5°$. This angular range is also of interest for other bistatic radar applications, such as bistatic SAR, because here, due to the geometry, corresponding angular ranges can be generated. The elevation angle of the outgoing scattered signal vector towards the receiver $\overrightarrow{RX}$ is ϕ_{SC}. This angle is for the measurement trials presented in this thesis also limited to $\phi_{SC} \leq 5°$ and can therefore be assumed to be equal to the grazing angle. The bistatic angle according to the clutter patch is then defined as the scalar product between the transmit and scattering vector:

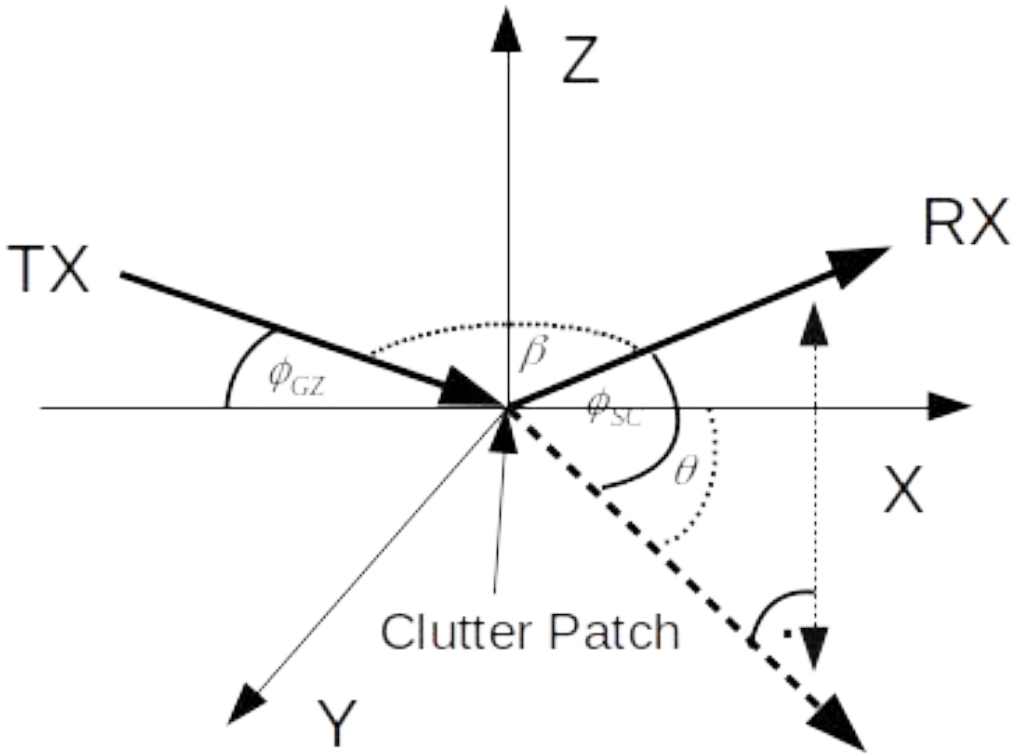

Figure 4.8: The bistatic clutter geometry according to [69].

$$\beta = cos^{-1}\left(\frac{\overrightarrow{TX} \cdot \overrightarrow{RX}}{|\overrightarrow{TX}||\overrightarrow{RX}|}\right) \tag{4.11}$$

Inserting spherical coordinates in Equation 4.11, the bistatic angle can be expressed as follow:

$$\beta = cos^{-1}(sin(\phi_{GZ})sin(\phi_{SC}) - cos(\phi_{GZ})cos(\phi_{SC})cos(\theta)) \tag{4.12}$$

The out-of-plane angle θ is lying in the same plane as the bistatic angle β for small, negligible elevation and scattering angles. Then, equation 4.12 simplifies to [69]

$$\beta = 180^\circ - \theta \tag{4.13}$$

In the field of bistatic clutter, often the out-of-plane angle θ is presented, to determine whether the measurements have been carried out in-plane ($\theta = 0$) or out-of-plane ($\theta = 0^\circ$). The bistatic clutter measurements carried out within the scope

of this thesis have all been carried out-of-plane.

Another import parameter is the clutter cell area, defined as the intersection of the range and Doppler cell with the mainbeam footprint. Whereas the range and Doppler cells are defined by the bistatic iso-range and iso-Doppler contours, the mainbeam footprint is the covered clutter surface [73]. In general, this value and thus also the clutter cell area is a calculated value that may deviate significantly in reality. Antennas with their frequency dependent pattern radiate and receive of course also outside the defined 3 dB beamwidth, used for the definition of the beamwidth. So, in general, the clutter cell size is a numerically determined value. At this point the author refers to the relevant literature [73]. The PhD thesis in [74] especially addresses the problem of bistatic clutter cell size for sea clutter measurements and the numerical approaches. In the simplest case the cell size can be considered as beamwidth-limited. For small grazing angles as assumed in this thesis below 5°, a two-dimensional approximation as a parallelogram results, taking into account the cross-range dimension of the transmit and receive antennas. In the measurements performed, the numerically determined cell sizes have been varied between 198 m-225 m and 120 m-314 m in the cross-range dimensions. For the interesting bistatic angle range from 60° to 80° the cell sizes of the single measurements were comparable for the different types of rural terrain. It is to be clarified once again that the exact determination and setting at this point is almost impossible with real hardware. Important was a qualitative comparability of the single measurements whereas for each terrain the geometry has been adapted accordingly. The following Fig. 4.9 is intended to show some of the relevant factors also influencing bistatic clutter measurements by means of a mindmap. The aim is to illustrate how complex and extensive a holistic recording of the clutter properties is for different parameter sets. Of course, this cannot be done in a single dissertation and was not the goal.

The results presented in this thesis are therefore only valid for a small, fixed set of parameters. It is important to note that the results were obtained only for a bistatic angular range from 60° to 80°. All following diagrams refer to the averaged

Figure 4.9: Some of the relevant factors influencing bistatic clutter measurements to illustrate the complexity and scope of such measurements.

range-Doppler values corresponding to this angular range.

4.3 Chapter Summary

This chapter tried to show the necessary basics of bistatic radar geometry. The comparison with the monostatic geometry should show the much higher complexity, both in hardware and processing. Important bistatic radar parameters have been introduced. This should make clear which advantages the approach of a dual-channel signal processing, adapted to a dual-channel receiver, proposed in this thesis has compared to a conventional monostatic or even bistatic setup. The use of a dedicated reference channel to receive the transmitted signal is a much more efficient solution for bistatic clutter measurements compared to cabled solutions between

transmitter and receiver. In addition, a much more flexible measurement operation is possible, since the transmitter and receiver units can be positioned anywhere around a site. Initial measurements were presented to show the different characteristics of a range-Doppler map. These are important to characterize and model the occurring clutter. The observed terrain or the clutter patch has a special geometry, which has been presented and is necessary for the evaluation of the results. It was also shown how dependent clutter measurements are on numerous parameters, which is the reason why a holistic description within a single thesis cannot be target-oriented.

Chapter 5

Descriptive Bistatic Rural Clutter Statistics

This chapter describes the statistical analysis methodology and parameters used to describe the ground-based bistatic clutter for the different rural terrain types and seasons. The clutter analysis is performed on the range-Doppler domain data. From the processed range-Doppler maps, those range-Doppler bins corresponding to an angular range of 60° to 80° were individually averaged and recorded over the sampling duration for further analysis. This knowledge is important to be able to classify the later results.

The range-Doppler maps reduced in bistatic range and Doppler to the dominant clutter region were evaluated using various statistical parameters. Corresponding to the terrain dimensions chosen for the measurement trials, the range-Doppler maps were cropped in bistatic range up to 500 m and in Doppler to 1.18 kHz. Accordingly these results in a maximum number of 333 range bins and 193 Doppler bins used to reduce the amount of data for the further evaluation. Only the amplitude values of the clutter patches were used for the analysis. Then the range and Doppler bins corresponding to a bistatic angle range from 60° to 80° have been average individually for each cropped range-Doppler map and over the total sampling duration. Then the values are normalized to the corresponding mean value for better comparison because of the different damping factors caused by the terrain dimension. Histograms are calculated for the approximation of the probability density function. Using cumulative summation, from the histogram values the cumulative distribution functions are approximated. Other relevant parameters are explained in the following sections

5.1 Skewness

The skewness is used to describe the asymmetry of the distributions for different types of terrain and seasons. It can be used to quantify whether the majority of the clutter values are accumulated to the right or left of the mean value. The mean value was set to zero for all observations in favour of better comparability. The skewness for the cropped range-Doppler map $c[mn]$, with m being the range bin index and n being the Doppler bin index, is calculated as follows:

$$s_{bias} = \frac{\frac{1}{MN}\sum_{m=1}^{M}\sum_{n=1}^{N}(c[mn]-\bar{c})^3}{\left(\sqrt{\frac{1}{MN}\sum_{m=1}^{M}\sum_{n=1}^{N}(c[mn]-\bar{c})^2}\right)^3} \tag{5.1}$$

where $c[mn]$ is the clutter amplitude value at position m,n in the cropped range-Doppler map, $\bar{c}$ the two-dimensional mean amplitude value of the clutter patch, M the number of bistatic range bins and N the number of Doppler bins corresponding

to a bistatic angle range from 60° to 80°. Because the above calculated skewness value is biased a correction is applied to calculate the unbiased skewness according to the following formula:

$$s = \frac{\sqrt{MN(MN-1)}}{MN-2} s_{bias} \tag{5.2}$$

A negative skewness value indicates that most of the values are on the right side of the mean value. Accordingly the histogram of the data will show a longer tail to the left. A positive skewness value is indicating that most of the clutter values are on the left side of the data mean value. In this case, the hisotgram would show a longer tail to the right.

5.2 Kurtosis

The kurtosis is another statistical parameter quantifying the histogram appearance of a data series. The kurtosis can also be interpreted as an indicator for the dynamic range of the terrain clutter. A higher value describes a higher concentration of clutter amplitudes around a certain value and thus a lower dynamic range. The kurtosis of a clutter distribution is defined as follows:

$$k_{bias} = \frac{\frac{1}{MN} \sum_{m=1}^{M} \sum_{n=1}^{N} (c[mn] - \bar{c})^4}{\left(\frac{1}{MN} \sum_{m=1}^{M} \sum_{n=1}^{N} (c[mn] - \bar{c})^2 \right)^2} \tag{5.3}$$

where $c[mn]$ is the clutter amplitude value at position m,n in the cropped range-Doppler map, $\bar{c}$ the two-dimensional mean amplitude value of the clutter patch, M the number of bistatic range bins and N the number of Doppler bins corresponding to a bistatic angle range from 60° to 80°. The calculated biased kurtosis value can be corrected to the unbiased value as follows:

$$k = \frac{MN-1}{(MN-2)(MN-3)} ((MN+1)k_{bias} - 3(MN-1)) + 3 \tag{5.4}$$

5.3 Interquartile Range

Another parameter to quantify the clutter properties is the interquartile range (IQR). The IQR is also an indicator for the dynamic range between the 75% and 25% percentiles of the clutter data neglecting the values with low probability of occurrence:

$$IQR = c_{75\%} - c_{25\%} \tag{5.5}$$

where c is a $1 \times MN$ vector which results by reshaping the MxN clutter region corresponding to a bistatic angle range from 60° to 80°. This measure of variability indicates the spread of the normalized clutter amplitude values for the different terrain types. This definition for the dynamic range of a terrain does not consider any outliers in the clutter amplitudes and is therefore suitable for a better comparison of the characteristics between the different rural terrain types and seasons.

5.4 Standard Deviation

A further parameter to characterize the terrain is the standard deviation of the clutter amplitudes within the reduced range-Doppler map $c[mn]$ corresponding to a bistatic angle range from 60° to 80°, defined as:

$$\sigma = \sqrt{\frac{1}{MN-1} \sum_{m=1}^{M} \sum_{n=1}^{N} (c[mn] - \bar{c})^2} \tag{5.6}$$

Together with the interquartile range, the standard deviation can be interpreted as some kind of clutter dynamic range measure. Compared to the IQR, outliers are considered within the calculation, resulting in higher clutter dynamic ranges. In the author's opinion, however, both parameters are essential for describing the properties.

5.5 Pearson Correlation Coefficient Analysis

The Pearson correlation coefficient (PCC) [75] is used in this thesis to quantify the similarities between the different histograms and their appearance. So, this quantity can be used for classification purposes. The idea is to correlate the different clutter histograms against each other, in order to show correlations between different types of terrain and seasons. The PCC between two histograms h_i and h_j can be computed as follows:

$$r_{h_i h_j} = \frac{\sum_{m=1}^{M}(h[m]_i - \bar{h_i})(h[m]_j - \bar{h_j})}{\sqrt{\sum_{m=1}^{M}(h[m]_i - \bar{h_i})^2 \sum_{m=1}^{M}(h[m]_j - \bar{h_j})^2}} \tag{5.7}$$

The PCC can take values between -1 and 1. A value of $r_{xy} = -1$ is indicating a negative linear correlation between the histogram pairs and a value of $r_{xy} = 1$ a positive linear correlation. A PCC value of $r_{xy} = 0$ indicates no correlation between a certain pair of rural terrain or seasonal influence.

Calculating the PCC between different histograms of different terrain types, can be used for classification purposes as will be shown in the presented analysis in chapter **Rural Bistatic Clutter Analysis**. In Figure 5.1 a graphical representation for the correlation of two histogram data sets is shown in simplified form. These can be data from different types of terrain as well as from different seasons, e.g. summer and winter. A linear correlation, no matter whether positive or negative, thus allows correlations to be identified. This is also confirmed in the later results.

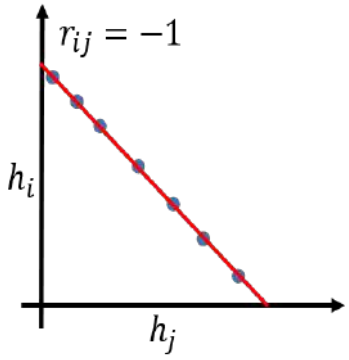

(a) Total negative correlation between histogram values.

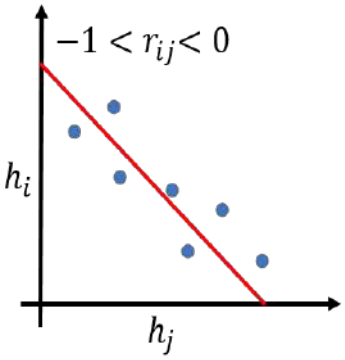

(b) Negative correlation between histogram values.

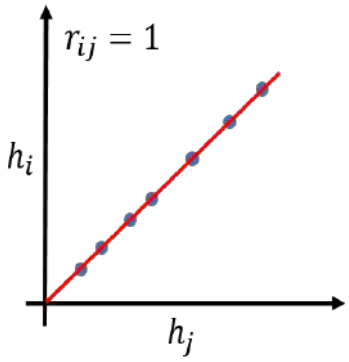

(c) Total positive correlation between histogram values.

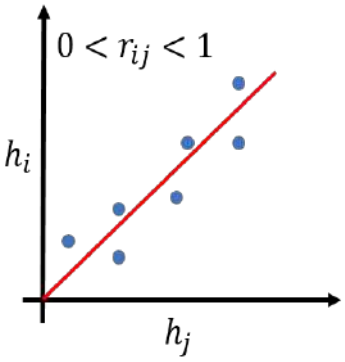

(d) Positive correlation between histogram values.

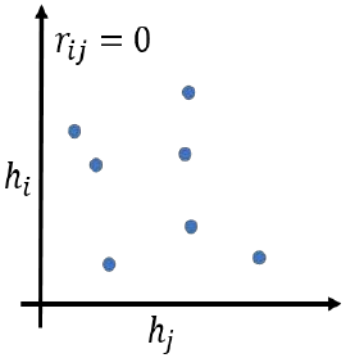

(e) Uncorrelated histogram values.

Figure 5.1: Visualization of the correlation coefficient r_{ij} between histograms h_i and h_j of different terrain types and seasons. (a) total negative linear correlation and (b) negative linear correlation between the histogram pairs, (c) total positive linear and (c) positive linear correlation between the different terrain data. (e) uncorrelated histogram data.

5.6 Weibull Probability Density and Distribution Function

At this point, results are anticipated and the knowledge is listed that the clutter amplitudes can be assigned to a Weibull distribution. A corresponding validation of the Weibull fit is given in the chapter **Rural Bistatic Clutter Analysis**.

The Weibull density function is a continuous density defined by two parameters, namely the shape parameter k and the scale parameter λ. The Weibull probability density function (PDF) is defined as follows:

$$f(x;\lambda,k) = \begin{cases} \lambda k x^{k-1} e^{-\lambda x^k} & \text{for } x \geq 0 \\ 0 & \text{for } x < 0 \end{cases} \tag{5.8}$$

With the same parameters, the Weibull cumulative distribution function (CDF) is defined as follows:

$$F(x;\lambda,k) = \begin{cases} 1 - e^{-\lambda x^k} & \text{for } x \geq 0 \\ 0 & \text{for } x < 0 \end{cases} \tag{5.9}$$

Depending on the choice of the shape parameter k, the Weibull distribution can be transformed into an exponential distribution (for $k = 1$) or a Rayleigh distribution (for $k = 2$). It therefore offers the advantage of a better comparability of the results presented in this thesis, since several similar distributions do not have to be evaluated against each other. The Weibull PDF and CDF are then used to analytically describe the clutter density and distribution functions approximated by the histograms of the different types of terrain and seasons. Applying maximum-likelihood estimation to the computed histogram values for each terrain type, the scale and shape parameter can be estimated. The likelihood function to Equation 5.8 results in:

$$L(\lambda,k) = \prod_{i=1}^{N} f(x_i,\lambda,k) = \lambda^N k^N (\prod_{i=1}^{N} x_i)^{k-1} e^{-\lambda \sum_{i=1}^{N} x_i^k} \tag{5.10}$$

where N is the number of histogram bins used to estimate the PDF and $x_i = h[i]$ the according normalized histogram bin count. Taking the natural logarithm, the log-likelihood function for the parameter estimation is defined as follows:

$$ln(L(\lambda,k)) = Nln(\lambda)Nln(k) + (k-1)\sum_{i=1}^{N} ln(x_i) - \lambda \sum_{i=1}^{N} x_i^k \tag{5.11}$$

To determine the required parameters from the log-likelihood function, the partial derivatives must be formed. Taking the partial derivatives of (5.11) and equating them to zero

$$\frac{\delta}{\delta\lambda} ln(L(\lambda,k)) = 0 \tag{5.12}$$

$$\frac{\delta}{\delta k} ln(L(\lambda,k)) = 0 \tag{5.13}$$

results in the estimates for the scale and shape parameter. The partial derivatives can than be solved numerically for $\hat{\lambda}$,$\hat{k}$, which are the final estimates of the scale and shape parameter. Both parameters completely describe the Weibul PDF and the Weibull CDF.

5.7 Chapter Summary

This chapter describes the main statistical parameters for characterizing the properties of the bistatic clutter occurring in different types of terrain. Starting with the processed data from the range-Doppler domain, the clutter analysis is performed. The method presented in this thesis is based on the evaluation of the clutter data directly in the range-Doppler domain averaged for the range-Doppler bins according to a bistatic angle from 60° to 80° instead of only for single range cells of a range profile. The applied measurement methodology also ensures that the relevant clutter data is located in the same range-Doppler region. For this purpose, the measurements were performed on comparable large areas of terrain. The histograms, as initial estimates of the probability density function and the corresponding cumulative distribution functions can be analytically described using parametrizable

Weibull distributions. By means of a maximum-likelihood estimation the necessary parameters can be determined from the histogram data. Correlation analyses are used for similarity analysis between histogram appearance in order to show correlations between different types of terrain and seasons. In particular, the correlation properties of clutter statistics for different types of terrain could be of great interest for adaptive radar modes. The further parameters were selected by the author according to relevant statistical parameters, which on the one hand guarantee a comparability of the data for further work and on the other hand allow a synthesis of corresponding random numbers to model the clutter properties.

Chapter 6

Measurement Methodology and Materials

In this chapter, the measurement methodology for performing bistatic clutter measurements and the hardware setup, used and adapted for this purpose, are presented. The way in which the clutter measurements were performed and evaluated represents a new approach. A dual-channel bistatic measurement setup was used for the measurements, where the transmitter and receiver units are externally synchronized via Rubidium standards, ensuring phase and frequency coherence during the measurement trials. Due to the two receiving channels, the transmitter and receiver units can be freely positioned along a rural terrain, without the need for a physical connection between them. Thereby, one receiving channel receives the direct signal emitted by the transmitter, which is needed for the proposed range-Doppler processing, which is the first step of the clutter analysis. Using a dual-channel receiver, the second channel is receiving the clutter components and the developed processing enables an additional phase synchronization to the transmitter phase. Together with the coherent processing, this leads to an improved signal-to-noise ratio. Isolated areas, were selected for the measurements, which are comparable in their dimensions to ensure a uniform coverage of the bistatic angular range. The grazing and scattering angles were selected to be less than 5° degrees during each measurement, an angular range which is of interest for ground-based applications. Compared to other published bistatic ground clutter measurements and analysis for rural terrain,

this thesis derives the clutter properties directly from the bistatic range-Doppler maps. These are reduced to the relevant clutter range. Another reason why the measurements were performed in terrain with comparable dimensions. This kind of measurement using the presented setup and the developed evaluation is a novelty in the field of rural bistatic clutter measurement and evaluation. In addition, relevant types of terrain were surveyed, most of which are found in German rural areas. This classification of dominant sub-terrains allows a much more granular characterization of the different clutter sources. The measurements were carried out in summer and winter in order to characterize the seasonal influence, too. The idea of the subdivision of the rural environment and corresponding percentages of the individual land masses were already published in [1, 5, 6].

6.1 Proposed Measurement Methodology

In this thesis, series of measurements were carried out to characterize the statistical properties of bistatic rural terrain clutter in such a way that the rural environment was not measured holistically but divided into dominant subgroups. The rural environment in which the measurements were carried out is country-specific for Germany or Central Europe, and the subgroups were chosen accordingly. The measurements were carried out with a phase-coherent dual-channel measurement setup. One of the two receiving channels was used to receive the waveform emitted directly from the transmitter. The second receiving channel received the corresponding rural clutter. In order to characterize the clutter with such a hardware approach, a corresponding pulse-based coherent processing is presented in the following sections. It can be assumed that only the relevant clutter is present in the received signals and that no additional object reflections have distorted the measurements.

The observation of a rural German environment divided into its dominant terrain types and their phase coherent measurements thus represent an essential novelty in the field of bistatic clutter analyses. In the following sub-sections, the rural subgroups are first introduced and a justification for their choice is given. Afterwards, the measurement setup and the selected parameters are described. These parameters have been retained for all measurements in order to ensure the comparability of the results. As the measurement data were collected over a period of almost two years, the last sub-chapter shows on which days measurements were taken and which preparatory measurements were necessary. This should make clear once again with which not inconsiderable effort the measurements were carried out to collect the data.

6.1.1 Subgroups of a typical German rural environment

As described in the introduction to this chapter, compared to state-of-the-art analysis, the rural environment was divided into dominant subgroups for clutter analysis [6]. The author has specified the following four dominant types of terrain that

mainly form the country-specific German or Central European rural environment in the region where the measurements have been carried out:

- **Group A**: Fields with low vegetation
- **Group B**: Fields with high vegetation
- **Group C**: Plantations of small trees
- **Group D**: Forest environments

These subgroups are mainly found in the rural environment of the Eifel region in western Germany where the measurements were carried out. This region was also chosen to represent the country-specific clutter analysis, as the Fraunhofer Institute for High Frequency Physics and Radar Techniques FHR has its campus there. For logistical reasons, the proximity to the institute made the extensive series of measurements possible. Group A describes terrain which mainly consists of flat meadows or farmland. Group B describes the terrain types with high vegetation such as cereal or corn fields. Plantations consisting of small trees are described in group C. These are mainly plantations consisting of fruit trees or vines. They are usually arranged in rows. This fact is relevant for the later evaluation and discussion of the results. The fourth group D comprises forests. In the Eifel region these are mainly mixed forests consisting of spruce, oak, beech and pine trees. This type of mixed forest can be regarded as ”evergreen”, as dense vegetation is present both in summer and winter. Figure 6.1 shows a section of the surveyed terrain ([1]). The selected rural subgroups are highlighted in colour. In the figure a landmass of about $9\,km^2$ is shown.

Table 6.1 shows the percentage share of the represented land mass for the four subgroups ([1]). The share was calculated from the above shown image section and put into total relation. It can be seen that the dominant share is covered by group A sites. This is followed by group B and D sites. The smallest part of the total rural landmass is formed by plantations e.g. consisting of small trees with 10,4 % of the

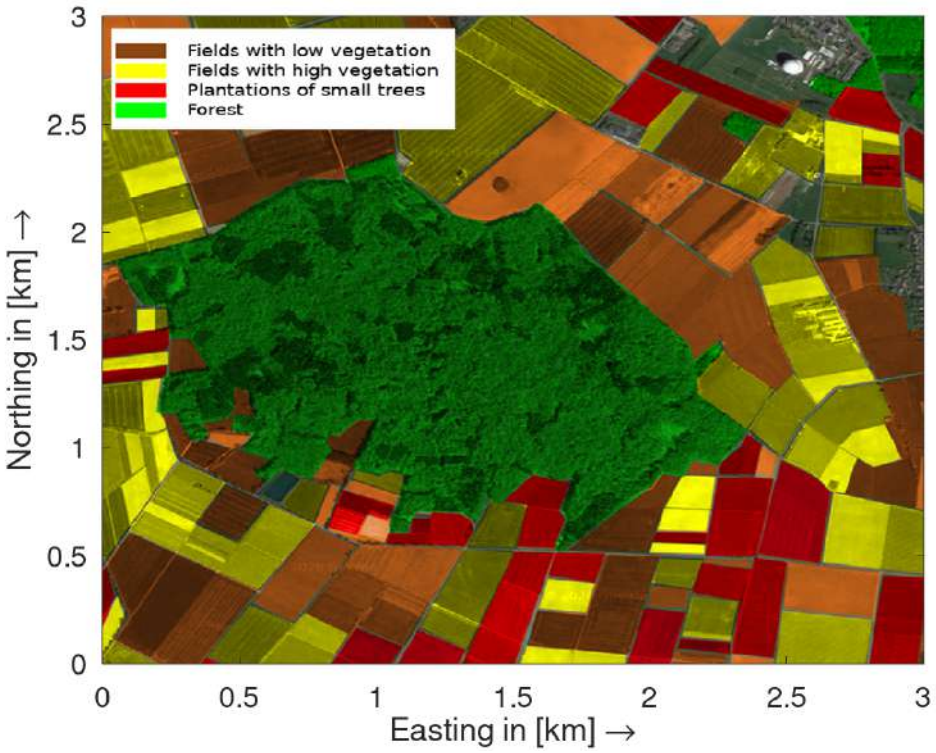

Figure 6.1: Selected rural terrain in the Eifel region in western Germany. The four dominant rural subgroups identified by the author are colour coded. The Fraunhofer FHR as the starting point of each measurement can be seen in the upper right corner ([1]).

total landmass. For the scene shown, about 6 % were covered by other buildings or lakes. According to official data from the German Federal Statistical Office, the proportion of forest areas is 29.8 % [76]. The share of agricultural land is 50.08 % in total. This includes the groups A, B and C selected in this thesis. The official numbers for group A sites show a share of 70.5 %, 27.2 % for group B and 1.2 % for group C [29], [77]. These data represent an average value for the total landmass of Germany. However, these results also correspond to those in Table 6.1. Here, too, the largest share is formed by group A terrain, followed by group B and C. In the official data the share of group C is also the lowest.

Type A	Type B	Type C	Type D	Others
31.8%	22.8%	10.4%	29%	6%

Table 6.1: Percentage of the various types of rural terrain as a proportion of the total landmass for the depicted scene.

The share of the four sub-terrain types indicates that a rural environment can not be seen as a heterogeneous landmass according to the derivation of statistical clutter properties. This fact illustrates the need for subdivision and separate measurements of the different types of terrain presented in this thesis. The targeted measurement of these relevant terrain types both in the summer and in the winter is therefore an important contribution to the bistatic rural ground clutter analysis, since such measurement data have not yet been published for a country-specific German rural environments at the time of writing this thesis. Even monostatic rural ground clutter analyses have not yet been published in such a subdivision for the landscapes under consideration.

6.1.2 Relevant Measurement Parameters

In order to ensure the comparability of data and results, the measurements in the aforementioned rural terrain subgroups were always carried out using the same hardware setup, methodology and parameter set. However, it should be clearly emphasized here that the metrological recording of clutter properties is subject to enormous parameter variation. The results listed here are therefore only valid for the listed hardware, geometry and parameter sets. However, these results represent a basis for further investigations in the field of bistatic clutter investigations. In order to obtain data for the radar-relevant X-band, the measurements were performed at a center frequency of 8.85 GHz, according to the transmit permission. A continuous acquisition of the complete X-band was also not possible due to the limitations of the used hardware and permissions. The limitations of the transmitting power required that the measurements were performed at a reduced scale. This means that terrain areas were selected in such a way that only the vegetation of the desired terrain type was illuminated under the given bistatic baseline to ensure as best as possible that only the clutter caused by the terrain under test has been measured. The bandwidth of the radiated signals was set to 100 MHz, so that the frequencies from 8.8 GHz to 8.9 GHz are covered. Linear frequency modulated pulses were used as waveform with a maximum transmit power adjusted to 30 dBm in accordance with the transmit permission. This value already includes the transmission gain of the

horn antenna used and thus corresponds to the effectively radiated power (ERP) [8]. On the receiving side, the signals were amplified and sampled at a frequency of 250 MHz. The sampling has been performed in the third Nyquist band. This type of sampling eliminates non-linear interference effects near DC (0 Hz). Further parameters regarding the hardware used are given in the following sections. For the measurements, the transmitter and the receiver were placed in such a way that the terrain under test (TuT) to be surveyed has been covered by the transmit and receive antenna beams in a way that at least a bistatic angle range from 60° to 80° has been covered within the illuminated terrain under test containing the desired vegetation. Clutter patches of comparable size were always selected to ensure the comparability of the results. Nevertheless, to make a valid statement about the clutter properties, only the range-Doppler cells for the bistatic angular range from 60° to 80° were evaluated and presented due to the complexity of such measurements, the measured terrain areas and the hardware used. A schematic representation of an exemplary measurement setup is shown in Figure 6.2. The transmitter and receiver units placed around the site are synchronized by an external reference clock to ensure phase coherence. A solution consisting of rubidium oscillators was used after previous investigations to ensure the synchronization [4]. These standards are tuned via GPS signal. Both transmitter and receiver had such a unit built-in and were therefore synchronized with sufficient accuracy of 35 μrad [9]. An investigation of various synchronization techniques can be taken from the publication in [4] that has been created by the author within the scope of this thesis.

To give the reader a better visualization of the hardware used, Figure 6.3 and Figure 6.4 show the transmitter and receiver units set up during an exemplary measurement. The measurement bus with mounted receiver antennas enabled a more flexible measurement procedure. In Figure 6.4 the two antenna, one for the reference signal and the other one for the surveillance signal can bee seen. The elements have been separated by 2 m. Previously, tripods were used for all measurements which required constant assembly and disassembly. For measurements in group A terrain, however, tripods were still used to achieve an antenna height corresponding

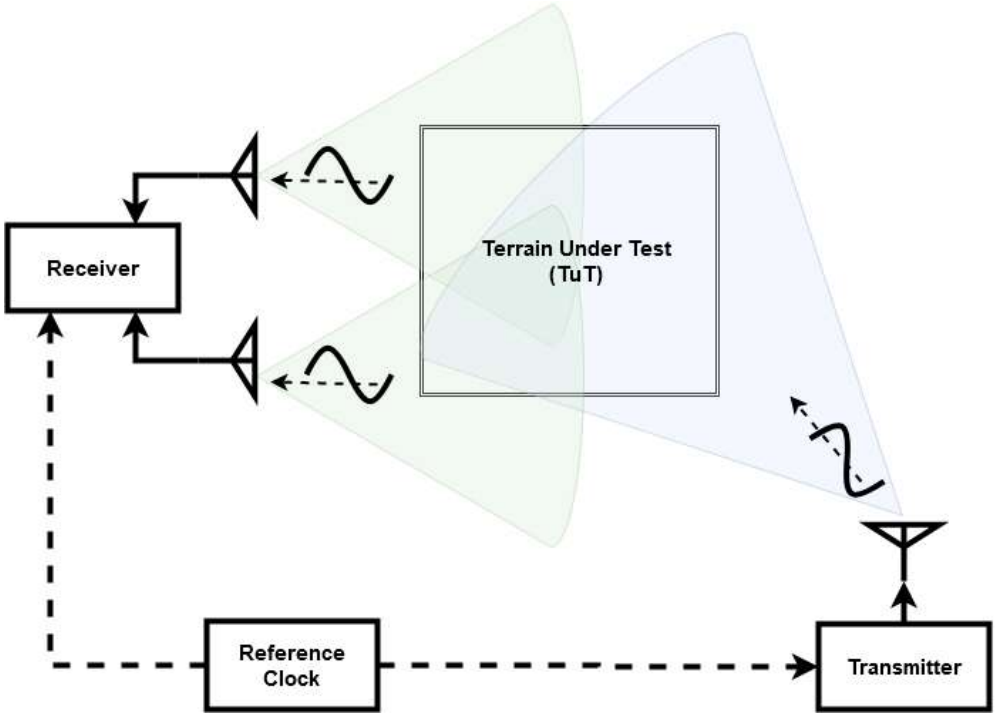

Figure 6.2: Schematic representation of the measurement setup. The transmitter and receiver were arranged with different baselines depending on the terrain (TuT) dimensions and accessibility of the measurement location.

to the desired grazing and scattering angles below 5°.

As mentioned, the maximum distance at which the transmitter and receiver can be set up in relation to each other depends largely on the minimum required reception power that must be applied to the analog-to-digital converter on the receiver side. For the bistatic setup used in this thesis a minimum reception power of -49.92 dBm is necessary. This value is given by the used analog-to-digital converter and represents the absolute limit of the hardware used and was therefore increased by 20 dB. With a maximum radiated power of 30 dBm, a total gain on the receiver side of 46 dB and a minimum received power of -29.92 dBm a maximum bistatic distance of 5.5 km results. In order to determine a maximum range for the baseline between the transmitter and receiver from these values, the bistatic angle β at which the measurements were made is also required. Taking into account the above mentioned values, the minimum reception power and the resulting maximum bistatic distance as well as the variation of the bistatic angle, the maximum distance between the transmitter and receiver was limited to 500 m during each measurement

Figure 6.3: The transmitter set up in a cornfield.

trial. The minimum distance is defined by the terrain dimension and was at least 160 m. In order to achieve results relevant for ground-based bistatic radar applications, a grazing angle of below 5 ° was always maintained during the measurements. The scattering angle was chosen accordingly below 5 °. The areas to be surveyed were then selected according to the maximum bistatic distance. It was always ensured that only clutter was present in the received signals. For this purpose, the respective area was optimally illuminated with the transmitting and receiving antennas. In order to suppress the direct signal components efficiently, an optimal alignment of the transmitting antenna and the reference channel antenna was carried out at the beginning of each measurement at the corresponding measurement location. The parameters already mentioned, all further parameters necessary for the verification of the results and for repeating the measurement methodology are listed in Table 6.2.

Parameters given in the table in intervals were adapted to the prevailing terrain conditions for each individual measurement. The mentioned beamwidths for the

Figure 6.4: Bistatic receiver built into a bus for flexible use. The reference and surveillance channel antennas are mounted on the roof and can be aligned according to the terrain.

transmit and receive antenna are related to the measured 3 dB width. Care was taken to carry out all measurements for the respective type of terrain and season in dry conditions and with wind speeds of less than 7 km/h. These restrictions were chosen to ensure comparability of the results for each group of terrain within and between seasons. As wet, rainy and snowy environments as well as too high wind speeds influence the results, these factors were avoided.

6.1.3 Scope of the Measurement Campaigns

The measurements in the different types of terrain were carried out in the years 2019 and 2020. Measurements were made in summer 2019 and winter 2019/2020 to investigate the influence of the seasons on the clutter statistics. For each terrain group A-D, at least four individual measurements have been carried out during each season. Table 6.3 lists the successful measurement campaigns. In addition to the measurements listed there, further measurements were carried out, but these did

Measurement Parameter	**Value**
Center Frequency	8.85 GHz
Transmit Antenna Beamwidth	28 °
Receive Antenna Beamwidth	36 °
Transmit Power (total) $P_T G_T$	30 dBm
Receiver Gain (total) G_R	46 dB
Bandwidth	100 MHz
Range Resolution	1.5 m
CPI (in Pulses)	8192
Doppler Resolution	6.103 Hz
Pulse On-Time	15 μsec
Pulse Off-Time	5 μsec
Polarization Transmit Antenna	Vertical
Polarization Receive Antennas	Vertical
Tx-Rx Baseline Variation	160 m - 500 m
Bistatic Angle Variation	at least 60 ° - 80 °
Grazing Angle ϕ_{GZ}	$< 5°$
Scattering Angle ϕ_{SC}	$< 5°$
Sampling Frequency	250 MHz
ADC Number of Bits	8
Nyquist Band	3
Windspeed	$< 7 \frac{km}{h}$

Table 6.2: Measurement parameters applied to each single measurement campaign. Variable parameters have been adapted to the terrain conditions.

not yield any usable data. The reasons for this were mostly due to hardware defects. The measurement setup used is made up of laboratory components that were not designed for such intensive measurement use. In the course of the years 2019 and 2020, a wide variety of hardware defects and unusable data occurred time and again. In addition, measurement campaigns were carried out to investigate different approaches to synchronize the transmitter and receiver for phase coherent measurements. These took place in 2018 as preparation and are also not listed. Also, in 2018, the necessary hardware tests took place in the open field in preparation for the actual measurements. Table 6.3 lists the measurement campaigns that produced data suitable for further processing. According to the listed dates, the measurements with the numbers 1 to 16 correspond to the summer measurements. The measurements with the numbers 17 to 26 form the winter measurements. The scope of

Number of Measurement	Date of Measurement	Group of Terrain
1	12.04.2019	A
2	16.05.2019	B
3	28.05.2019	C
4	29.05.2019	D
5	06.06.2019	A
6	27.06.2019	B,*
7	02.07.2019	C
8	12.07.2019	D*
9	23.07.2019	A
10	31.07.2019	B
11	12.08.2019	C*
12	22.08.2019	D
13	30.08.2019	A*
14	22.10.2019	B
15	24.10.2019	C
16	25.10.2019	D
17	13.11.2019	A
18	25.11.2019	C
19	26.11.2019	D,D
20	29.11.2019	A
21	05.12.2019	C,C
22	04.12.2019	D
23	10.12.2019	A
24	18.02.2020	C
25	19.02.2020	D
26	17.03.2020	A

Table 6.3: Measurements sorted by date in the years 2019 and 2020.

winter measurements is smaller, since group B sites, fields with high vegetation, are not present in winter. In addition to the measurements listed here, four separate measurements were taken to investigate the detection performance of a bistatic radar under the influence of rural ground clutter. These measurements also took place in summer 2019. The corresponding measurement days are marked with ”*”.

The individual types of terrain were measured according to an alternating pattern. Measurements for the spring and autumn seasons were not explicitly carried out. In order to be able to derive valid statements regarding clutter properties from the measured data for these seasons as well, the already very extensive measurement effort would have had to be significantly increased. The individual measuring days

shown and the corresponding number of measurements not listed further illustrate the great measuring effort put into the preparation of the results presented in this thesis and supported by Fraunhofer FHR with all means.

6.2 Materials

In the following sub-sections, the bistatic measurement setup, consisting of a transmitter and a dual-channel receiver developed by Fraunhofer FHR, which was compiled and used for the execution of experiments, is presented. The research work here consisted mainly in the synchronization of the used bistatic nodes.

6.2.1 The Used Bistatic Radar Setup

The transmitting and receiving nodes used for the bistatic radar setup were developed and built by Fraunhofer FHR in the context of other projects. For the measurements needed within the scope of this thesis, these were then combined to a bistatic setup and used for the measurements. In addition, extensive tests on the external synchronisation of the nodes were carried out within the scope of this thesis. In order to understand the measuring principle, the hardware provided by Fraunhofer FHR is presented in the following.

In order to be able to collect data for a statistical bistatic ground clutter analysis, a bistatic measurement setup was used. The setup consists of a transmitter and a bistatic dual-channel receiver developed by Fraunhofer FHR. Since a direct decoupling of the signal on the transmitter side is not possible due to hardware limitations, one receiving channel is used to receive the direct signal and the second channel to receive the clutter echoes of the terrain under test for further processing. Synchronization between the transmitter and receiver was ensured using GPS disciplined rubidium clocks. Using an external reference signal generation, enables phase coherent measurements resulting in a higher signal-to-noise ratio. In the following, the schematic diagrams of the transmitter and receiver are presented.

6.2.1.1 The Dual-Channel Bistatic Receiver

In Figure 6.5 the structural diagram of the dual-channel bistatic radar receiver, developed by Fraunhofer FHR is shown. The receiver used here was developed by Fraunhofer FHR as part of another project [78]. The receiver is designed for the X-band and can receive signals with a bandwidth of 100 MHz using a tunable local

oscillator. Both receiving channels have an identical front-end design. Behind the receiving antenna, a limiter protects the following hardware from being damaged by too high reception power. This could be the case in terrain where a strong direct signal component is available during the bistatic radar measurement e.g. a field with low vegetation.

A quad-Vivaldi antenna element arrangement was used as antenna, both for the reference and surveillance channel antenna. After the antenna, the signals are amplified using a low noise amplifier (LNA). The LNA ensures the amplification of very weak signals without significantly degrading the signal-to-noise ratio (SNR). A reduction of the SNR and thus of the dynamic range would otherwise lead to weak reflections of e.g. a quadrocopter no longer being detectable. After the LNA the signals are down-converted to a fixed intermediate frequency using a common local oscillator signal for both received channels. For the measurements the down-converted intermediate frequency was set 300 MHz. After subsequent filtering with a bandwidth of 100 MHz for frequency image suppression and further amplification, the signals are sampled in the third Nyquist band at a sampling rate of 250 MHz. This sampling technique minimizes interference effects near DC and results in spectral folding of the down-mixed signal to the frequency range from 0 MHz to 100 MHz. The resolution of the analog-to-digital converter was limited to eight bits. So the dynamic range at the ADC was limited according the following formula [79]:

$$\text{Dynamic Range in [dB]} = 6.02\text{Number Of Bits} + 1.76\,dB = 49.92\,dB. \quad (6.1)$$

Due to the dynamic range determined by the hardware, it was necessary to ensure that the reference signal was received sufficiently attenuated in the surveillance channel during the bistatic measurements. This was done by aligning the two receiving antennas individually according to the terrain conditions of the type of terrain to be measured. Before the actual bistatic measurements, a power measurement was carried out in each of the individual receiving channels. The antennas

mounted on the measurement bus were only 2 m apart. This difficulty was accepted for a more efficient measurement. It should be mentioned, that the dynamic range after the ADC can be increased by the processing gain. This gain depends on the number of received radar pulses used for coherent radar processing. The hardware setup was chosen to achieve a maximum dynamic range together with the radar processing. Due to the power limitations imposed by the transmit permission, only very weak reflections can be measured, depending on the terrain attenuation.

This part of the page intentionally left blank.

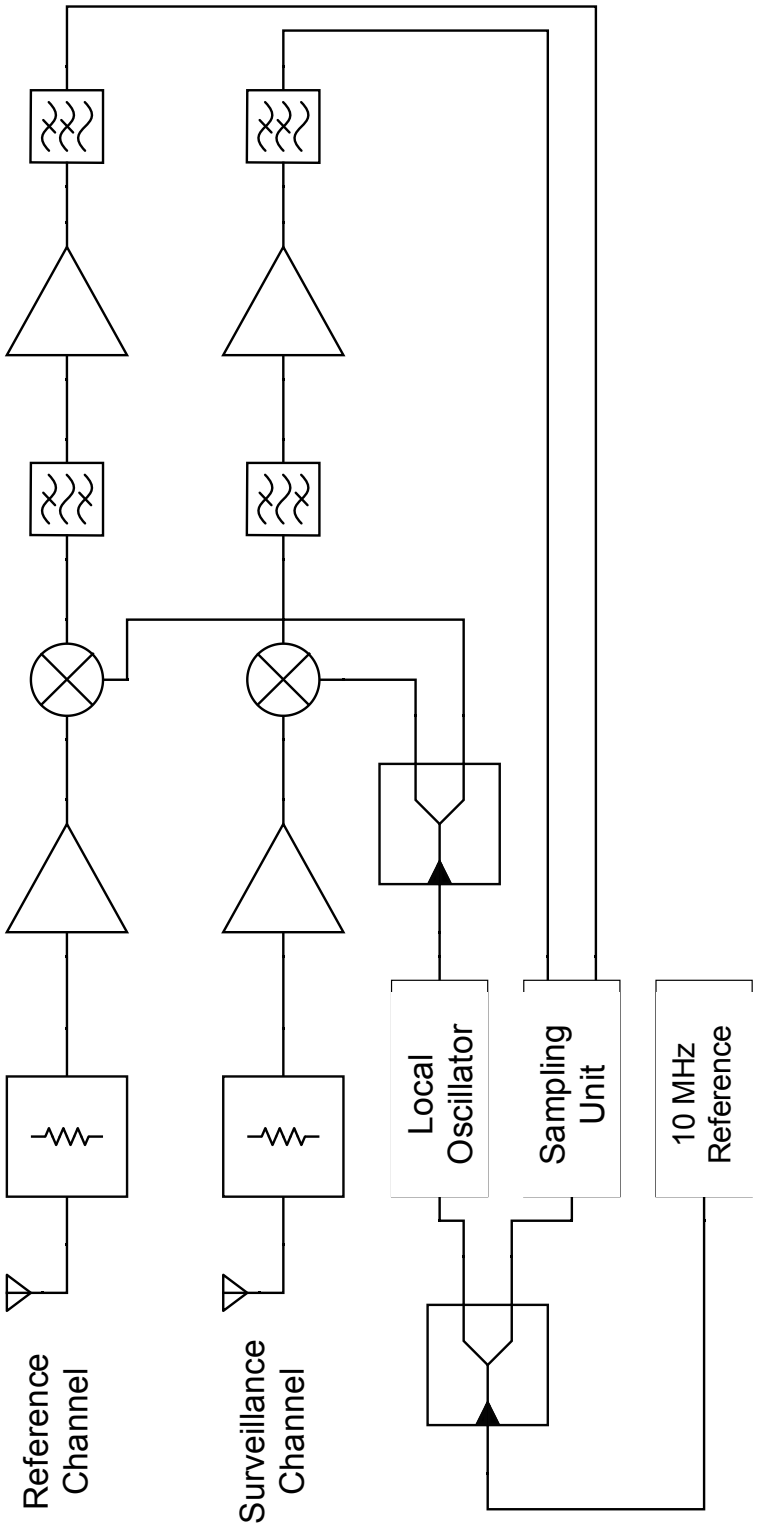

Figure 6.5: The dual-channel receiver developed by Fraunhofer FHR for the bistatic radar measurements with a reference channel for the reception of the direct signal and a surveillance channel for the clutter reception.

As can further be seen in Figure 6.5, there are two independent clock sources in the receiver design. The common local oscillator for down-conversion and the the sampling frequency of the analog-to-digital converter. All clock sources are synchronized over a 10 MHz reference which is generated by a GPS disciplined rubidium standard. This ensures phase coherency between the transmitter and receiver [4]. In Figure 6.6 the Fraunhofer FHR hardware demonstrator is shown.

Figure 6.6: The dual-channel receiver developed by Fraunhofer FHR.

6.2.1.2 The X-band Transmitter used as Illuminator

Since in a bistatic radar configuration the transmitter and receiver are spatially separated, a corresponding transmitter unit developed by Fraunhofer FHR has been used. Figure 6.7 shows the transmitter schematic of the bistatic radar setup. The transmitter is designed for the X-band and can transmit arbitrary waveforms with a bandwidth up 100 MHz and a power of 30 dBm. A horn antenna is used as transmit antenna. The radar signals are generated by the arbitrary waveform generator (AWG) in the baseband. The digitally generated radar waveforms are uploaded to

the AWG. After digital-to-analog conversion and before up-conversion filtering is necessary to remove resulting frequency images created by the AWG. After up-conversion to the desired center frequency of 8.85 GHz, the frequency images due to the conversion operation are filtered and the signals are amplified. The amplifier is needed to compensate the conversion-loss introduced by the mixing stage. The last amplifier stage is a power amplifier directly attached to the antenna ensuring the desired transmit power.

The complete frequency range from 8 GHz to 12 GHz can be covered with the transmitter. However, this is not possible simultaneously or in scanning mode at the time the experiment was carried out. A fixed local oscillator frequency therefore must be set at the beginning of a measurement. During the measurements, the signal generated by the AWG was always up-converted to a center frequency of 8.85 GHz according to the transmit permission. Therefore a local oscillator frequency of 7.9 GHz had to be set. The baseband signals were output by the AWG at a center frequency of 950 MHz. The digital-to-analog converter (DAC) had a cut-off frequency of 10 GHz. Previous measurements identified this frequency range as particularly suitable.

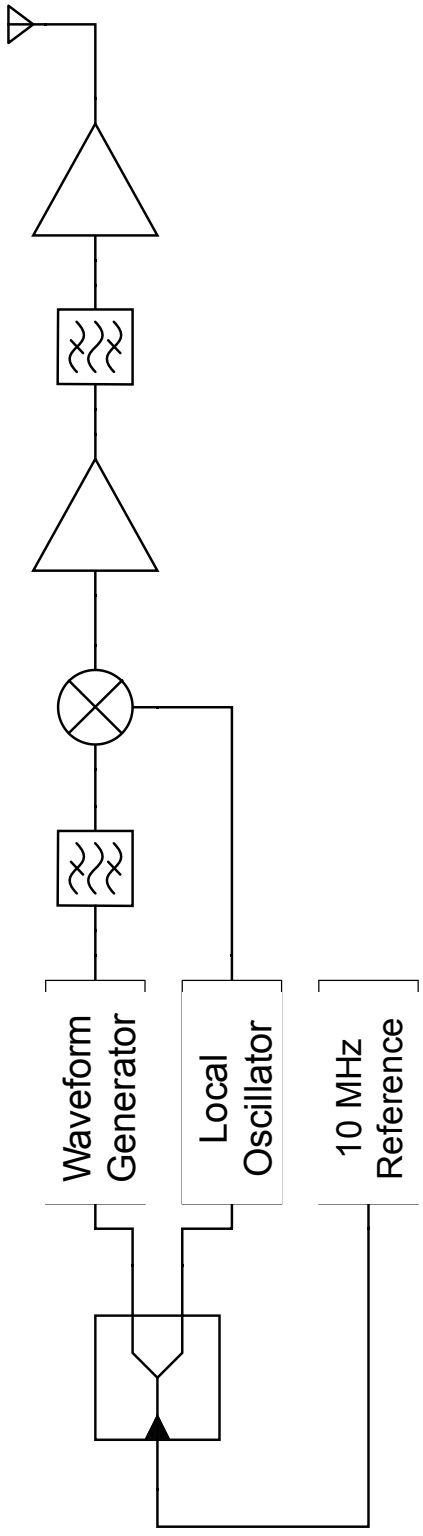

Figure 6.7: The structural schematic of the X-band transmitter developed by Fraunhofer FHR used as illuminator for the bistatic radar measurements.

Both the local oscillator and the AWG digital-to-analog converter are referenced by an external 10 MHz signal and are thus synchronized with the receiver to ensure phase coherency during the measurements. In Figure 6.8 the transmitter is shown. On top of the transmitter unit, the Rubidium standard is located.

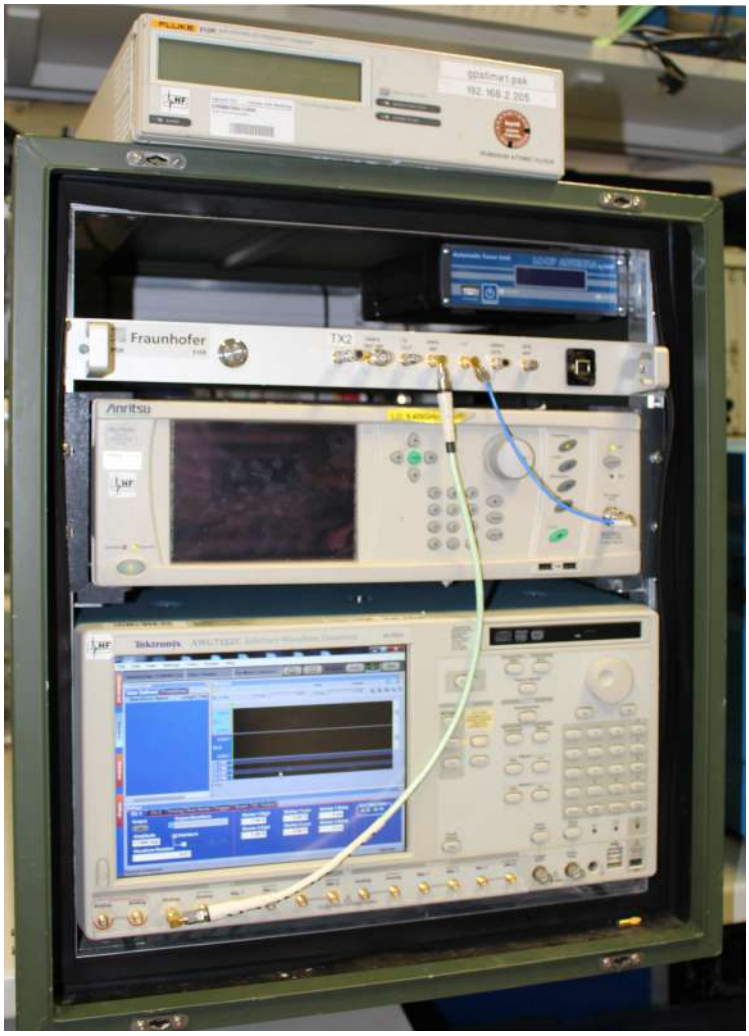

Figure 6.8: The transmitter unit for the bistatic radar measurements developed by Fraunhofer FHR. On top of the green box the Rubidium standard is located, providing the external generated 10 MHz signal.

The structure presented here, consisting of a transmitter and a receiver, offers the advantage that no physical connection between the transmitter and receiver unit is required. This is normally necessary to transmit the transmitted signal to the receiver for radar processing. Since a dual-channel approach is used here, the signal

emitted by the transmitter is received directly via one of the two receiver channels [80]. This results in a significantly simplified hardware architecture for the receiver, as no additional signal transmission takes place.

6.2.2 The measurement signal

For the bistatic radar measurements a pulsed waveform with a linear frequency modulation was used [81]. This waveform is also known as chirp. The advantage of such a waveform is the energy spread over a wider bandwidth. This allows short and powerful pulses to be replaced by longer modulated transmission pulses with lower amplitude. The spread bandwidth then leads to pulse compression in signal processing after cross-correlation to generate the range profile. This results in clear correlation maxima.

Since the range resolution is related to the inverse of the measurement bandwidth, with such a signal it is more efficient to cover the desired bandwidth. The advantage of this waveform is also due to its immunity to interference. A linear frequency modulated signal contains only one frequency component at a time and is therefore much more robust against intermodulation effects of the hardware [82]. Signals that have several frequency components at any given time, e.g. Orthogonal Frequency-Division Multiplexing (OFDM) waveforms require a very linear behaviour in the amplifiers and mixing stages. Otherwise, artifacts are caused by the third-order intermodulation products [83]. The requirements result in considerably higher costs for the components. For this reason, a linear frequency modulated waveform was chosen for the bistatic radar design in this thesis to keep the costs and requirements of the hardware low. The pulsed signal x_{tx} used is defined as follows:

$$x_{tx}(t) = \begin{cases} Asin(2\pi(F_0 t + \frac{F_1 - F_0}{2T_{chirp}} t^2)) & \text{for } 0 \leq t \leq T_{chirp} \\ 0 & \text{for } T_{chirp} < t \leq T_{chirp} + T_{off} \end{cases} \tag{6.2}$$

where F_0 and F_1 are the start and stop frequencies of the signal. The bandwidth

is defined as the difference between both frequencies to $bw = F_1 - F_0$. The time duration within the signal needs to linearly increase the frequency from F_0 up to F_1, is the duration T_{chirp}. The scaling factor A is defining the amplitude. T_{off} defines the time during the signal is switched off.

A pulsed signal was specially selected because this, together with the hardware used, enabled pulse-based coherent signal processing. The two-channel approach was used to trigger the reference channel on the individually received direct signal pulses and thus determines the start of the pulse. Together with the phase coherence between transmitter and receiver, this results in a lower hardware cost compared to bistatic solutions that require a physical connection between transmitter and receiver. In addition, a cable-bound solution would disturb the flexibility during the measurements in different types of terrain.

In Figure 6.9 a sample waveform is shown, captured with the bistatic radar setup used within the scope of this thesis. The signal has been down-converted, according to the sampling in the third Nyquist band, to the frequency range from 0 MHz to 100 MHz. With the chosen bandwidth a range resolution of $1.5\,m$ can be achieved. A total of seven pulses are shown with a overall duration of $140\,\mu$s according to a signal duration during on-time of $T_{chirp} = 15\mu$s and off-time $T_{off} = 5\mu$, results in a single pulse length off $T_{chirp} + T_{off} = 20\mu$s. The pulse length was chosen to guarantee a linearly frequency sweep generated by the arbitrary waveform generator used in the transmitter. The linear time-frequency response of the transmitted and received waveform can also be seen in Figure 6.9.

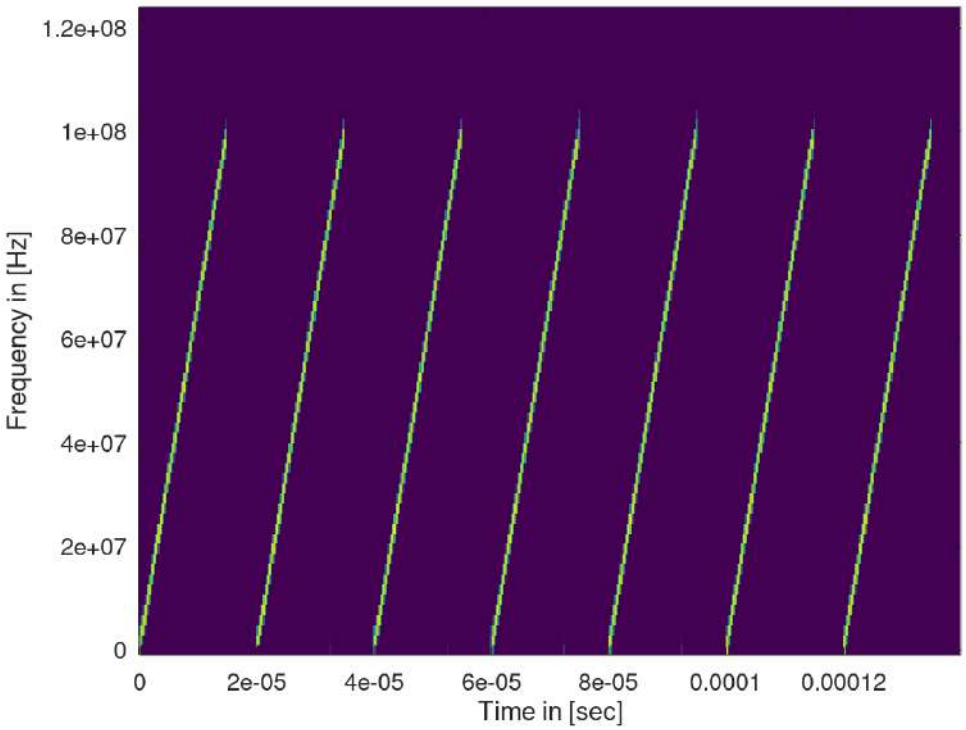

Figure 6.9: Example of a down-converted pulse train from a center frequency of 8.8 GHz to 50 MHz, containing seven transmit pulses with a bandwidth of 100 MHz and a pulse duration of 15μs.

6.2.3 The Coherent Pulse-based Signal Processing Approach

The measurement data were processed according to the coherent signal processing approach shown in Figure 6.11 to generate range-Doppler maps which served as a basis for the further statistical clutter analysis [1]. The signal processing approach in this thesis takes the two receiving channels of the chosen receiver, namely the reference channel and the surveillance channel. For radar processing it is necessary to know the start time of the received radar pulse. A hardware solution consisting of a direct connection between transmitter and receiver was out of question for cost reasons. In addition, such a design makes it difficult to install the bistatic radar in various types of terrain, some of which are impassable.

A linear frequency modulated pulse waveform was used as transmit signal which is received directly by the reference channel, directed to the side lobe of the

transmit antenna during each measurement. As the transmitted waveform is known, the beginning and the end of an incoming pulse are determined by a matched filter and a synchronization step explained in the following section. Within the scope of this thesis an improved synchronization, using a generalized cross-correlation has been developed, which was published in [3]. This approach allows an accurate determination of the pulse start time in the reference channel. An incorrect determination would otherwise lead to a range offset. As the transmitter and receiver units are externally synchronized via a 10 MHz signal, coherent signal processing is possible in this approach. This results in a higher SNR, which is advantageous for clutter analysis.

If the sample index of the pulse is known, the end of the pulse can be determined with the knowledge of the pulse width and the sampling rate. The corresponding samples of the incoming pulse are also extracted in the surveillance channel, containing the clutter echos. Clutter cancellation is performed on the surveillance signal prior to pulse extraction. This step is necessary because inherent in a bistatic radar, parts of the time-delayed transmit signal also superimpose to the surveillance signal $X_surv(t)$, reducing the dynamic range and the sensitivity of the receiver as well. This is commonly known as direct signal interference (DSI):

$$x_{surv}(t) = x_{DSI}(t) + x_{Clutter}(t) + n(t) \tag{6.3}$$

where $x_{DSI}(t)$ represents the direct signal component, $x_{Clutter}(t)$ the signal component, containing the environmental clutter and $n(t)$ the additive noise term respectively. In the above equation no target within the illuminated scene is assumed. This assumption can be assumed valid, because during the measurements only areas without further scatterers within the illuminated scene were selected. In order to perform the direct signal suppression, a recursive least squares approach has been used [84], where the template of the transmit signal pattern has been used for the cancellation. Each recursion has been performed over a block length of 1024 pulses. The extracted pulses are then Hilbert transformed. Thus, the real-valued sampled

signals are transformed to analytical, complex signals. The corresponding range profiles are calculated by cross-correlating the reference and surveillance channel pulses. A single range profile indicates the reflected energy over the bistatic range. This calculation is determined in the frequency domain using the fast convolution, which is computational more efficient compared to the time-domain convolution. The individual range profiles are stored as columns in a matrix. The number of columns is defined by the coherent processing interval (CPI). The Doppler Fast Fourier transform (FFT) is calculated along the individual rows or equivalent range bins of the matrix resulting in the final range-Doppler map. For further processing, a validation of the clutter-to-noise ratio (CNR) was performed. The CNR has been determined for each calculated range-Doppler map. Only range-Doppler matrices with a CNR higher than 25 dB were used for further processing. To determine the noise power, range-Doppler bins outside the range-Doppler area of interest were averaged according to Fig. 6.10.

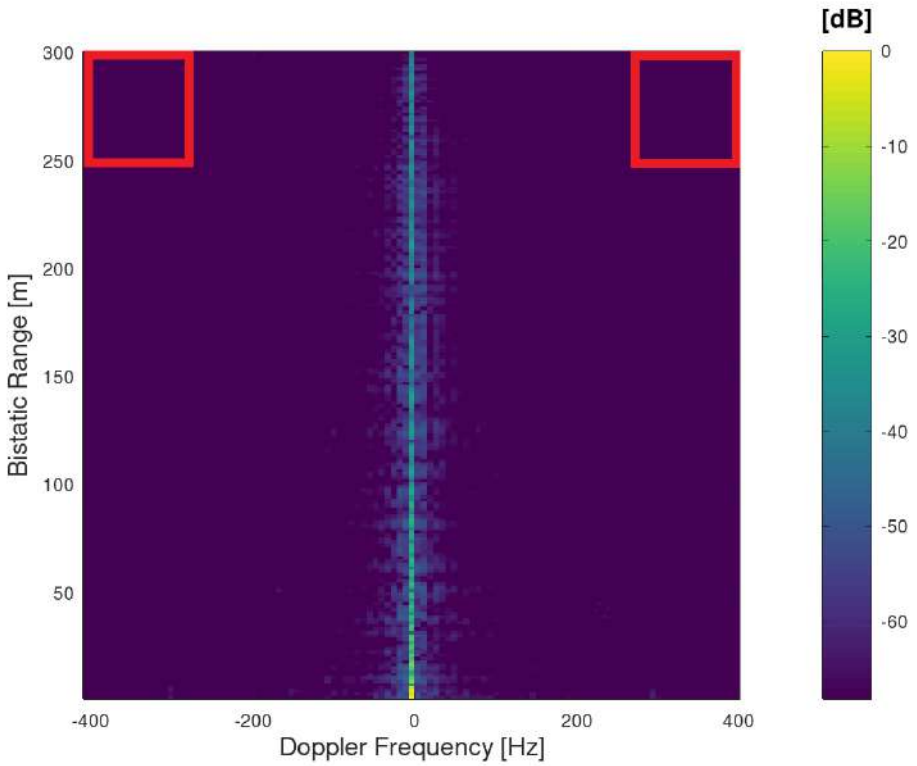

Figure 6.10: Marked region (red) of the processed range-Doppler maps in order to estimate the noise power for CNR determination. Range axis is normalized to bistatic baseline.

In order to determine the mean clutter power, the accumulated range-Doppler bins corresponding to the bistatic angle range of 60° to 80° have been used. The range-Doppler maps are then cropped in both domains to the dominant clutter area in order to perform the statistical analysis. For the measurement trials the CPI was 8192 pulses or correspondingly to 0.16384 sec. From the cropped range-Doppler region, the range-Doppler bins according to a bistatic angle range from 60° to 80° and a velocity of up to +-1$\frac{m}{s}$, accumulated over consecutive CPI's covering a total measurement time of two seconds, have been extracted for the further statistical evaluation.

This part of the page intentionally left blank.

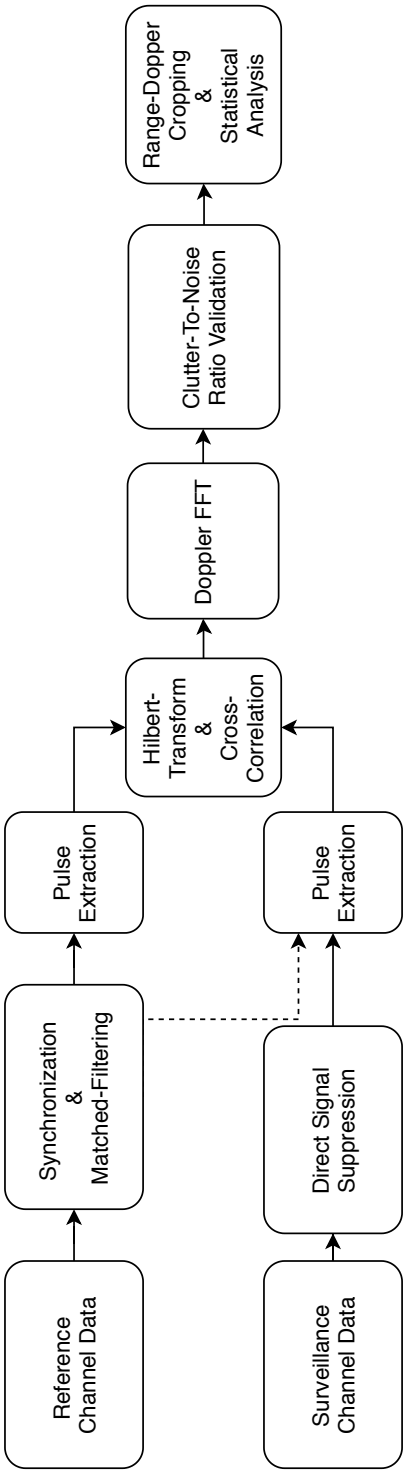

Figure 6.11: This figure shows the signal processing chain considering the two receive channels of the bistatic radar receiver. During the measurements the reference channel antenna points to the transmitter and receives the direct signal while the surveillance channel receives the clutter echoes. The statistical parameters of the clutter for the rural terrain are calculated on the processed and cropped range-Doppler maps ([1]).

6.2.3.1 An improved synchronization scheme for range-Doppler processing

In this thesis the clutter characteristics are derived from range-Doppler maps. In order to process the measurement data to create those range-Doppler maps, a synchronization to the received pulses in the reference channel is needed. So, the beginning of an incoming pulse in the reference channel can be determined. Knowing the pulse length in samples, the corresponding reference channel and surveillance channel pulses can be extracted for further processing. A common approach is to use the cross-correlation between the reference signal data with a known pattern of the transmitted signal. According to the signal-to-noise ratio (SNR) the results could be erroneous. Especially for narrow-band signals, this approach is very sensitive to low SNR levels. In the context of this thesis, an extended approach for the determination of the beginning of a pulse, received by the reference channel, was developed and published [3]. The approach relies on the generalized cross-correlation (GCC). Because the approach can be extended to any channel, in the following two sub-sections, only the received pulses in the reference channel are considered.

6.2.3.2 Generalized cross-correlation

The cross-correlation can be used to determine the beginning of a pulse in the reference channel. Therefore the received pulses $y_{rx}(t)$ are cross-correlated with the known transmit signal $x_{tx}(t)$ pattern. This is the signal which is loaded into the transmitter and radiated from there. In passive bistatic applications, this transmitter signal is often not or only partially known. In such cases, corresponding signal characteristics (e.g. guard intervals) must be available in order to continue to be able to perform an unambiguous correlation as presented here.

The beginning of the pulse can the be calculated in the first step using the cross-correlation between the received reference signal and the known transmit signal pattern:

$$r_{xy}(\tau) = \int_{-\infty}^{\infty} x_{tx}(t) y_{rx}(t-\tau) d\tau \tag{6.4}$$

where the integral limits will be chosen according to the pulse length of the signal. To ensure a complete pulse length inside the correlation window, the integration limits should be at least twice the signal duration. In the digital domain, the integral is converted into a summation, whereby the limits must be selected according to the number of samples over a length of two pulse durations. From the maximum value of the cross-correlation $r_{xy}(\tau)$, the beginning of a single pulse can be determined by the corresponding delay τ_{max}. The generalized cross-correlation uses an additional normalization kernel-function $K(f)$ to perform pre-whitening of the cross-correlation spectrum [85]. This operation is defined in the frequency domain as follows:

$$R_x y(f) = \frac{X_{tx}(f) Y_{rx}^*(f)}{K(f)} \tag{6.5}$$

where $X_{tx}(f)$ is the Fourier transform of the known transmitted signal and $Y_{rx}^*(f)$ is the conjugate-complex of the received signal Fourier transform. In [85] several kernel functions are listed. For this thesis the kernel defined in 6.6 was chosen [3], also known as Phase Transform (*PHAT*).

$$k(f) = |X_{tx}(f) Y_{rx}^*(f)| \tag{6.6}$$

which is the absolute value of the spectral cross-correlation. The correlation

spectrum is normalized to one in the amplitude by using the *PHAT*-kernel function. Since the start of the pulse must be determined in the time domain, the generalized cross-correlation in time domain is then defined as the inverse Fourier transform of 6.5 which results in:

$$r_{xy}(\tau) = \int_{-\infty}^{\infty} \frac{X_{tx}(f)Y_{rx}^{*}(f)}{|X_{tx}(f)Y_{rx}^{*}(f)|} e^{j2\pi f\tau} df \tag{6.7}$$

For the measurement data an additional spectral window $W(f)$ was applied, limiting the bandwidth to the chosen measurement bandwidth of 100 MHz. The windowing is leading to the following expression:

$$r_{xy}(\tau) = \int_{-\infty}^{\infty} W(f) \frac{X_{tx}(f)Y_{rx}^{*}(f)}{|X_{tx}(f)Y_{rx}^{*}(f)|} e^{j2\pi f\tau} df \tag{6.8}$$

with the spectral window function $W(f)$ defined as:

$$W(f) = \begin{cases} 0, & f \leq F_0 - \frac{bw}{2} \\ 1, & f_0 - \frac{bw}{2} \leq f \leq f_0 + \frac{bw}{2} \\ 0, & f \geq F_0 + \frac{bw}{2} \end{cases} \tag{6.9}$$

The rectangular spectral window results in the highest peak resolution in time domain compared to other window functions. In addition, through the filtering process the signal-to noise ratio is enhanced in case of higher sampling frequencies. Depending on the application also other window functions can be used [30], but

the choice of the window function is always a compromise between resolution and sidelobe suppression. The corresponding delay τ_d indicating the beginning of a single pulse in the received signal $y_{rx}(t)$ can then be found by solving the following problem:

$$\tau_d = \arg\max_{\tau} |r_{xy}(\tau)|, \text{ with } 0 \leq \tau \leq \tau_{max} \tag{6.10}$$

where τ_{max} is chosen to the expected maximum delay caused by the bistatic geometry.

For a pulse modulated chirp, the corresponding cross-correlation spectrum has a non-flat behaviour. With a decrease in signal-to-noise ratio, the cross-correlation spectrum becomes more noisy. The spectral non-flat cross-correlation is leading to a widening of the corresponding correlation peak in time domain of the correlation function $r_{xy}(\tau)$. The generalized cross-correlation produces a flat correlation spectrum due to normalization with the windowed *PHAT* kernel function. The kernel function behaves like a pre-whitening filter. This leads to sharper peaks of the cross-correlation function $r_{xy}(\tau)$ in time domain, with a sinc-envelope due to the applied spectral rectangular window. The *PHAT*-kernel function was chosen because of its low computational load and amplitude normalization that leads to better resolution in the time domain. The phase response, on the other hand, remains unchanged and can be used to correct the static phase shift occurring between the transmitter and receiver internal clocks [4, 30].

6.2.3.3 Time domain interpolation

The pre-whitening caused by the kernel function and the spectral window in 6.9 cause a rectangular windowing of the cross-correlation spectrum. In this case, the properties of the Fourier transform in the frequency domain result in a sinc-convolution in time domain. According to the chosen sampling frequency of the

correlation function, leakage in time domain will occur and the true maximum correlation value, indicating the beginning of a single pulse will not be sampled directly. This effect is analogous to the leakage effect in the frequency domain [86]. In Figure 6.12 the true sinc-envelope (dashed) of the cross-correlation after the inverse Fourier-Transform is drawn together with the two adjacent sample points according to the sampling frequency.

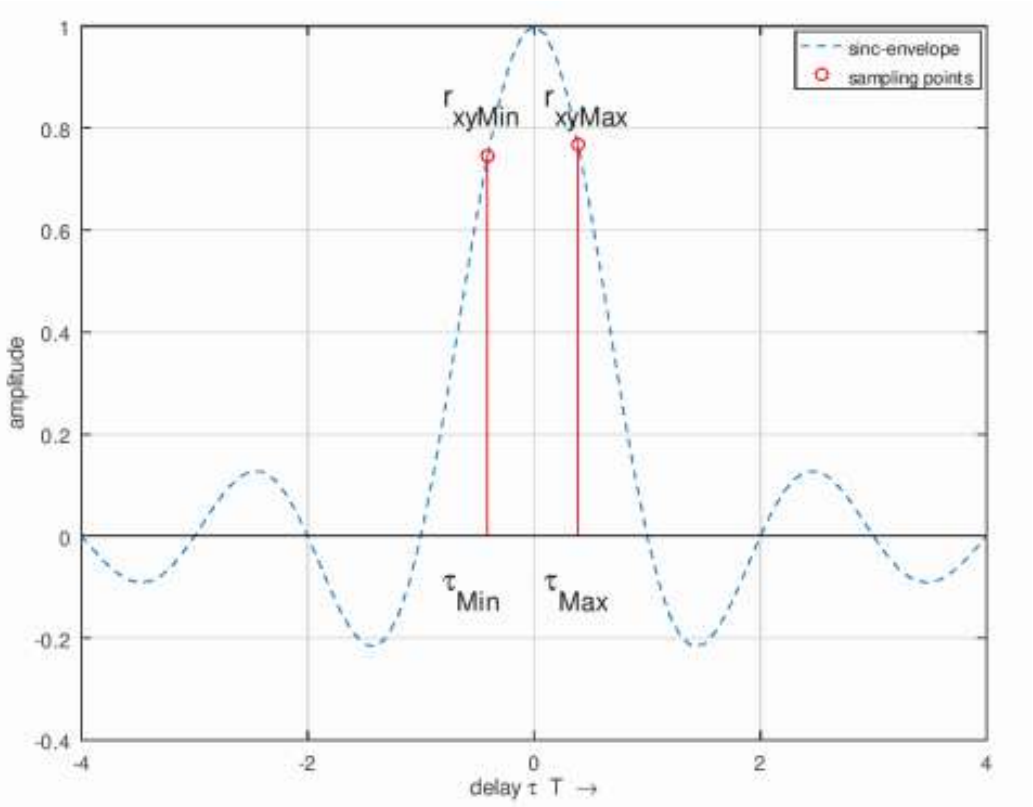

Figure 6.12: Sinc-envelope of the cross-correlation in time domain and sampling points ([3]).

As can be seen, the maximum of the sinc-envelope is not sampled, leading to leakage in time domain. The paper in [87] introduces an algorithm for an low complexity sinc-based interpolation in frequency domain. Additional information can be found in [86]. This proposed method has been applied to the time domain to improve the delay estimation with low complexity in cases where time domain leakage occurs. The proposed algorithm determines the maximum peak value r_{xyMax} at τ_{Max} according to equation 6.10 and the largest adjacent value to calculate the inter-

mediate delay value using sinc-interpolation. For the normalized cross-correlation function the sampled maximum value r_{xyMax} and its greatest adjacent sampled value $rxyMin$ are defined as follows:

$$r_{xyMax} = sinc(\tau_{err}) \tag{6.11}$$

$$r_{xyMin} = sinc(\tau_{err} - 1) \tag{6.12}$$

where τ_{err} is the delay deviation from the sample point τ_{Max} to the true value of τ_d. Computing the ratio of $rxyMax$ and $rxyMin$ is leading to the following equation:

$$\frac{r_{xyMin}}{r_{xyMax}} = sinc(\tau_{err} - 1)sinc(\tau_{err}) \tag{6.13}$$

The deviation τ_{err} from the true delay τ_d where the maximum of the sinc-envelope occurs can then be determined by solving 6.13 according to [87]:

$$\tau_{err} = \frac{r_{xyMin}}{r_{xyMin} + r_{xyMax}} \tag{6.14}$$

The time τ_{Max} where the maximum value $rxyMax$ occurred, will be corrected with the calculated delay error in equation 6.14 to increase the delay estimation accuracy. In the following section the results, demonstrating the improved robustness of the proposed approach will be presented.

6.2.3.4 Results using the improved reference signal synchronization

The proposed approach for determining the beginning of an incoming radar pulse with a known transmit signal pattern is leading to an increase in estimation accuracy. To show the increased robustness of pulse start detection, the presented synchronization method of the received pulses in the reference channel compared to the standard cross-correlation, received pulses with different delays were generated

in a Monte-Carlo simulation. The SNR was varied in each iteration. The following results have already been published in [3]. In total 1000 iterations were calculated and the results averaged. Especially under low SNR conditions the proposed method increases the estimation accuracy of the start time of the reference signal pulses, as can be seen in Figure 6.13. The estimation accuracy for the start time of the pulses can be determined by the mean square error (MSE) which is given in dB to allow a better comparison of the results between the standard cross-correlation, the generalized cross-correlation using the *PHAT* kernel function and the presented approach.

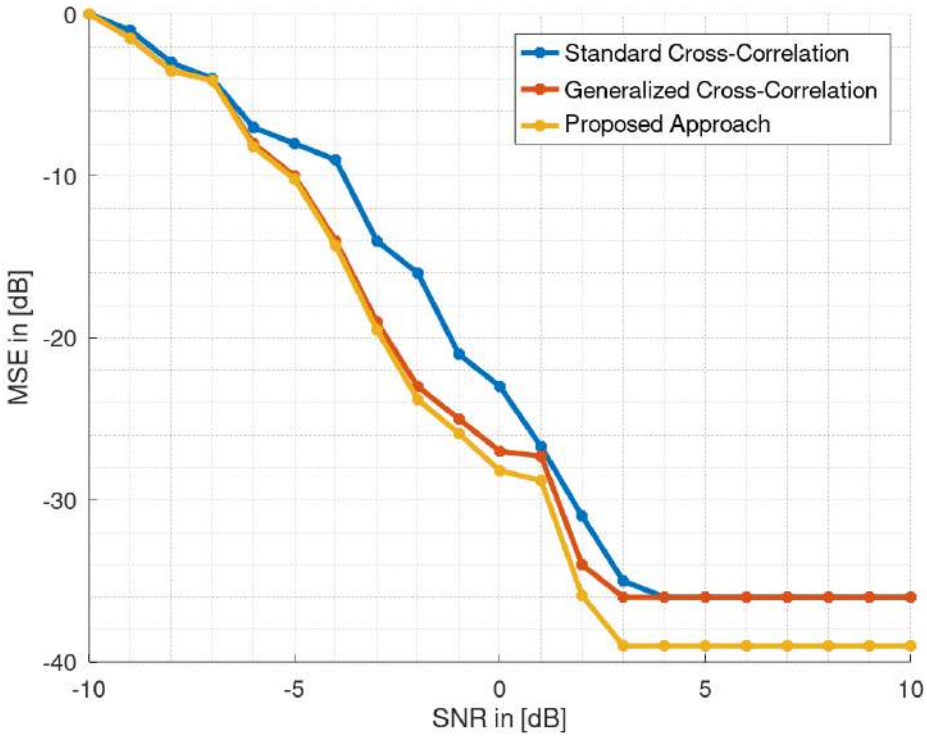

Figure 6.13: Modified cross-correlation results ([3]).

Since for the measurements made for the thesis, transmission regulations had to be considered, thus the transmission power was limited to 30 dBm. Depending on the type of terrain, the received signals are correspondingly weak. Therefore the area with envious SNR is of interest for this work. It is shown in Figure 6.14 that the presented approach results in a decreased MSE reduced by more than 3 dB

compared to the standard cross-correlation.

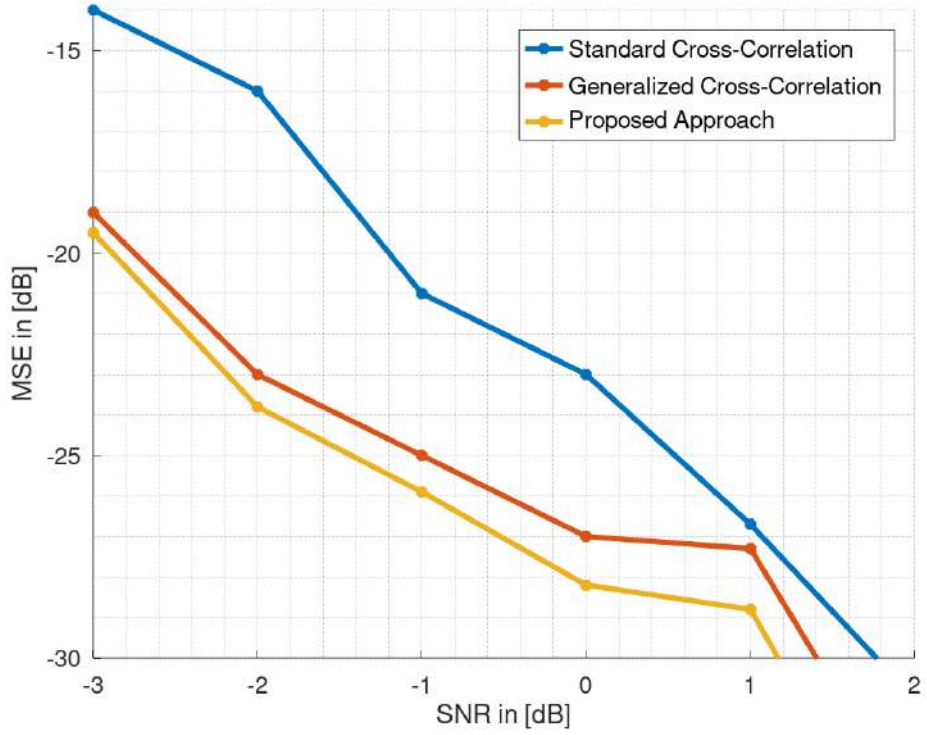

Figure 6.14: Modified cross-correlation results under low SNR conditions ([3]).

6.3 Chapter Summary

This chapter describes a novel measurement methodology in the field of rural clutter characterization for bistatic ground radar consisting of subdivision of the rural environment into four dominant subgroups of the German rural environment. A division of the rural environment into the four rural groups of fields with low vegetation, fields with high vegetation, plantations with small trees and forests is presented. The division based on the proportionate land mass of each type of terrain was verified with official data from the German Federal Statistical Office. The necessary measurement parameters were also presented, which were retained for each individual measurement in order to ensure a consistent assessment of the results obtained. The used bistatic radar setup developed by Fraunhofer FHR, consisting of a dual-channel receiver and a transmit unit has been used for the measurement trials. The bistatic nodes are synchronized externally, using Rubidium standards, generat-

ing a 10 MHz reference signal. The dual-channel approach enables a more efficient measurement process because no physical connection between the transmitter and receiver is needed. Instead, the transmitted waveform is received over-the-air by the reference signal channel. A pulse-based processing adapted to the hardware enables coherent signal processing to generate range-Doppler data for further clutter analysis. Together with the proposed pulsed radar waveform, an improved coherent signal processing approach has been presented.

6.4 Critical Discussion

This chapter describes how the clutter measurements were performed, the hardware used and how the digitized data was processed for the presentation of results. It must be kept in mind that the measurement parameters described here represent only a part of the spectrum of possible parameter variations. The holistic recording and description of the bistatic clutter in the X-band is of course not possible within the scope of a single dissertation. With the available resources, the measurement parameters described, the results presented in the following chapter can only be attributed to the selected configuration. Due to the limited memory of the oscilloscope used to digitize the data, the temporal depth of the data to be analyzed was of course also limited to a duration of two seconds. It is therefore of great interest to investigate the long-term behavior of the clutter fluctuations in range and Doppler in further studies. For further analysis, the range cells representing the bistatic angle between 60° and 80° were accumulated and the variation of the amplitude values for the measurement duration of two seconds was determined. This reduced bistatic angle range represents the relevant range under which the clutter patch was always illuminated according to the chosen measurement areas. In further investigations, a granular comparison of the amplitude variation versus the bistatic angle would be of great interest due to its great influence. The same applies to the evaluation of the clutter amplitudes within the Doppler domain. Here, the Doppler amplitudes to the corresponding range-bins have been averaged over time for each range cell. Longer integration times and a finer spectral resolution would be desirable. However, this

would also require a longer coherent data sequence, which could not be acquired with the available setup. Also an important factor for the measurement results is the clutter-to-noise ratio. Before starting each individual measurement, the terrain was first surveyed. At first, an attempt was made to create a direct signal suppression in hardware as far as possible prior to each single measurement. After warming up the equipment, test measurements were performed to ensure a clutter-to-noise ratio of at least 25 dB. This parameter also served as a threshold value in the processing. It must be noted, however, that receiver noise is probably the dominant factor here. The noise figure of 5.3 dB determined by means of a spectrum analyzer explicitly refers to the presented setup. The noise itself was estimated from the range-Doppler matrices via averaging range-Doppler bins of clutter-free area. Due to the small bistatic geometries this was not a limiting factor in terms of dynamic range. Especially for larger baselines or bistatic distances this problem becomes much more dominant. Ideally, the following results represent only the clutter statistics. However, these are always subject to noise, to some extent of course also with parts of the direct signal. For the direct signal suppression in the surveillance channel a recursive least square estimator has been applied. Because of non-linearities in the transmit and receive chain, the DSI is not only the delayed version of the transmit signal itself. It could be an interesting topic to investigate the performance using non-linear approaches for non-linear and time-variant systems. For further studies also an non-linear and also time-variant estimate of the transmit and receive transfer-functions should be investigated. Initial studies on the characterization of non-linear RF chains have been published by the author in [88] outside the scope of this thesis. However, a residual error remains in the data as a small noise component. At higher transmit powers, this problem also becomes increasingly dominant. Likewise also with weaker received signals due to larger bistatic geometries with increased free-space loss.

Chapter 7

Rural Bistatic Clutter Analysis

In this chapter the results of the evaluated measurement data are presented. First the influence of the different rural environments and the resulting clutter on the detection performance of the used bistatic radar is worked out. Then, in the following sections the different clutter characteristics of the different terrain types for different seasons are presented. Analytical model functions are also presented for the clutter amplitudes, Doppler spread and Doppler-zero line characteristics. Due to the complexity of bistatic clutter measurements and limitations of the hardware used, the presented statistics refer to those range-Doppler bins averaged over a bistatic angular range from 60° to 80°.

7.1 The Influence of the Rural Bistatic Clutter on Detection Performance

The different types of rural terrain cause different clutter characteristics. The resulting clutter influences the detection performance of the bistatic radar in different ways. To demonstrate this influence, four separated measurement campaigns were carried out in summer 2019. The goal was the detection of a small quadrocopter as shown in Figure 7.1. The X-band transmitter of the bistatic radar setup was used as co-operative illuminator during the measurement trials. The center frequency was set to 8.85 GHz. A pulse train, modulated with linear chirps and a bandwidth of 100 MHz, a pulse duration of 2 μs and a pulse repetition frequency of 50 kHz was used as transmitted waveform. The transmitted power was set to 30 dBm according to the transmission permits. During each measurement the reference antenna was steered to the transmitter sidelobes while the surveillance antenna was steered toward the terrain under test with the flying quadrocopter in it. The quadrocopter was following a cross flight-pattern shown in Figure 7.2 during the measurements, with a maximum speed of 25 $\frac{km}{h}$. The selected flight pattern ensured a maximum Doppler shift. The measured rural terrain types are a flat field, corn-field, plantation of small trees and a forest representing a typical German rural scene to investigate the detection performance under different ground clutter conditions. The small radar cross-section (RCS) of the quadrocopter represents a challenging case for the detection performance. Carbon fibre rotor blades have been mounted on the quadrocopter in order the increase the RCS. Transmitter and receiver were placed at least with a baseline of 160 meters and maximum 220 meters from each other around the terrain under test. The receive and transmit antenna field of view is around 38° and over 28° respectively. The transmit and receive antenna boresight have been aligned under a angle of 45°. The bistatic angle varied between 20° and 100°. The measurements were carried out under the same environmental conditions. Measurements were only made at wind speeds of less than 7 $\frac{km}{h}$ and in dry vegetation. The CPI corresponds to 10.000 pulses used for the generation of a single range-Doppler map. The processed range-Doppler maps were cropped to a bistatic range

of 300 meters and a maximum Doppler frequency of 400 Hz which represents the operating area of the flying quadrocopter during each measurement. The remaining parameters were the same as for the bistatic clutter measurements listed in Table 6.2. The range-Doppler plots shown in the following subsections from 7.1.1-7.1.4 have already been published in [6], where also first performance relevant effects have been discussed. The attentive reader should be informed at this point that the bistatic distances in the following range-Doppler plots are normalized. This means that all distances have been reduced by the bistatic baseline and thus start at distance zero in all plots. This serves a better comparability due to the different terrain dimensions and baselines. In the following figures, the Doppler zero line has also been removed for reasons of the dynamic range that can be displayed. The illustrations serve mainly the visual clutter representation and the detection of targets with low RCS, which is decreased by the clutter.

Figure 7.1: Quadrocopter DJI Mavic Pro with carbon fibre rotor blades to increase the RCS.

7.1.1 Detections in a field with low vegetation

As an example for a field with low vegetation, a bistatic radar measurement has been carried out on a plain salad field shown in Figure 7.3. This terrain is characterized by low vegetation. The lack of biomass leads to a strong direct signal prop-

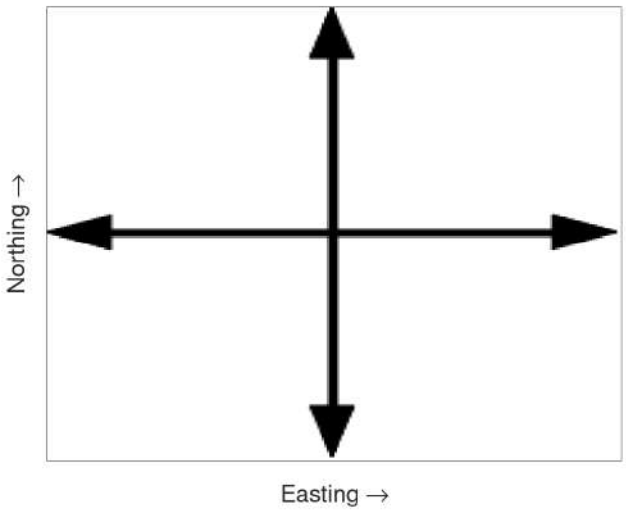

Figure 7.2: Quadrocopter cross-flight pattern ensuring maximum Doppler shift.

agation, which is only significantly influenced by free space attenuation instead of additional attenuation due to vegetation. The baseline between transmitter and receiver was 220 m. One receive antenna was steered to the transmitter sidelobe and the second receive antenna was steered to the surveillance area where the quadrocopter was flying. Due to the low vegetation, a strong direct signal component is present in the measurement data. This effect can bee seen in the detection results shown in Figure 7.4. The clutter around the Doppler-zero line has a strong extension in the bistatic range dimension with an attenuation of around 15 dB over the bistatic range of 300 m. So, the strong direct signal component, which is decades of dB higher compared to the quadrocopter echo signal, causes quadrocopter signal reflection masking, indicated by the low number of total detections in Figure 7.4. The dynamic range in such scenarios is too high for the used measurement setup due to hardware limitations of the 8 bit analog-to-digital converter. The hardware revision of the measurement setup has not a build-in automatic gain control (AGC), needed to adjust the dynamic range for the (ADC) in case of such a strong direct signal. Measurements with an updated system setup, including AGC will be part of the future work. Also indicated in Figure 7.4 is a weak Doppler spread, up to about 20 Hz. This is due to the lack of biomass which would produce clutter in case of wind movements.

Figure 7.3: A salad field as an example for a field with low vegetation.

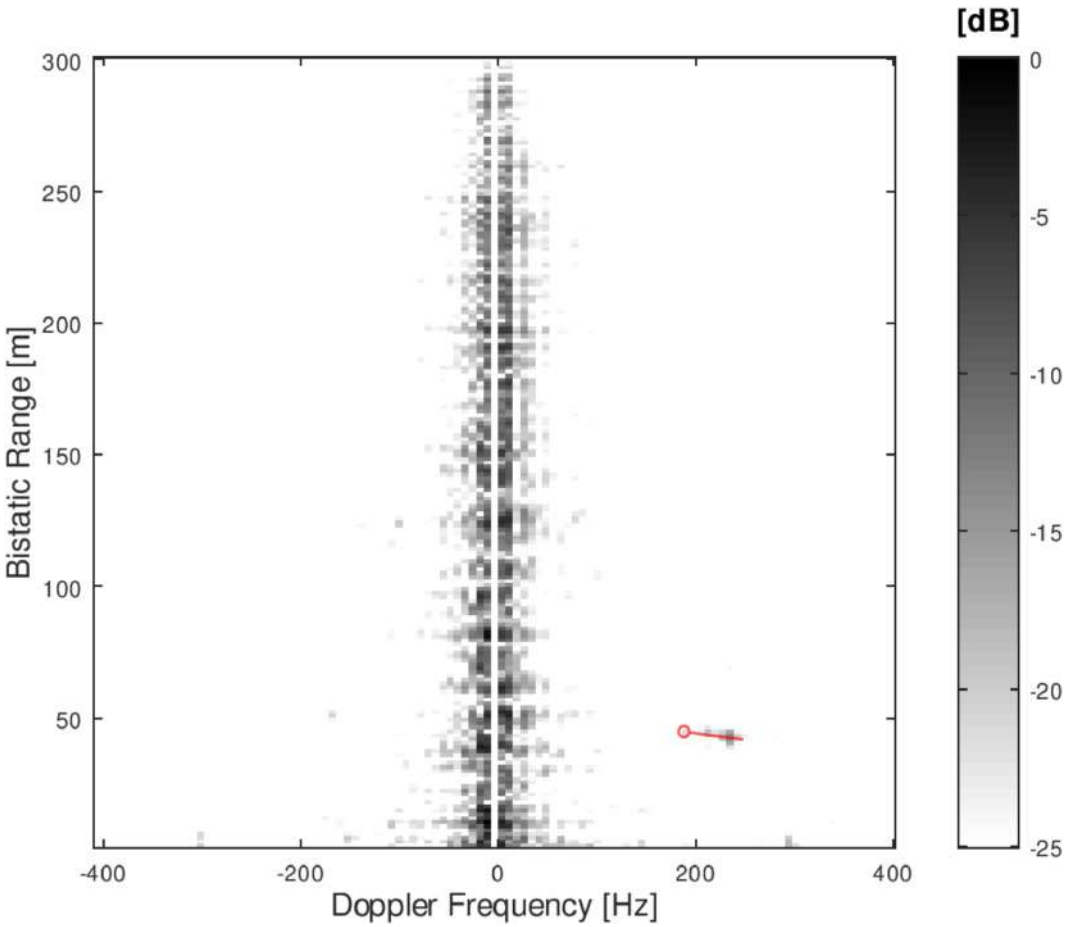

Figure 7.4: Quadrocopter detections in a field with low vegetation. Range axis is normalized to bistatic baseline.

7.1.2 Detections in a field with high vegetation

The second type of investigated rural terrain are fields with high vegetation e.g corn fields or cereal fields. This type of terrain is characterized by high vegetation. However, the biomass does not consist of wood but instead of cereals or corn plants. Therefore this type of terrain is only available in summer. These fields are harvested at the end of the summer. As an example, a corn field is shown in Figure 7.5, where the bistatic measurements have been carried out. The baseline between transmitter and receiver has been 210 m according to the terrain dimensions. The resulting detections of the quadrocopter are shown in Figure 7.6. Also the Doppler spread caused by the moving plants due to wind are visible. The Doppler-zero line shows the attenuation of the clutter over the bistatic range by about 20 dB in amplitude. Due to the highly mobile biomass, a strong Doppler spread down to about 200 Hz is also visible. The individual corn plants move even at low wind speeds. Compared to the results in the field with low vegetation, the relative number of detections is 10 times higher for fields with high vegetation. Due to the existing high vegetation, the direct signal is sufficiently attenuated and ensures a dynamic range that can be resolved by the ADC used.

Figure 7.5: A maize field as an example for a field with high vegetation.

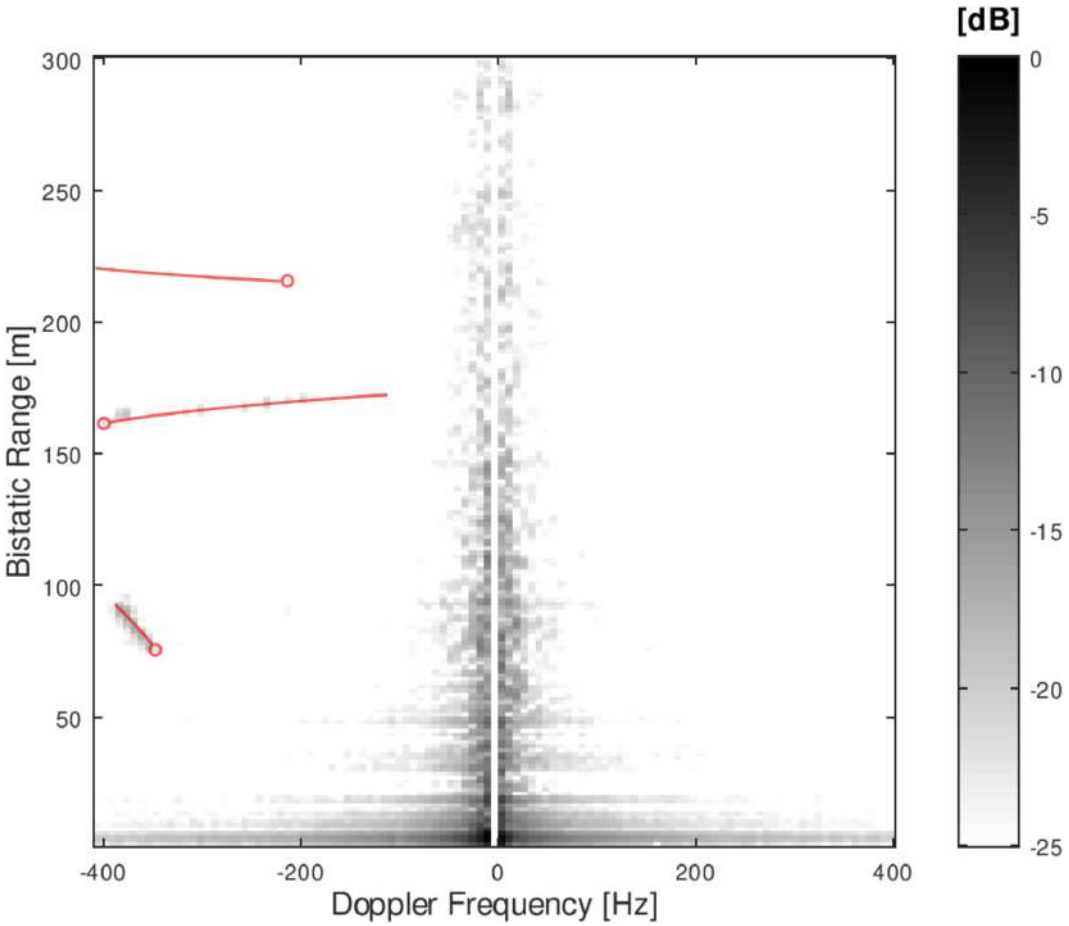

Figure 7.6: Quadrocopter detections in a field with high vegetation. Range axis is normalized to bistatic baseline.

7.1.3 Detections in a plantation of small trees

Plantations of small trees are the third group of investigated rural terrain e.g. vineyards of fruit trees. In this type of terrain the biomass consists largely of wood. The leaves of the plants are found on many small branches. For the measurements, a plantation of apple trees was chosen, which is shown in Figure 7.7. As can be seen in the Figure, the trees are arranged in rows, which is common for this type of rural terrain.

The arrangement in rows ensures that individual propagation paths are only significantly attenuated by free space attenuation and are not additionally strongly dampened by the vegetation. This may result in strong direct signal components that mask the reflected quadrocopter signal. On the other hand, the biomass, which mainly consists of wood and small thick leaves, results in strong attenuation values

Figure 7.7: A plantation of apple trees as an example for plantations of small trees.

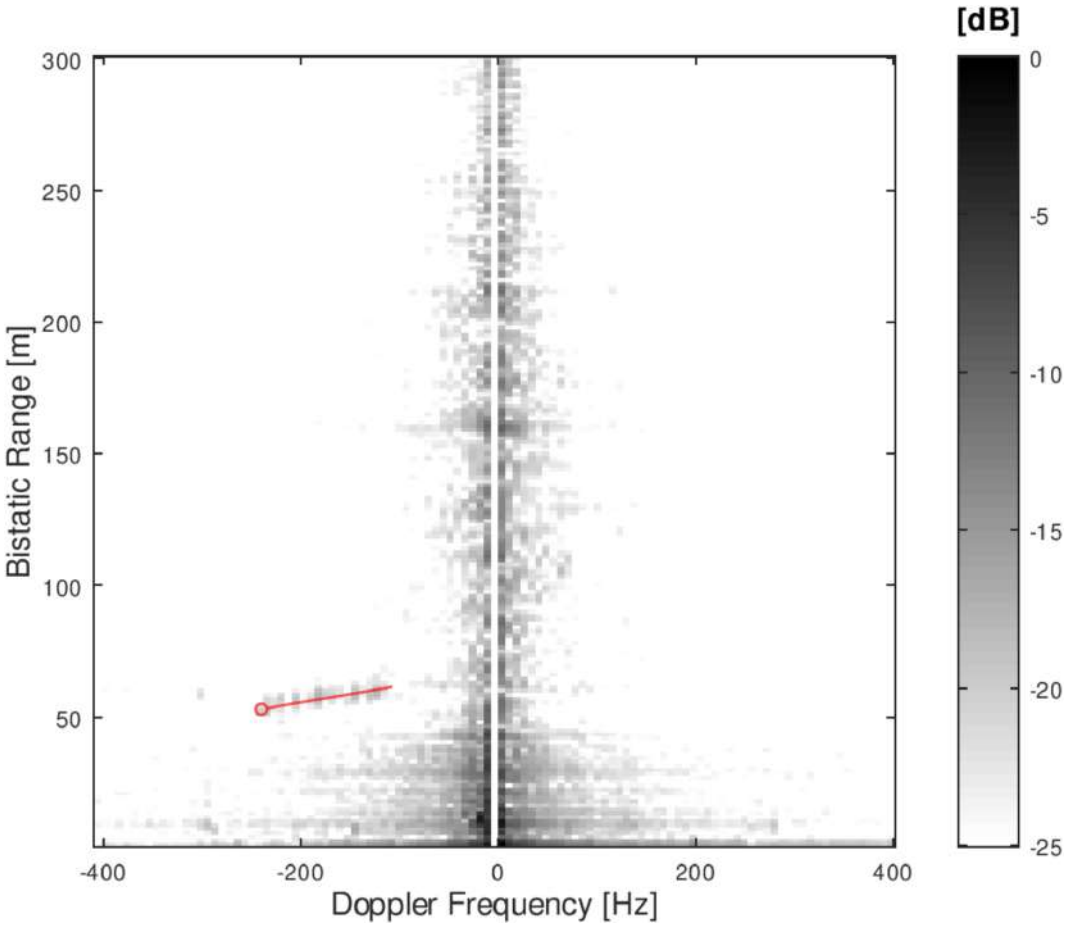

Figure 7.8: Quadrocopter detections in a plantation of small trees. Range axis is normalized to bistatic baseline.

for some propagation paths. The detection results of the quadrocopter flying the cross pattern are shown in Figure 7.8. The strong direct signal propagation due to multiple paths caused by the arrangement of the trees in rows can be recognized by the characteristic of the Doppler-zero line. The clutter is damped around 15 dB over the shown bistatic range. Due to the many small leaves and branches, which move even at low wind speeds, a clear Doppler spread of about 150 Hz is visible. The relative number of detections is two times higher compared to fields with low vegetation and about four and a half times less compared to fields with high vegetation.

7.1.4 Detections in a forest environment

The fourth dominant rural terrain group is forests. In the Eifel region in western Germany, where all measurements were carried out, these are mainly mixed forests with a high proportion of coniferous forest [89]. The forest environment where the measurements have been carried out is shown in Figure 7.9. The high proportion of wood and branches, as well as various leaves in the size range of the wavelength used lead to a strong absorption of the signals emitted and reflected by the quadrocopter. The baseline between transmitter and receiver was set to 160 m according to the terrain dimensions. The detection results of the flying quadrocopter are shown in 7.10. The strong signal attenuation caused by the forest can be seen on the Doppler-zero line. After a bistatic range of 150 m the clutter is attenuated by more than 25 dB. The relative number of detections is comparable to the fields with low vegetation, where a strong direct signal component caused object reflections masking. Whereas in the forest environment, the strong signal attenuation is responsible for the detection performance.

Figure 7.9: A mixed forest as an example for forest environments.

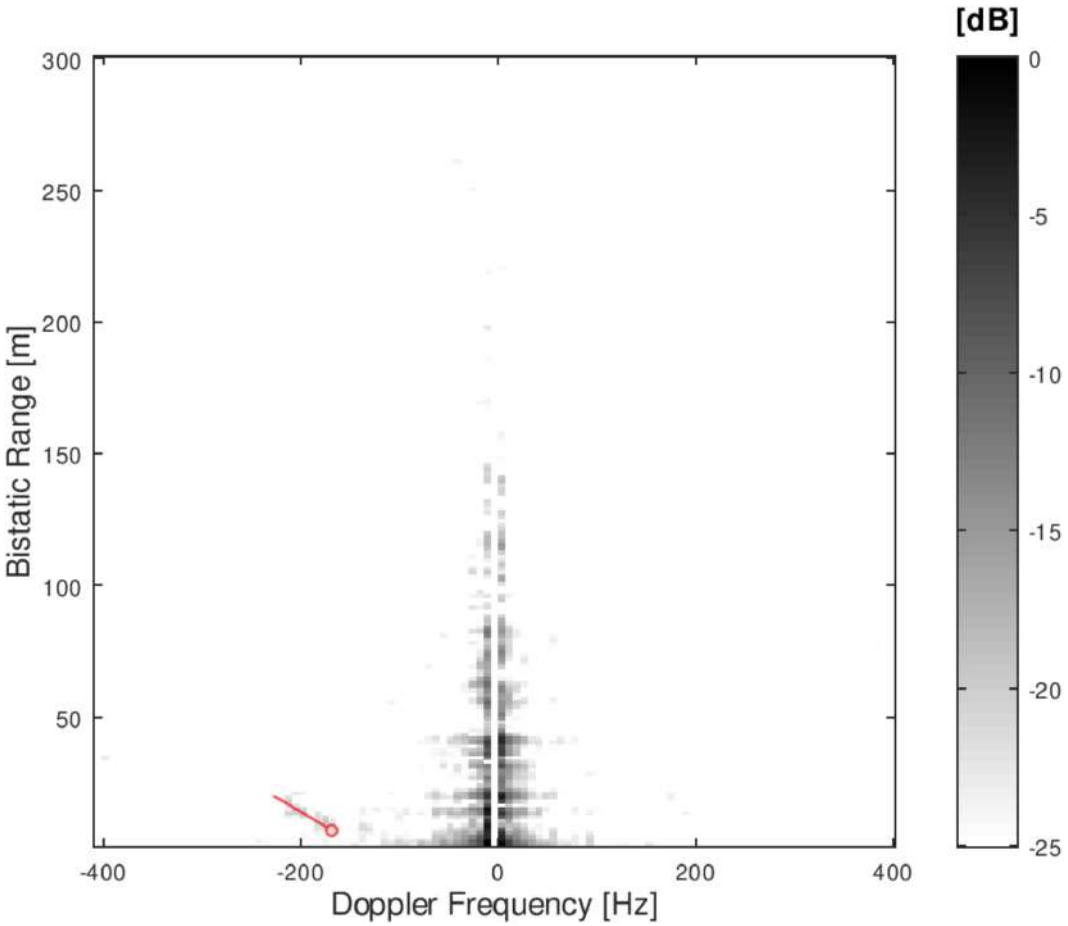

Figure 7.10: Quadrocopter detections in a forest environment. Range axis is normalized to bistatic baseline.

7.1.5 Critical discussion summary on the detection performance

As can be seen, there is a significant influence on the detection performance of the bistatic radar caused by the different resulting environmental clutter. The detection performance in the forest environment (see Fig. 7.10) and the plain field (see Fig. 7.4) is clearly reduced compared to the other terrain types. The forests cause a very weak receive signal indicated by only a small amount of detections and the reduced clutter extension in bistatic range. In the plain field the strong direct signal component causes a strong clutter spread in bistatic range covering the quadrocopter signal echos. This could be improved in future measurements with additional AGC. In the corn-fields (see Fig. 7.6) the good propagation conditions and the direct signal suppression due to the vegetation are causing multiple quadrocopter detections. The movements of the corn plants are causing a dominant Doppler spread of around 200 Hz. An increase in transmitted power could lead to a further improvement in the detection rate. For the plantations of small trees a(see Fig. 7.8) the biomass, mainly consisting of wood and small branches with leafes, a significant signal attenuation is causing detection masking. Due to the arrangement of the trees in rows, several propagation paths are mainly not influenced by vegetation attenuation rather than free space loss. This is also causing a strong direct signal component, indicated by the clutter attenuation of around 15 dB over a bistatic range of 300 m. The relative number of detection in fields with high vegetation is almost ten times higher compared to fields with low vegetation and forest environments and even four and a half times higher compared to plantations of small trees. The results show that the different types of rural terrain have an significant influence on the detection performance of the used bistatic radar setup.

7.2 Rural Bistatic Clutter Statistics

In this section the bistatic clutter analysis of the different rural terrains are presented. A further subdivision of the results for summer and winter is also part of this section. The data basis for the evaluation is the range-Doppler data processed according to the procedure described above. These were reduced to the relevant clutter areas and evaluated for the averaged range-Doppler bins corresponding to a bistatic angle range from 60° to 80°. The corresponding cells for the specific terrain types and seasons have been averaged over all taken measurement trials, in order to present a more robust analysis.

Parts of the following results have already been published in [1, 5]. This concerns especially the histogram and CDF results in 7.2.1 and 7.2.2, as well as the correlation analysis in table 7.1. In [1] also first results of the descriptive statistics of table 7.2 were presented.

7.2.1 Clutter Amplitude Histogram Figures and Correlation Analysis

Figure 7.11 shows the histogram figures of the four terrain groups for the measurements carried out in the summer. The histograms are normalized to their mean values for better comparability. Otherwise the different damping factors resulting from different terrain dimensions would lead to an incorrect representation of the results. Then a cumulative sum over the bins results in the CDF. The histogram bin-range is limited to -30 dB up to 30 dB for the visualization.

It can be seen that the histogram figures show a shifted probability density function for the fields with low vegetation to the right of the mean value. For the fields with high vegetation, plantation of small trees and forests, the probability density functions are shifted to the left. It can also be seen that the PDF appearance and width are clearly different for each terrain.

Figure 7.12 shows the histogram figures for the measurements carried out in the winter. For the fields with high vegetation, no measurements have been made

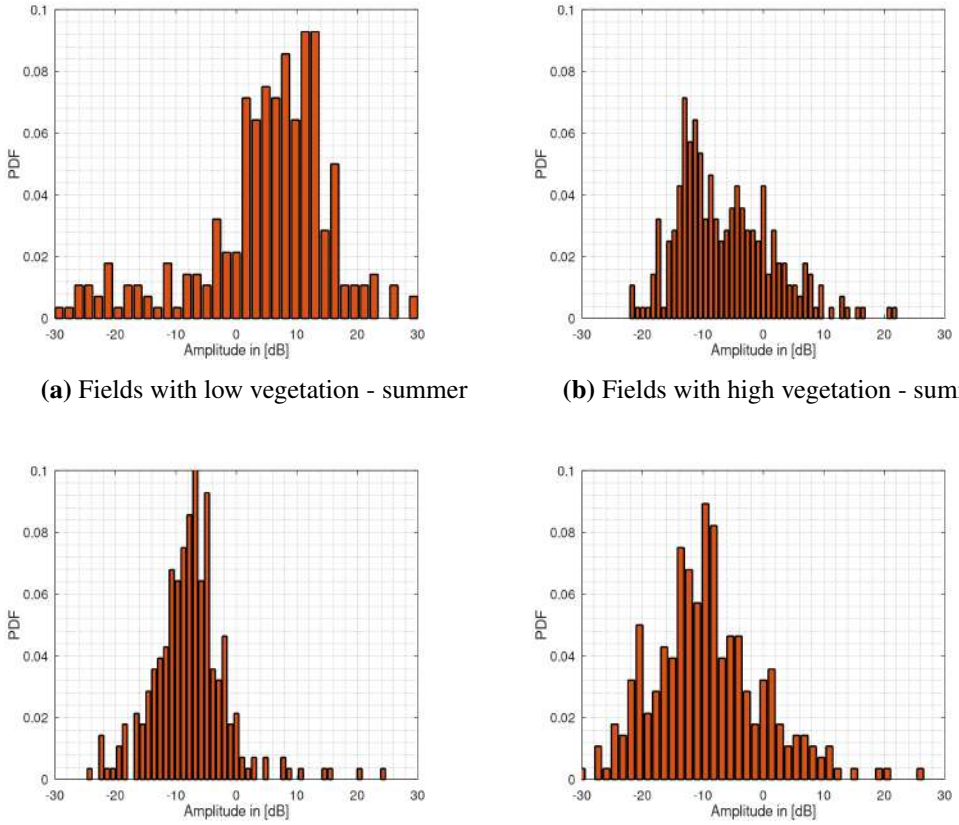

(a) Fields with low vegetation - summer

(b) Fields with high vegetation - summer

(c) Plantations of small trees - summer

(d) Forest environments - summer

Figure 7.11: Histogram figures of the clutter amplitudes for the summer measurements for (a) fields with low vegetation, (b) fields with high vegetation, (c) plantations of small tress and (d) forest environments (published in [1]).

because during this season the terrain falls into the group of fields with low vegetation. It can also be seen in the data of the winter measurements that the probability density function, approximated by the histogram values, for fields with low vegetation shows a shift to the right, whereas the other terrain groups show a shift to the left. This is the same behaviour as for the measurements carried out during the summer. In general, the histograms for all terrain types show a flattened course for the winter measurements than the corresponding histograms for the summer measurements. The flattening of the histograms could be an indication of an increase in the clutter amplitude spread due to reduced vegetation at this time of year.

A correlation analysis has been applied to the calculated histogram data. This allows the linear correlation between the individual types of terrain to be shown. Furthermore, the correlation between the respective types of terrain and seasons can be

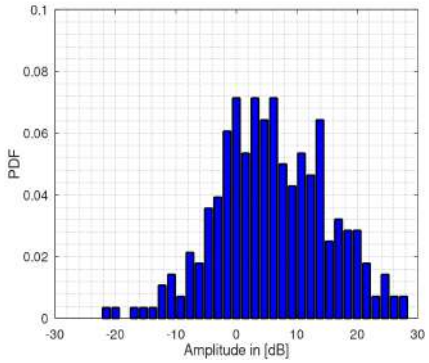

(a) Fields with low vegetation - winter

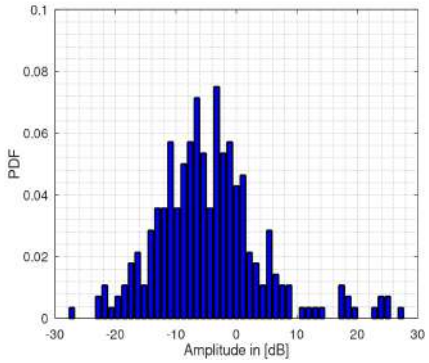

(b) Plantations of small trees - winter

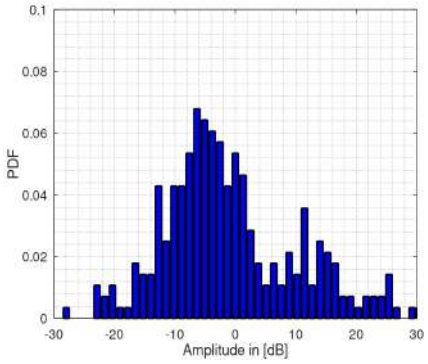

(c) Forest environments - winter

Figure 7.12: Histogram figures of the clutter amplitudes for the winter measurements for (a) fields with low vegetation, (b) plantations of small tress and (c) forest environments (published in [1]).

quantified. The corresponding Pearson correlation coefficients are listed in Table 7.1. As can be seen the fields with low vegetation for summer and winter correlate with a value of 0.78. Also, the histogram appearance for the plantations of small trees shows a strong correlation between summer and winter with a value of 0.76. The forest environment in summer correlates with the forest environment in winter with a value of 0.64 and a value of 0.84 with the plantations of small trees during winter. A possible explanation could be the fact that both types of terrain consist mainly of trees. At this point, attention should be drawn once again to the idea of correlation analysis for the classification of the clutter environment. This could be an interesting application in adaptive radar applications. The unique correlation properties can be used to classify the rural terrain and thus provide a-priori knowledge for adapting the radar application to the corresponding rural environment.

Terrain Under Test	Fields with Low Vegetation Winter	Plantations of Small Trees Winter	Forest Environment Winter
Fields with low vegetation summer	0.78	0.1	0.18
Plantations of small trees summer	−0.16	0.76	0.59
Forest environment summer	−0.04	0.84	0.64

Table 7.1: Pearson correlation coefficients for the different clutter histograms of the fields with low vegetation, plantations of small trees and forest environments and the corresponding winter histograms ([1])

.

7.2.2 Clutter Amplitude Cumulative Distribution Figures

The cumulative distribution figures for the clutter amplitudes were calculated from the corresponding histogram values by cumulative summing up the histogram bins ([1]). The results are shown in Figure 7.13 for the various rural terrain types for summer measurements. For the winter measurements, the resulting cumulative distributions are shown in Figure 7.14. For the fields with low vegetation, only summer measurements are available in Figure 7.13b. As this type of terrain is only available during the summer, no measurement data were recorded. Instead, the empty fields then fall into the category of fields with low vegetation in winter. The cumulative distribution figure visualizes the density of the relative damping values. As expected, these are highest for forest environments, see Figure 7.13d, and lowest for fields with low vegetation in Figure 7.14a.

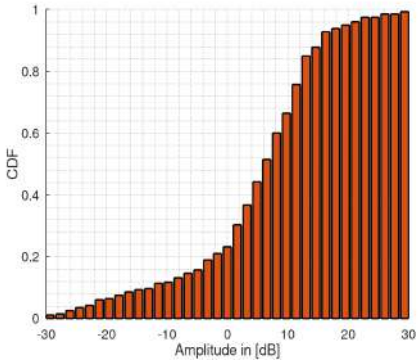

(a) Fields with low vegetation

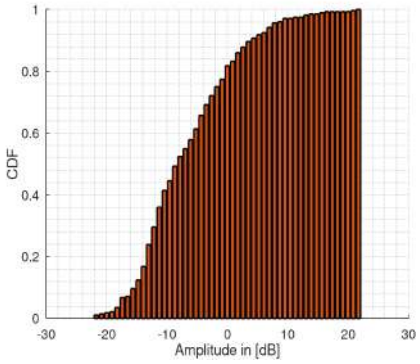

(b) Fields with high vegetation

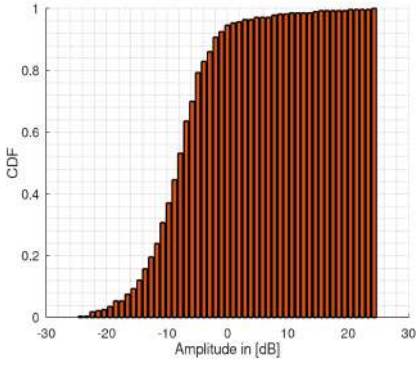

(c) Plantations of small trees

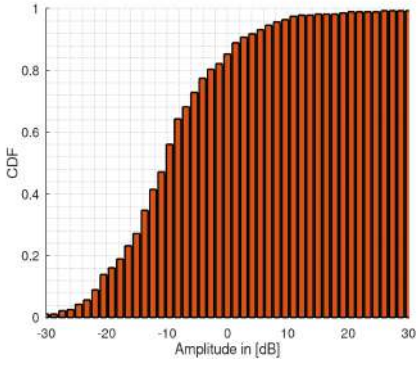

(d) Forest environments

Figure 7.13: Cumulative distribution figures of the clutter amplitudes for summer measurement data ([1]), for (a) fields with low vegetation, (b) fields with high vegetation, (c) plantations of small tress and (d) forest environments.

During the transition from summer to winter, the density functions especially for plantations of small trees in Figure 7.14b and forest environments in Figure 7.14c, move farther to the right. The steepest increase in slope of the cumulative distribution results for the terrain group of the plantations of small trees. This can also be seen from the corresponding histogram, as the amplitude values are centered around the mean value. It can be seen that the flatter the cumulative distribution, the larger the clutter amplitude spread.

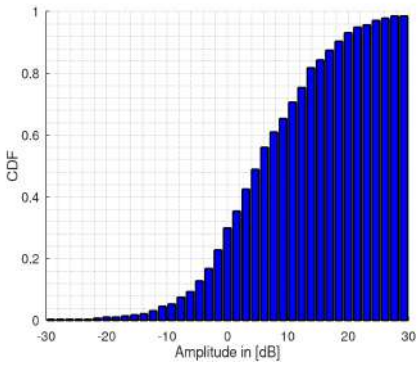

(a) Fields with low vegetation - winter

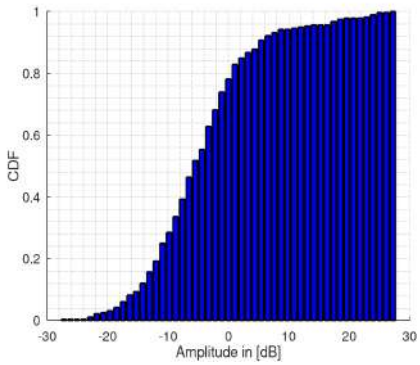

(b) Plantations of small trees - winter

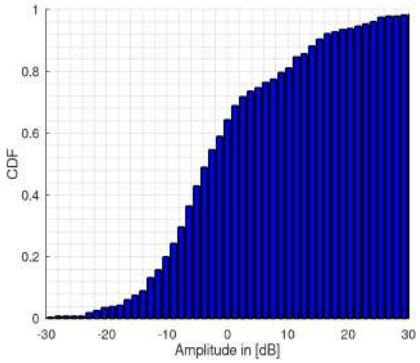

(c) Forest environments - winter

Figure 7.14: Cumulative distribution figures of the clutter amplitudes for winter measurement data ([1]), for (a) fields with low vegetation, (b) plantations of small tress and (c) forest environments.

The offset, defined as cumulative distribution shift between the forest data in summer and winter is significantly greater at about 8 dB compared to plantations of small trees with about 3 dB. For fields with low vegetation this offset is negligible. According to their cumulative distribution, these have similar statistics in

both seasons. It can be further noted that the slope of the cumulative distribution is higher for the plantations than for the other types of terrain. This behaviour is also confirmed in the data from the winter measurements.

7.2.3 Descriptive Clutter Statistics

Table 7.2 shows the characteristics of the descriptive statistics for the measured bistatic ground clutter from the average cropped range-Doppler regions. Here, fields with low vegetation show the largest standard deviation with nearly 12 dB. The lowest standard deviation was measured for terrains with plantations of small trees. In contrast, the data for the winter measurements give the largest IQR with about 14 dB for forest environments. As already seen in the histogram figures, the data for the fields with low vegetation were negatively skewed for both summer and winter. The highest value for the kurtosis was calculated from the measured data for the plantations of small trees during summer. The following table has already been published in [1].

Terrain Under Test	σ	**IQR**	**Skewness**	**Kurtosis**
Fields with low vegetaion - summer	11.8 dB	10.8 dB	-0.98	1.7
Fields with high vegetation - summer	7.9 dB	11.2 dB	0.73	0.5
Plantations of small trees - summer	6.2 dB	6.2 dB	0.98	4.4
Forest environment - summer	10.0 dB	10.9 dB	0.88	2.3
Fields with low vegetation - winter	10.1 dB	13.1 dB	-0.11	1.3
Plantations of small trees - winter	9.0 dB	10.0 dB	0.84	1.64
Forest environment - winter	11.7 dB	14.3 dB	0.62	0.33

Table 7.2: Descriptive statistical properties of the clutter amplitudes for the different terrain types during summer and winter from the cropped and averaged clutter patches ([1]).

A box-plot analysis has then been performed to visualize the minimum, maximum, median and percentiles (1st, 2nd, 3rd) values. Each plot in Figure 7.15 -7.18 shows the corresponding box-plot for the summer vegetation on the left and the winter vegetation on the right. The group of fields with high vegetation during summer is plotted against the fields with low vegetation during winter. Corn or cereal fields are not present during the winter season. In Figure 7.15, the box-plots for fields with low vegetation show that the properties do not change significantly between summer and winter. This could be due to the similar vegetation in both seasons. The IQR in winter is increased by 2.3 dB compared to summer. From the box-plot for the summer measurements, clear outliers can be seen in the clutter amplitudes. This could be due to multipath propagation caused by vegetation moving in the wind. Due to the strong direct signal components, a faulty analysis cannot be excluded. The box-plot for fields with high vegetation indicates the lowest number of outliers in the summer measurement data (see Figure 7.16).

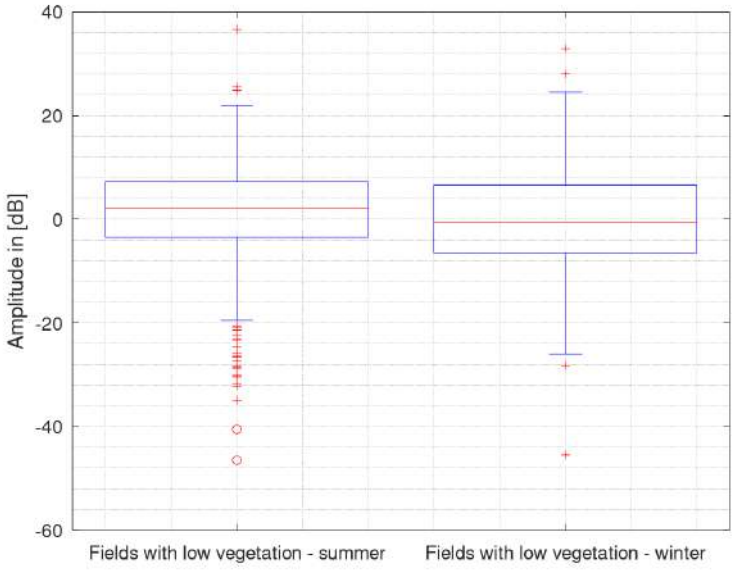

Figure 7.15: Box-plot of clutter amplitudes for fields with low vegetation during summer and winter.

A significant increase in the dynamic range is visible for plantations of small trees in Figure 7.17. However, the number of outliers behaves similarly in the sum-

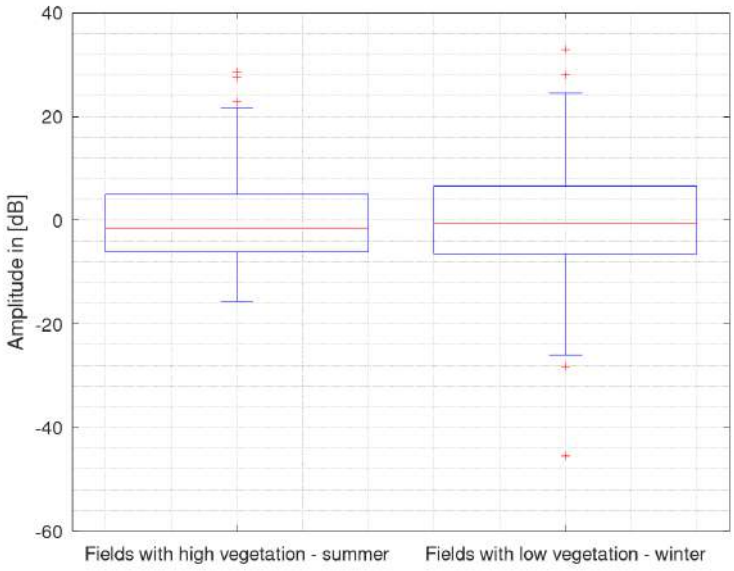

Figure 7.16: Box-plot of clutter amplitude for fields with high vegetation during summer and and comparable fields with low vegetation during winter. Fields with low vegetation are not present during the winter season.

mer and winter measurement data. A similar behaviour can be observed for forest environments, shown in the box-plot in Figure 7.18. As both rural terrain types consist mainly of trees, this could be a possible explanation.

The corresponding statistical parameters represented by the box-plots are listed for the different terrain types and seasons in Table A.1 in the appendix section. It can be seen that especially fields with low vegetation show the smallest clutter amplitudes. The maximum values occur in forest environments during summer measurements. Plantations of small trees, both in summer and winter, show similar minimum and maximum values.

Fields with high vegetation have a limited amplitude range from -15.6 dB to 28.6 dB. This is the smallest value range among the terrain types considered.

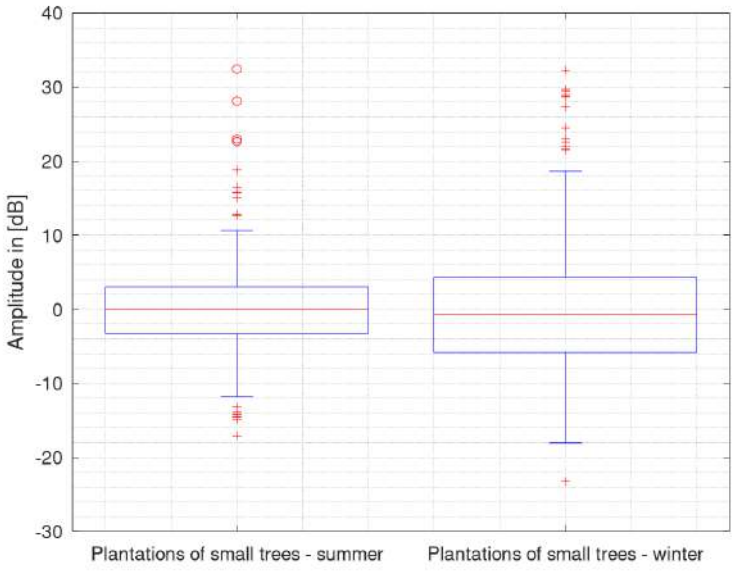

Figure 7.17: Box-plot of clutter amplitudes for plantations of small trees during summer and winter.

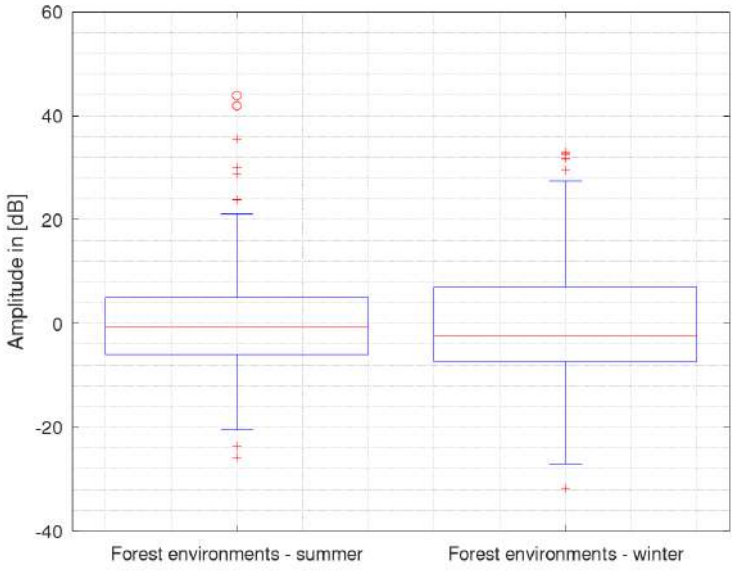

Figure 7.18: Box-plot of clutter amplitudes for forest environments during summer and winter.

7.2.4 Clutter Amplitude Probability Density Functions

In order to analytically describe the bistatic clutter amplitude probability density functions, Weibull density functions have been fitted to each histogram data-set.

The following table shows the quality of the Weibull fit compared to the Rayleigh distribution using the log-likelihood as goodness-of-fit quantity. The higher log-likelihood values imply the choice of the Weibull distribution.

Terrain Under Test	Weibull	Rayleigh
Fields with low vegetation - summer	704.296	183.442
Fields with low vegetation - winter	497.273	185.538
Fields with high vegetation - summer	652.927	260.156
Plantations of small trees - summer	909.621	107.538
Plantations of small trees - winter	572.214	35.667
Forest environment - summer	541.368	132.046
Forest environment - winter	597.976	171.105

Table 7.3: Log likelihoods for Weibull and Rayleigh distribution fits to the clutter statistics.

Using maximum-likelihood estimation, the necessary scale and shape parameters, λ and k describing the Weibull probability density function, have been estimated. Prior to the parameter estimation, all histogram values were shifted into the positive value range, since the Weibull distribution is not defined for negative values. The corresponding offset is listed in Table 7.4. Together with the other values in the presented table, the two-parameter Weibull distribution is fully described. The analytically described clutter distributions are shown for the different terrain types and the corresponding seasons in Figure 7.19.

Figure 7.19a shows even more clearly in comparison to the histogram figures that especially for fields with low vegetation the density functions between summer and winter show no significant difference. This could be due to the terrain conditions. During summer, as well as winter, there is only little vegetation available, which could lead to dominant back-scattering. The density function for this type of terrain shows a skewness to the right in both summer and winter measurement

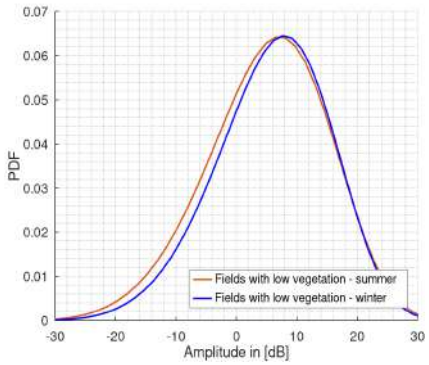

(a) Fields with low vegetation - summer

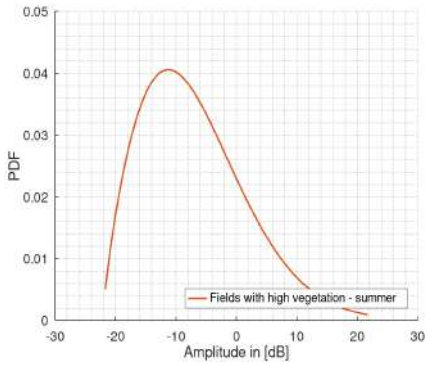

(b) Fields with high vegetation - summer

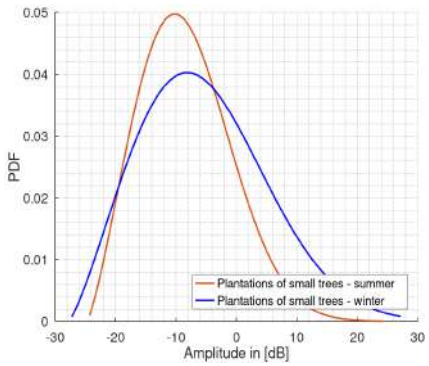

(c) Plantations of small trees - summer

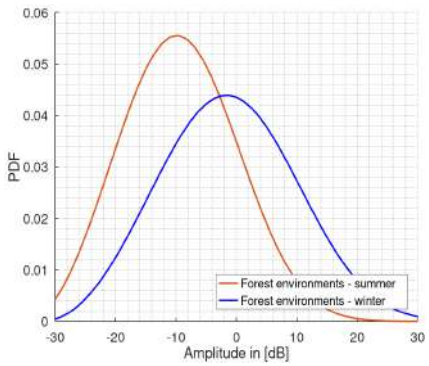

(d) Forest environments - summer

Figure 7.19: Modelled bistatic clutter amplitude probability density functions for (a) fields with low vegetation, (b) fields with high vegetation, (c) plantations of small tress and (d) forest environments in summer and winter.

data. Whereas all other density functions show a skewed distribution to the left side. Differences between the summer and winter clutter properties are particularly noticeable in small tree plantations and forest environments, shown in Figure 7.19c and 7.19d. Both types of terrain have a broader and flattened density function in the winter measurement data compared to the summer measurement data. This may be due to the lack of leaves at this time of year. In general, similar function curves can be recognized for both types of terrain. Plantations of small trees as well as forest environments both consist mainly of trees which could be a reason for this.

Terrain Under Test	λ	k	Offset
Fields with low vegetation - summer	50.623	5.332	-41.897
Fields with low vegetation - winter	48.894	5.483	-39.807
Fields with high vegetation - summer	17.191	1.787	-11.681
Plantations of small trees - summer	18.561	2.318	-15.940
Plantations of small trees - winter	25.355	2.268	-20.455
Forest environment - summer	28.669	2.972	-17.271
Forest environment - winter	34.9521	3.093	-23.701

Table 7.4: Estimated scale, shape and offset parameters, describing the Weibull fit for the different rural terrain types in winter and summer vegetation.

7.2.5 Clutter Amplitude Cumulative Distribution Functions

From the scale and shape parameters for the clutter density functions determined by the maximum-likelihood estimation, the corresponding cumulative distribution functions can also be described analytically. The corresponding clutter Weibull distributions are shown for the different terrain types and seasons in Figure 7.20. Figure 7.20a again shows the similarity of distributions for fields with low vegetation in both summer and winter. According to Figure 7.20b, fields with high vegetation have the steepest distribution. This type of terrain is not present in winter and therefore no measurements have been carried out. Differences between the clutter statistics between summer and winter are mainly visible for plantations of small trees and forest environments. In Figure 7.20c, a shift to the right of the winter distribution is visible compared to summer. The same effect can be observed in forest environments in Figure 7.20d. Again, the composition of the terrain types, mostly trees, may be an explanation in this behavior.

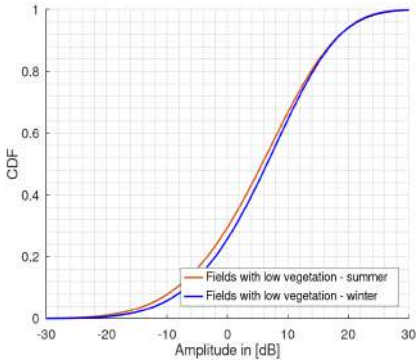

(a) Fields with low vegetation - summer

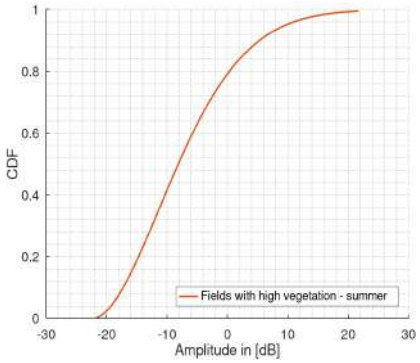

(b) Fields with high vegetation - summer

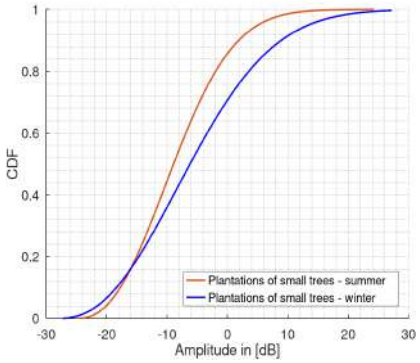

(c) Plantations of small trees - summer

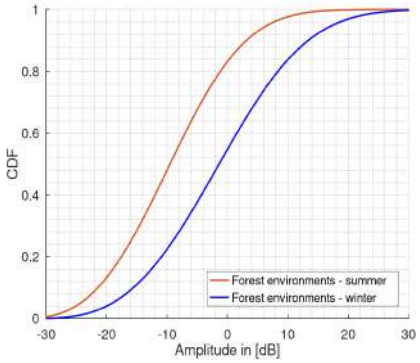

(d) Forest environments - summer

Figure 7.20: Modelled bistatic clutter amplitude cumulative distribution functions for (a) fields with low vegetation, (b) fields with high vegetation, (c) plantations of small tress and (d) forest environments in summer and winter.

7.2.6 Clutter Doppler Domain Characteristics

In this section the Doppler spread characteristics will be presented. The Doppler spread occurs by moving clutter scatterers e.g. moving vegetation due to wind. During each bistatic clutter measurement, the wind-speed has been below 7 $\frac{km}{h}$, in order to make the results comparable. To extract the Doppler spread, the maximum value of each column from the processed and cropped range-Doppler maps has been determined over the bistatic range of 500 m, the relevant range the used hardware setup was able to detect clutter echos. In Doppler dimension, the Doppler bins within the range from -3 $\frac{m}{s}$ to +3 $\frac{m}{s}$ have been evaluated, covering the range of expected velocities. The Doppler spread spectra for the four rural terrain types and the corresponding seasons are presented in Figure 7.21.

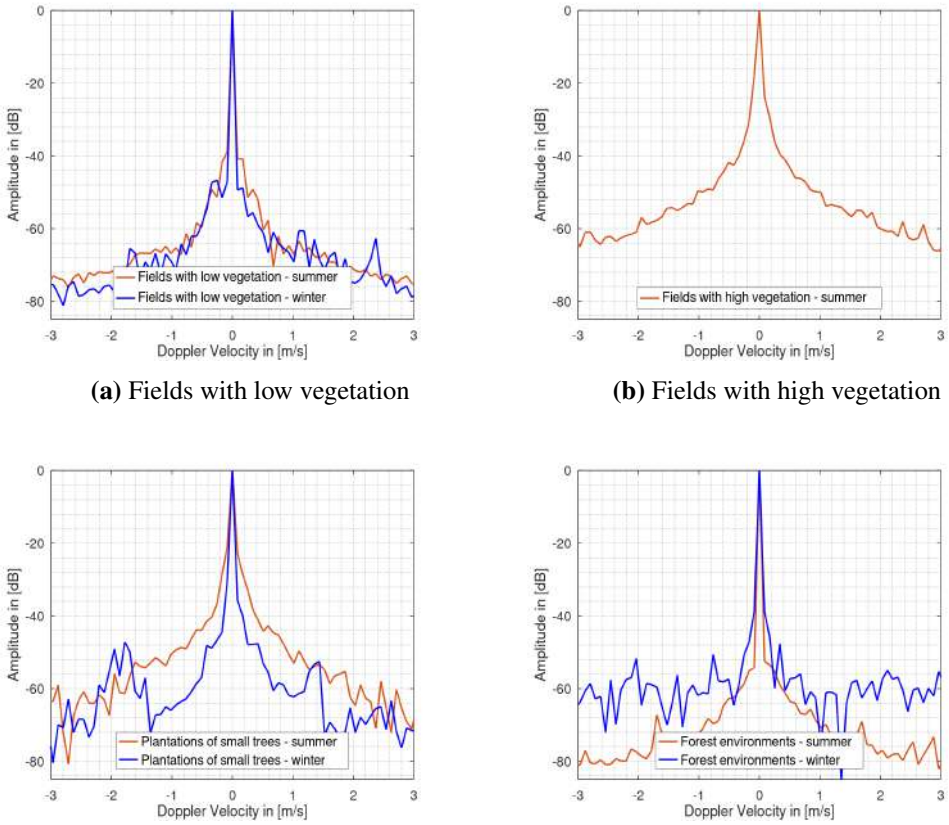

(a) Fields with low vegetation

(b) Fields with high vegetation

(c) Plantations of small trees

(d) Forest environments

Figure 7.21: Doppler spread spectra for (a) fields with low vegetation, (b) fields with high vegetation, (c) plantations of small tress and (d) forest environments in summer and winter.

The Doppler spread characteristic for fields with low vegetation behaves similarly in summer and winter, as shown in Figure 7.21a. This type of terrain, due to its low vegetation during both, summer and winter season, has little to no biomass that could produce strong Doppler modulated reflections. Therefore, the Doppler spectrum decreases relatively quickly compared to fields with high vegetation. Due to their highly mobile vegetation, these fields produce distinct Doppler reflections (see Figure 7.21b). However, this type of terrain is only found in summer, so no winter measurements are available. Figure 7.21c shows the corresponding Doppler spectra for plantations of small trees. Compared to the measurement data during summer, a decrease of the Doppler spread amplitude in winter can be seen. This could be due to the fact, that this type of terrain has a reduced biomass in winter compared to summer. The strong Doppler spread in summer could be due to the strong vegetation consisting of many small leaves and branches. Especially the many small branches provide a strong Doppler spread due to their movement in winter as well. A slightly different behaviour can be seen for forests in Figure 7.21d. In the data from the summer measurements, only a small Doppler spread is visible. This could be due to the strong signal attenuation of this type of terrain. In the winter season a stronger Doppler spread is visible. A possible explanation would be the fact that the lower attenuation in this season allows stronger reflections. Since the measured forest areas are mixed forests, there is also biomass available in winter (ever-green), which produces strong Doppler amplitudes due to movement in the wind.

As can be seen in Figure 7.21, the Doppler spread spectra can be assumed symmetrically. For the further investigations, therefore, only the single-sided spectra will be considered. In Figure 7.22 the single-sided Doppler spectra and the corresponding sampling points are shown. The single-sided spectra are the data bases for the following modelling of the Doppler characteristics. The single sided Doppler spectra are limited to a maximum velocity of $1\ \frac{m}{s}$, which is the interesting velocity range for the following dominant Doppler component analysis.

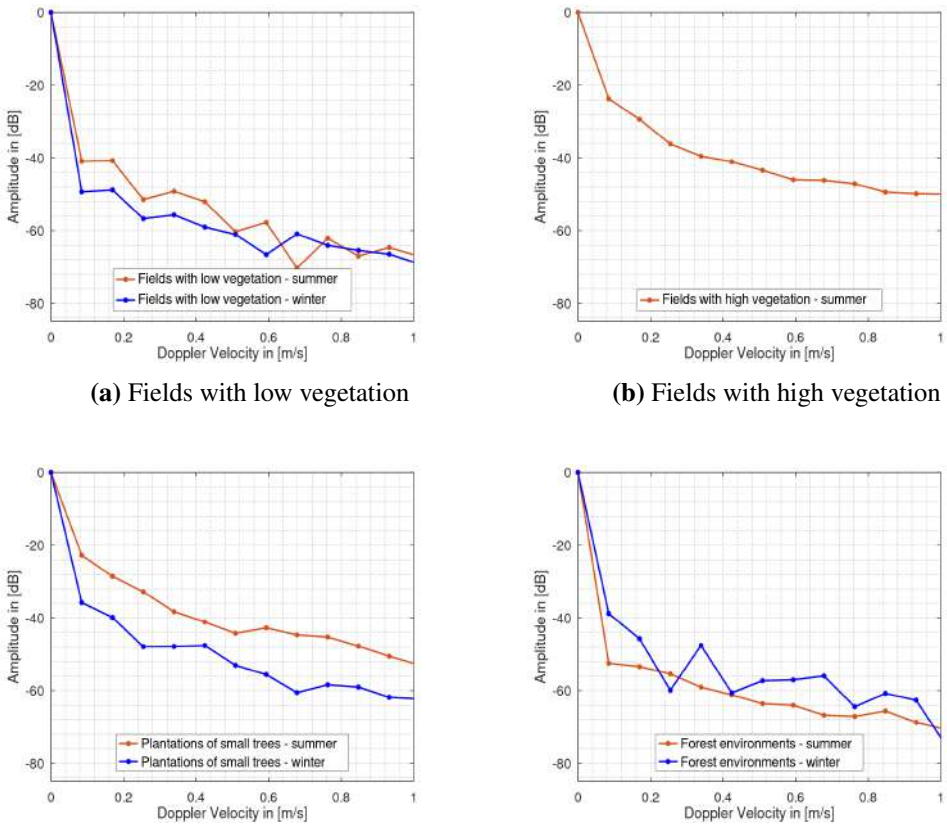

(a) Fields with low vegetation

(b) Fields with high vegetation

(c) Plantations of small trees

(d) Forest environments

Figure 7.22: Single-sided Doppler spread spectra for (a) fields with low vegetation, (b) fields with high vegetation, (c) plantations of small tress and (d) forest environments in summer and winter.

7.2.7 Doppler Coherent and Diffuse Component Models

According to the author in [54], the Doppler characteristics consists of two essential components: The coherent and the diffuse component, according to Figure 7.23. The coherent as well as the diffuse component can also be identified within the single-side Doppler spectra plots for the different rural terrain types in Figure 7.22. The coherent components are generated by strong scatterers that move hardly or only minimally. In the example of forests or plantations of small trees, this could be the trunks of individual trees. These form a large back-scatter area with minimal movement. The diffuse component on the other hand is created by fast moving scatterers with a much smaller back-scattering area. As an example, the leaves and branches of the trees are to be mentioned here. These move even at low wind speeds and lead to corresponding signal components in the Doppler spectrum. According to the author, this can be seen in Figure 7.21c. For example, in summer the plantations of small trees are covered with many small leaves that can produce such a diffuse component. In winter this component is reduced in amplitude due to the lack of biomass. The branches and twigs that are still present during this time of the year then produce fewer signal components.

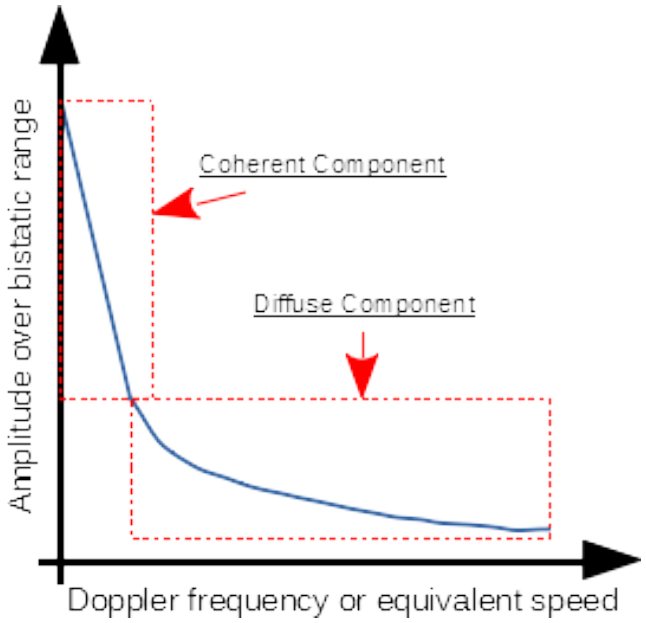

Figure 7.23: Coherent and diffuse Doppler components.

In order to be able to describe the Doppler characteristic analytically, a mathe-

matical model was defined for the coherent and diffuse components. The coherent component is linearly approximated. The diffuse component is described using an exponential model. In this thesis, the coherent component model describes the linear behaviour of the coherent Doppler spread component from 0 $\frac{m}{s}$ to 0.08 $\frac{m}{s}$. The coherent amplitude model is defined as follows:

$$A_{coherent}(v) = -\frac{m_{Damping}}{0.08 \ \frac{m}{s}} v \tag{7.1}$$

where $m_{Damping}$ is the corresponding damping factor or the slope of the linear regression and v the corresponding Doppler velocity, within the aforementioned range. The damping factors for the rural terrains, both during summer and winter, are listed in Table 7.5.

It can be seen that fields with low vegetation show a more narrow coherent component compared to the other terrain types. The reduced vegetation of this type of terrain offers fewer scatterers which could become visible in the Doppler spectrum due to movements e.g. in the wind. However, there is a difference between summer and winter. A possible explanation would be the further reduced vegetation during the winter season. As expected, the other types of terrain cause a significantly larger Doppler spread due to their biomass. The coherent components are correspondingly flatter. Forests are an exception. A very narrow coherent component, with -52.06 dB damping factor in summer, can be seen here. As already mentioned, the trunks of the individual trees could be a possible explanation. According to Table 7.5, the lowest attenuation factors are found for fields with low vegetation with and plantations of small trees during summer measurements. As already mentioned, both types of terrain have a strong back-scatter due to their vegetation. Large parts of this are hardly moving wooden components like tree trunks and fast moving parts like leaves and branches.

For the analytical description of the diffuse component, Doppler amplitudes caused by environmental movements, the following exponential model function was chosen:

Terrain Under Test	$m_{Damping}$
Fields with low vegetation - summer	-40.9
Fields with low vegetation - winter	-49.3
Fields with high vegetation - summer	-23.7
Plantations of small trees - summer	-22.74
Plantations of small trees - winter	-35.78
Forest environment - summer	-52.06
Forest environment - winter	-38.79

Table 7.5: Descriptive statistical properties of the clutter amplitudes for the different terrain types during summer and winter.

$$A_{diffuse}(v) = A + Be^{-Cv} \tag{7.2}$$

where the parameters have to be estimated are A,B and C. The Doppler frequency or equivalent speed in $\frac{m}{s}$ is marked with v. The model parameters have been estimated numerically. Therefore, a non-linear least-square fitting with 400 iterations has been performed. The resulting parameter estimations for the model function are listed in Table 7.6. Forest environments show a clear difference between summer and winter vegetation. During winter, the diffuse component is much more pronounced. Here too, the fact of the strong attenuation could play a significant role. During winter, the signal attenuation is lower in forest environments compared to summer season due to the decreased proportion of foliage. Since the surveyed forest environments are mixed forests, there are still many trees with corresponding vegetation, such as fir trees, which continue to produce a Doppler component also during the winter season.

The presented model parameters describe the bistatic Doppler spread, caused

Terrain Under Test	A	B	C
Fields with low vegetation - summer	-79.39	51.72	-1.26
Fields with low vegetation - winter	-74.22	54.87	-2.998
Fields with high vegetation - summer	-72.04	48.58	-0.7039
Plantations of small trees - summer	-72.58	51.62	-0.7511
Plantations of small trees - winter	-72.26	51.11	-1.623
Forest environment - summer	-80.57	53.92	-2.035
Forest environment - winter	-61.1	59.66	-9.314

Table 7.6: Non-linear least square estimation of the exponential model function parameters for the diffuse Doppler component.

by the different rural environments for the summer and winter vegetation. The models are only valid within the presented velocity range due to the fact, that the measurements have been carried out during calm weather with windspeed below 7 $\frac{km}{h}$. Additional measurements have to be carried out in order to also derive more generic model functions for broader velocity ranges.

7.2.8 Clutter Doppler-Zero Characteristics

Within the range-Doppler domain, the Doppler-zero line represents all stationary clutter scatterers. In each range cell, the respective back-scattered power is accumulated over all illuminated bistatic angles and scatteres. Since the bistatic measurements were carried out in such a way that it could be ensured in each case that only the terrain under test was illuminated, it can be assumed that only the back-scattered power by the vegetation is present in the corresponding range cells. The Doppler-zero line is therefore an ideal indicator for the attenuation behaviour of a certain terrain type. The Doppler-zero lines are presented over a bistatic range of 500 m.

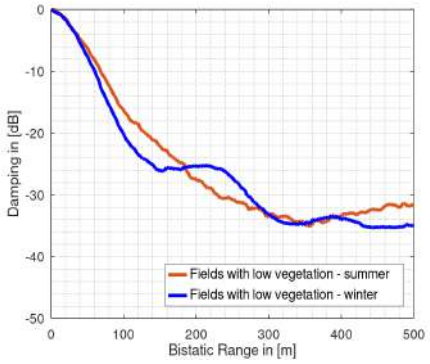

(a) Fields with low vegetation

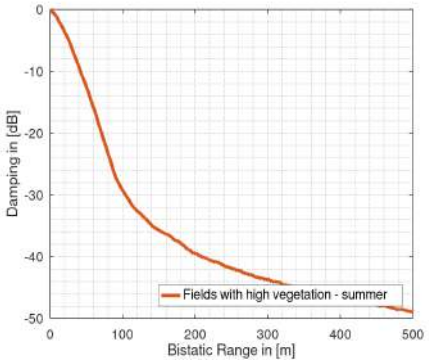

(b) Fields with high vegetation

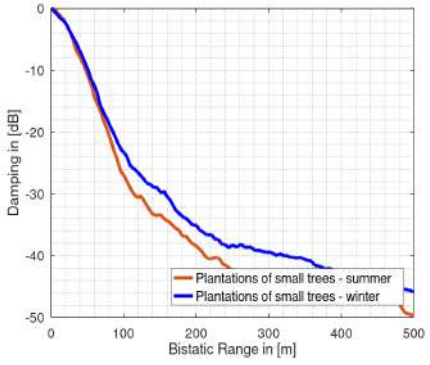

(c) Plantations of small trees

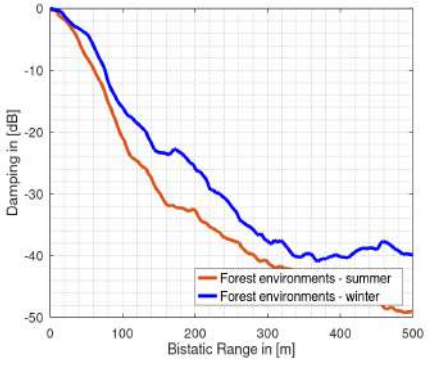

(d) Forest environments

Figure 7.24: Doppler-zero line characteristics, accumulated over all measured bistatic angles, for (a) fields with low vegetation, (b) fields with high vegetation, (c) plantations of small tress and (d) forest environments in summer and winter.

However, it is not possible to derive a generally valid damping factor directly from it. This would require further measurements at the same bistatic angles and different distances to a specific clutter patch. A measuring effort that should not be underestimated.

Figure 7.24 shows the Doppler-zero lines for each rural type of terrain and season. Figure 7.24a shows the Doppler characteristics for fields with low vegetation. As could already be seen in the evaluations for the detection performance, this type of terrain experiences the lowest attenuation in the considered bistatic range. However, it must be taken into account that due to the hardware used and the bistatic geometry, a strong direct signal component was present during the measurements and therefore the data for this type of terrain could be falsified. In the other types of terrain, a stronger decrease of the Doppler-zero line is visible, especially during summer measurements as shown in Figure 7.24b - 7.24d. Here, the existing biomass could be responsible for this. For plantations and forests, it can be seen that the attenuation is lower in winter. As the number of leaves is reduced during this season, this could be a possible explanation.

The lowest attenuation per meter results for fields with low vegetation. The damping factors in summer and winter are comparable. For the other types of terrain, the damping factors in summer are significantly higher. These are then reduced again in winter due to the lack of biomass.

With the presented linear approximations of the Doppler-zero line characteristics for a bistatic range up to 300 m it can be seen that with increasing vegetation and biomass an increasing signal attenuation is associated. This additional signal attenuation can also be measured for plantations of small trees and forest environments during the winter season, according to the presented values. However, the attenuation factor is reduced compared to the summer season, which may be due to the reduced biomass.

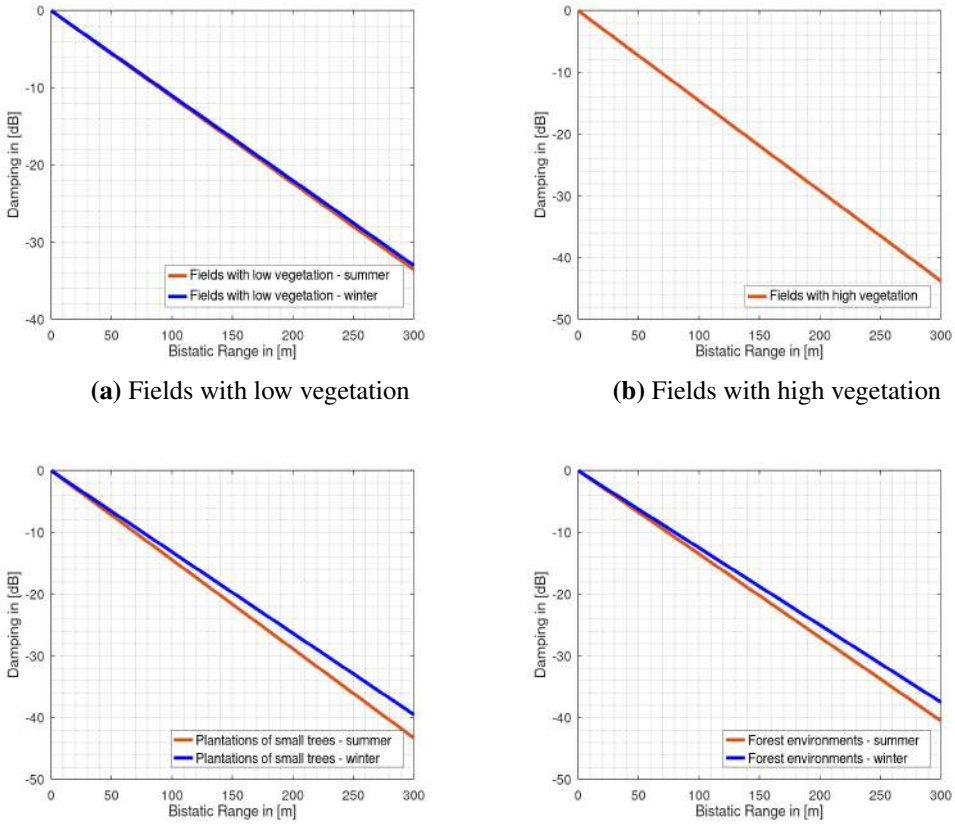

(a) Fields with low vegetation

(b) Fields with high vegetation

(c) Plantations of small trees

(d) Forest environments

Figure 7.25: Linear regression of the Doppler-zero lines over a bistatic range of 300 , for (a) fields with low vegetation, (b) fields with high vegetation, (c) plantations of small tress and (d) forest environments in summer and winter.

Terrain Under Test	Terrain Damping Factor
Fields with low vegetation - summer	-0.335 $\frac{dB}{m}$
Fields with low vegetation - winter	-0.323 $\frac{dB}{m}$
Fields with high vegetation - summer	-0.437 $\frac{dB}{m}$
Plantations of small trees - summer	-0.433 $\frac{dB}{m}$
Plantations of small trees - winter	-0.395 $\frac{dB}{m}$
Forest environment - summer	-0.405 $\frac{dB}{m}$
Forest environment - winter	-0.375 $\frac{dB}{m}$

Table 7.7: Linear approximated damping factors for the different rural terrain types and seasons.

7.3 Critical Discussion

The clutter statistics presented in this chapter were derived from the processed range-Doppler maps. However, only those range-Doppler bins corresponding to a bistatic angle range from 60° to 80° were considered accumulated. Thus, the presented results can only be considered valid for this angular range. The measurements were performed at selected locations for the different terrain types to ensure that the given beamwidths illuminate the corresponding terrain within this range. However, it should be mentioned that signal components outside the 3 dB beamwidths are of course also present. For this purpose, the areas were selected in such a way that adjacent areas were of the same terrain type. With higher transmit power also larger bistatic baselines would be possible and also larger patches could be illuminated. In that case it would be interesting to see if the statistics of mixed terrain types e.g. fields with high vegetation and plantations of small tress can be derived from the convolution of their individual densities. Of particular interest would be the influence of the bistatic angle on the backscattered magnitudes. The density functions shown represent the short term stability of the clutter amplitudes. It would also be interesting to make a long-term recording and to investigate the long-term statistical behaviour behavior. This was not possible with the available oscilloscope due to limited memory depth. According to the log likelihood optimization a best-fit of the density functions by means of a Weibull distribution was shown, which allows a synthesis of the clutter data for the selected parameters. The presented correlation analysis has shown that unique correlation properties can be used for a classification of the terrain types. This could be of particular interest for radar applications, in which an adaptive response to the prevailing environmental conditions is required and an adaption of the parameters could be performed. The presented results for the Doppler characteristics are also valid only for a bistatic angular range from 60° to 80° due to the mentioned reasons. Here, finer frequency resolution through longer sampling would be of interest in future studies. The presented data are mean-adjusted to make the different free-space damping effects due to the geometries, which vary depending on the type of terrain, more comparable.

Thus, the complexity of clutter measurements becomes apparent once again. This thesis therefore only offers comparable results for the set of parameters described here and thus serves as a template for further work. It would also be interesting to compare the results with larger bistatic baselines in order to validate the generality of the presented results.

Chapter 8

Discussion

In this thesis, statistical analysis of bistatic radar rural ground clutter for different terrain types under grazing angles below 5° and for a bistatic angle range from 60° to 80° is presented. The main novelty in this work is the separated statistical evaluation based on real measurement data of the clutter properties for different terrain subgroups forming a typical German rural environment, together with a dual-channel bistatic measurement setup with improved coherent range-Doppler processing. The results presented thus make a significant contribution to the field of bistatic ground clutter analysis of rural terrains for the frequency range from 8 GHz to 12 GHz, for which there are currently very few published results. The selected dominant types of terrain are fields with low vegetation, fields with high vegetation, plantations of small trees and forest environments. The group of fields with low vegetation includes terrain types such as meadows or farmland. The group of fields with high vegetation includes wheat or cornfields, for example. Plantations of small trees are the group consisting of environments such as fruit tree plantations, vineyards or other arrangements of smaller trees. Forests form the last rural subgroup. Additionally, the characteristics are described for different seasons, namely summer and winter. For each terrain group, bistatic radar measurements have been carried out in the Eifel region in western Germany in the summer 2019 and winter 2019/2020 using a bistatic radar setup developed by Fraunhofer FHR. The data from the individual measurements were processed, and the averaged statistical properties and characteristics are presented.

The histogram figures for the group of fields with low vegetation shows a skewness to the right both for the summer and winter measurement data. This is also indicated by the unbiased skewness value of $s = -0.98$ for the summer and -0.11 for the winter measurement data, whereas all other types of terrain show a positive value. The kurtosis remains approximately the same with the values 1.7 and 1.3. The cumulative distribution for this terrain also shows a clear shift compared to the other terrain types by nearly 10 dB, also again for the summer and winter, whereas the shift is less noticeable in winter. The standard deviation with $\sigma = 11.8\,dB$ for the summer is only reduced to $10.1\,dB$ compared to the winter measurements while the interquartile range is increased by nearly 3 dB. This behaviour is in contrast to the other types of terrain where the standard deviation generally increases in winter, whereas the IQR increases also for all other types of terrain. For the other groups, these changes are greater. However, bistatic measurements in such environments with low vegetation suffer from a strong direct signal component arriving at both receive channels. A reduction in detection performance is then probably mainly due to the direct signal instead of the clutter caused by the low vegetation. Since the current setup does not have an automatic gain control an optimal dynamic range of the analog-to-digital converter is not guaranteed. For this reason, the validity of the determined parameters for this terrain cannot be confirmed and thus may explain the behaviour of the standard deviation. Corresponding work on the hardware is part of our future work.

The histogram plots for the remaining environments are all shifted to the left around the histogram mean value also both for summer and winter measurement data while the shift slightly decreases for the winter measurements. With a value of 0.98, the skewness is much more dominant for the plantations of small trees in the summer compared to the other terrain types. This is also the case for the kurtosis with a value of 4.4. The values for skewness and kurtosis are the highest in the data compared to the other types of terrain. This indicates a lower dynamic range

because the amplitude values are strongly concentrated which may be due to the nature of this vegetation, which consists mainly of small leaves with high water content and dense vegetation with branches. The standard deviation and the IQR show the lowest value with 6.2 dB and 6.3 dB respectively for both summer and winter measurements. Since both values can be regarded as an indicator for the dynamic range, it can be seen that the plantations lead to significant signal attenuation and less dynamic range, especially in the summer when the trees are covered with water-filled leaves or fruits.

For the fields with high vegetation, the standard deviation shows a similar behaviour as the plantations with only a difference of 1.7 dB. However, the IQR of 11.2 dB is significantly higher and thus as high as for forest environments. Together with a value of 0.5 for the kurtosis, this indicates a high dynamic range of the clutter values. This can also be seen by the flattened histogram plot. A possible cause could be movements of the vegetation itself e.g. grain plants in the wind, resulting in a greater amplitude spread. The dynamic range for the forest environments is also with a value of 11.1 dB in the summer and 14.4 dB in the winter significantly higher compared to the other terrain types. It can be noted, although the plantations and forests consist mainly of trees, they differ significantly in the dynamic range of the clutter. A possible explanation could be that the plantations have a much denser vegetation and thus fewer multipath propagation are formed.

As aforementioned for all terrain types, except for the fields with low vegetation, an increase in the standard deviation from the summer to the winter statistics is visible and a respective shift of their cumulative figures. For plantations, the increase in the standard deviation is greatest with a value of 2.8 dB. This could be due the fact that the plantation trees are covered with many smaller, thicker leaves in summer, while these are missing in winter. As a result, considerably more propagation paths are formed which could lead to this higher value. This effect can also be seen with IQR value that has increased by almost 4 dB compared to the summer measurements. The clutter amplitudes for the forest environments also show the same behaviour,

although the increase in standard deviation and IQR of about 1.7 dB and 3 dB is lower but the total values are still higher. Again, the low number of leaves in winter is a possible explanation for the increase. For both types of terrain, this behaviour can also be seen from their distribution figures which shows the largest differences between the summer and winter data. Similar results were achieved for forest environments in monostatic applications [46].
For all types of terrain, there is a decrease in kurtosis values from summer to winter. This decrease is again particularly strong for forests and plantations of small trees with 4.4 and 2.3 in the summer compared to 1.64 and 0.33 in the winter respectively. However, this result is in line with the increase of the standard deviation and the increase of the IQR. As the clutter amplitudes are distributed over a larger amplitude range in the data for the winter measurements, the histograms have to be flattened which leads to a reduced kurtosis.

Interestingly, all terrain types, except the fields with low vegetation show a shift of their cumulative figures to the right in the winter compared to the data collected in summer. As mentioned the fields with low vegetation, however, have the largest offset with more than 10 dB compared to other measurements but show a similar density function for summer and winter. This could be due to the fact that the differences in vegetation between summer and winter is very small for fields with low vegetation, whereas all other types of terrain show significant differences in vegetation. Correlation analysis has shown that fields with low vegetation in summer and in winter correlate most clearly with a PCC of 0.78. Terrain with trees also showed a strong correlation with a PCC of 0.84. However, in winter it was no longer possible to clearly distinguish a plantation with small trees from a forest environment.

The analytical description of the clutter density functions and cumulative distribution functions was presented using a Weibull distribution according to a goodness-of-fit analysis compared to the Rayleigh distribution. The scale and

shape parameters necessary for the model description were determined by means of a maximum-likelihood estimation. The resulting clutter probability density functions clearly show the similarity of fields with low vegetation both in summer and winter. This could be mainly due to the generally low vegetation in this type of terrain at both seasons. However, the plantations of small trees and forest environments show significant differences between summer and winter measurements. The density functions in winter are widened and flattened compared to the statistics in summer. The corresponding CDF's confirm this behaviour. Here, a shift of the model function towards lower attenuation values is visible in the mentioned terrain types during the winter season. Here, too, the lower biomass in winter could be a possible explanation.

The evaluation of the Doppler spectra for the different terrain types shows a particularly dominant Doppler spectrum for fields with high vegetation. For plantations of small trees and forest environments a dominant Doppler spread is also visible. Here, it is mainly due to the moving leaves and branches that provide the corresponding signal components. In winter, a decrease in the strength of the Doppler spread can be seen in plantations of small trees. Possibly due to the missing leaves in this season. In contrast, the forest environments show a very dominant Doppler spectrum even in winter. This could be due to the fact that the measured forest environments are mainly mixed forests, which have a high biomass in summer and winter (”evergreen”). In forest environments in summer, the most dominant coherent Doppler components occurred with a slope of $\frac{-52.06dB}{0.08\frac{m}{s}}$. Presumably due to the tree trunks that cause the corresponding reflections. The Doppler-Zero line as an indicator for the damping properties of the different types of terrain shows the strongest damping behaviour for plantations of small trees and forest environments which is reduced in winter. These dominant characteristics significantly influence the detection performance as shown in the four separate investigations on the detection of a quadrocopter.

However, it must be noted that in this survey the different types of terrain were only measured over an averaged bistatic angle range of 60° - 80° and a grazing angle below 5°. It should be noted again that the presented results are only valid for the measurement parameters used. More reliable statements can only be made by further measurements at different aspect angles and parameter sets. This circumstance is in contrast to a not inconsiderable measurement effort. In addition, for fields with low vegetation there is the problem of strong direct signal components in the radar data. A falsification of the results cannot be excluded. In the future work it is planned to place the bistatic receiver on a moving platform [90] to cover a wide range of aspect angles by driving along the different terrain types if possible due to their accessibility. A similar measuring principle is known from the field of antenna measurement, where any spatial points can be measured. Furthermore, the measurements in forest environments were limited by the limited transmission power. This environment had the strongest attenuation effect and further measurements with the corresponding transmission power would have to be performed to verify the results. In general it must be noted, that bistatic clutter measurements are influenced by an enormous amount of parameters. Within the scope of a single PhD thesis a holistic description is not possible. Nevertheless, the results presented here can be the basis for further analysis.

Chapter 9

General Conclusions and Outlook on Future Work

This thesis presents a novel country-specific investigation of bistatic ground clutter in rural environments for the radar-relevant X-band and low grazing angles. In the field of bistatic ground clutter analysis for these types of terrain and especially the frequency range from 8 GHz to 12 GHz, there is currently very little available data from published evaluations compared to numerous monostatic studies. The important research questions posed at the beginning could be answered and the results presented in this thesis, therefore, have a significant impact on this research topic.

The bistatic ground clutter analysis is presented country-specific for German and Central European rural environments. Instead of considering the clutter characteristics for the rural environment as a whole, this paper presents the results for a division of landscapes into four dominant rural subgroups. The types of terrain analyzed are fields with low vegetation, fields with high vegetation, plantations of small trees, and forest environments. Fields with low vegetation are terrain consisting mainly of meadows or farmland. The group of fields with high vegetation is made up of agricultural areas such as corn or grain fields. Plantations of small trees represent fruit orchards or vineyards, while the forest environments are mixed forests.

The characteristic clutter properties of these four rural terrain types were worked out in numerous bistatic clutter measurements and presented here. The results are considered separately for the vegetation in summer and winter. During summer 2019 and winter, 2019/2020 measurements were carried out in the individual terrain types using a developed measuring setup and methodology. The measurements were performed for low grazing and scattering angles. This angle range is relevant for ground-based bistatic radar applications but also for other relevant bistatic applications such as imaging bistatic radar. A dual-channel bistatic measurement setup was used to perform the measurements. This is characterized by a phase coherence of the transmitting and receiving unit using an external reference signal. This allows free positioning of the transmitter and receiver unit without the need of a physical connection of the two.

The influence of the clutter properties of the different terrain types on the detection performance of a bistatic setup was shown. Especially plantations and forests were characterized by low detection performance. The statistical properties of these terrain types showed clear differences compared to fields with low and fields with high vegetation. The highest attenuation values over the bistatic range measured and Doppler-spread could be determined. A circumstance which is due to the vegetation, which mainly consists of trees. Due to the many small dense leaves and branches, there is a strong absorption. The moving scatterers also lead to a correspondingly pronounced Doppler spread which can mask weak object reflections and thus reduce the detection performance. In winter, the corresponding clutter amplitude distributions show a significant difference compared to summer for these terrain types. The same applies to the Doppler characteristics due to the reduced vegetation. Interestingly, fields with low vegetation behave similarly in der amplitude characteristics in summer and winter. The Weibull distributions do not indicate significant differences. Fields with high vegetation also show a distinct Doppler-spectrum which can lead to object masking. Especially maize or cereal fields with their plants influenced by the wind in the movement are responsible for this. This type of terrain also has the lowest extreme value statistics in terms

of dynamics, compared to the other types of terrain. Together with the moderate attenuation properties, this type of terrain had the least influence on the detection performance.

Correlation analysis confirms a significant difference in fields with low vegetation compared to plantations of small trees and forest environments. The latter two, however, show a strong correlation. This could be due to the fact that both types of land are mainly composed of trees or plants with high wooden content. The respective types of terrain also showed strong correlations between the respective seasons. These were most pronounced for fields with envious vegetation. The unique correlation properties can be used, among other things, to classify the types of terrain. Interesting applications here are CFAR applications which can achieve a corresponding increase in detection performance with a priori knowledge of the clutter distribution of the terrain types. Also adaptive radar applications are of great interest here. Knowing the prevailing terrain would give the radar the opportunity to adapt its parameters to it e.g. longer integration time or a change of PRF. In this thesis, analytical models for the rural bistatic ground clutter density functions and distributions in the form of Weibull distributions, the Doppler-spread characterization via exponential models and the Doppler-zero line properties derived from the measured data via linear models are also presented. The data basis for all evaluations were the bistatic range-Doppler domain data, which were collected using the newly developed measurement methodology.

The findings presented here provide an important contribution for further investigations due to the very small amount of data available from published bistatic ground clutter analyses for the X-band. The results obtained are also of great interest for future applications in the field of adaptive detection, such as knowledge-aided space-time adaptive processing (STAP), since the clutter signal space can be modeled accordingly, rather than assuming homogeneous environments [41]. This also includes general detectors based on hypothesis testing, for example, since the

disturbance in the form of the environmental clutter can be better modeled by such statistical models and thus leading to an increase in detection performance [42].

In future work, the bistatic measurement campaigns will be continued to investigate other environmental influences such as rain and snow, but also other types of terrain such as built-up land, on the clutter properties in the frequency and angle range investigated here. In addition, changes will be made to the hardware to ensure more efficient suppression of the direct signal component. This problem was especially apparent in fields with low vegetation and correspondingly low terrain attenuation.

Appendix A

Terrain Under Test	Minimum	1st Quartile	2nd Quartile	3rd Quartile	Maximum
Fields with low vegetation - summer	-46.4 dB	-3.5 dB	2.1 dB	7.3 dB	36.6 dB
Fields with low vegetation - winter	-45.4 dB	-6.5 dB	-0.5 dB	6.6 dB	32.9 dB
Fields with high vegetation - summer	-15.6 dB	-6.1 dB	-1.4 dB	5.1 dB	28.6 dB
Plantations of small trees - summer	-17.0 dB	-3.2 dB	-0.1 dB	3.0 dB	32.4 dB
Plantations of small trees - winter	-23.2 dB	-5.7 dB	-0.7 dB	4.3 dB	32.2 dB
Forest environment - summer	-25.7 dB	-5.9 dB	-0.6 dB	5.0 dB	43.9 dB
Forest environment - winter	-31.7 dB	-7.3 dB	-2.3 dB	7.0 dB	33.0 dB

Table A.1: Statistical properties of the box-plots for the clutter amplitudes of the different terrain types during summer and winter measurements.

Appendix B

Colophon

This thesis has been written in LaTeX. The presented figures have been created with either MATLAB/Octave, which is especially true for presented results, Inkscape and GIMP.

Bibliography

[1] Michael Kohler, Daniel W. O'Hagan, Matthias Weiss, David Wegner, Josef Worms, and Oliver Bringmann. Statistical analysis of bistatic radar ground clutter for different german rural environments. *Sensors*, 20(11):3311, Jun 2020.

[2] M. Ummenhofer, M. Kohler, J. Schell, and D. W. O'Hagan. Direction of arrival estimation techniques for passive radar based 3d target localization. In *2019 IEEE Radar Conference (RadarConf)*, pages 1–6, 2019.

[3] M. Kohler, A. Saam, J. Worms, D. W. O'Hagan, J. Novacek, and O. Bringmann. Delay estimation for time synchronization of a bistatic transfer function measurement setup to single received pulses. In *2019 Signal Processing: Algorithms, Architectures, Arrangements, and Applications (SPA)*, pages 62–66, 2019.

[4] M. Kohler, M. Weiss, A. Saam, J. Worms, D. W. O'Hagan, and O. Bringmann. External timebase trials for phase coherency of a bistatic transfer function measurement setup. In *2019 Signal Processing Symposium (SPSympo)*, pages 319–322, 2019.

[5] M. Kohler, V. Duk, M. Weiss, J. Worms, J. Schell, D. O'Hagan, and O. Bringmann. Statistical analysis of bistatic rural terrain clutter. In *2020 21st International Radar Symposium (IRS)*, pages 205–210, Oct 2020.

[6] M. Kohler, V. Duk, M. Weiss, W. Brodowski, J. Worms, D. O'Hagan, and O. Bringmann. A multifunctional broadband receiver for bistatic x-band radar

measurements. In *2020 IEEE International Radar Conference (RADAR)*, pages 918–922, 2020.

[7] the free encyclopedia Wikipedia. *Christian Hülsmeyer*, 2019 (accessed July 10, 2020).

[8] L. M. H. Ulander, P. Frölind, A. Gustavsson, R. Ragnarsson, and G. Stenström. Vhf/uhf bistatic and passive sar ground imaging. In *2015 IEEE Radar Conference (RadarCon)*, pages 0669–0673, 2015.

[9] M. Malanowski, R. Haugen, M. S. Greco, D. W. O'Hagan, R. Plšek, and A. Bernard. Land and sea clutter from fm-based passive bistatic radars. *IET Radar, Sonar Navigation*, 8(2):160–166, 2014.

[10] Fabiola Colone, DW O'hagan, P Lombardo, and CJ Baker. A multistage processing algorithm for disturbance removal and target detection in passive bistatic radar. *IEEE Transactions on Aerospace and Electronic Systems*, 45(2):698–722, 2009.

[11] C. J. Baker, H. D. Griffiths, and I. Papoutsis. Passive coherent location radar systems. part 2: waveform properties. *IEE Proceedings - Radar, Sonar and Navigation*, 152(3):160–168, 2005.

[12] Z. Geng, R. Xu, and H. Deng. Lte-based multistatic passive radar system for uav detection. *IET Radar, Sonar Navigation*, 14(7):1088–1097, 2020.

[13] D. W. O'Hagan and C. J. Baker. Passive bistatic radar (pbr) using fm radio illuminators of opportunity. In *2008 New Trends for Environmental Monitoring Using Passive Systems*, pages 1–6, 2008.

[14] C. B. Barneto, L. Anttila, M. Fleischer, and M. Valkama. Ofdm radar with lte waveform: Processing and performance. In *2019 IEEE Radio and Wireless Symposium (RWS)*, pages 1–4, 2019.

[15] T. Van Cao, T. Vu, M. Byrne, N. Dahal, P. E. Berry, A. B. Iji, D. Gustainis, M. Ummenhofer, and M. Kohler. Beamforming and tracking assessment with

passive radar experimental data. In *2020 IEEE International Radar Conference (RADAR)*, pages 49–54, 2020.

[16] Z. Geng, R. Xu, and H. Deng. Lte-based multistatic passive radar system for uav detection. *IET Radar, Sonar Navigation*, 14(7):1088–1097, 2020.

[17] Weike Feng, Jean-Michel Friedt, Giovanni Nico, Suyun Wang, Gilles Martin, and Motoyuki Sato. Passive bistatic ground-based synthetic aperture radar: Concept, system, and experiment results. *Remote Sensing*, 11(15):1753, Jul 2019.

[18] M. Yusuf, B. D. Beelde, E. Tanghe, E. D. Poorter, L. Martens, P. Laly, D. P. Gaillot, M. Liénard, and W. Joseph. Estimation of the number of persons in a reverberant environment using bistatic radar. In *2020 14th European Conference on Antennas and Propagation (EuCAP)*, pages 1–5, 2020.

[19] Y. Quan, L. Shi, J. Liu, and J. Ma. A novel bistatic joint radar-communication system in multi-path environments. In *2020 12th International Conference on Communication Software and Networks (ICCSN)*, pages 186–191, 2020.

[20] P. B. Cox and W. L. van Rossum. Analysing multibeam, cooperative, ground based radar in a bistatic configuration. In *2020 IEEE International Radar Conference (RADAR)*, pages 912–917, 2020.

[21] H. Xie, K. Duan, J. Hu, Z. Chen, S. Xu, Y. Lin, N. Zhu, B. Xi, D. An, and G. Wang. Monostatic and bistatic experiment with airborne uhf ultra-wideband sar system. In *2019 IEEE Asia-Pacific Microwave Conference (APMC)*, pages 830–832, 2019.

[22] M. Rodriguez-Cassola, S. V. Baumgartner, G. Krieger, and A. Moreira. Bistatic terrasar-x/f-sar spaceborne–airborne sar experiment: Description, data processing, and results. *IEEE Transactions on Geoscience and Remote Sensing*, 48(2):781–794, 2010.

[23] Ingo Walterscheid, Thomas Espeter, Jens Klare, and Andreas Brenner. Bistatic spaceborne-airborne forward-looking sar. pages 1–4, 01 2010.

[24] Z. Zhu and F. Xu. A high resolution imaging method for target using multi-static multi-frequency radar. In *2018 China International SAR Symposium (CISS)*, pages 1–3, 2018.

[25] M. Weiß, S. Sandenbergh, F. Valdes, P. Müller, D. Bok, M. Kohler, D. O'Hagan, and P. Knott. Aspects of next generation sensor/radar networks. In *2019 20th International Radar Symposium (IRS)*, pages 1–8, 2019.

[26] K. L. Scherer, S. J. Watt, E. A. Alwan, A. A. Akhiyat, B. Dupaix, W. Khalil, and J. L. Volakis. Simultaneous transmit and receive system architecture with four stages of cancellation. In *2015 IEEE International Symposium on Antennas and Propagation USNC/URSI National Radio Science Meeting*, pages 520–521, 2015.

[27] G. P. Blasone, F. Colone, P. Lombardo, P. Wojaczek, and D. Cristallini. A two-stage approach for direct signal and clutter cancellation in passive radar on moving platforms. In *2019 IEEE Radar Conference (RadarConf)*, pages 1–6, 2019.

[28] S. Björklund and A. Nelander. Fast-time stap for clutter suppression between transmitter and receiver in bistatic radar. In *2009 International Radar Conference "Surveillance for a Safer World" (RADAR 2009)*, pages 1–6, 2009.

[29] J. L. Garry, G. E. Smith, and C. J. Baker. Direct signal suppression schemes for passive radar. In *2015 Signal Processing Symposium (SPSympo)*, pages 1–5, 2015.

[30] R. G. Kulkarni. Design of windows for efficient spectral resolution and harmonic suppression [tips and tricks]. *IEEE Signal Processing Magazine*, 36(4):168–172, 2019.

[31] P. Xiao, W. Guo, Y. Wu, and B. Liu. A comprehensive method of ambiguity suppression for constellation of geostationary and low earth orbit sar. *IEEE Journal of Selected Topics in Applied Earth Observations and Remote Sensing*, 13:3327–3335, 2020.

[32] R.J. Doviak and D.S. Zrni. *Doppler Radar and Weather Observations*. Dover Books on Engineering Series. Dover Publications, 2006.

[33] J. Heckenbach, H. Kuschel, J. Schell, and M. Ummenhofer. Passive radar based control of wind turbine collision warning for air traffic parasol. In *2015 16th International Radar Symposium (IRS)*, pages 36–41, 2015.

[34] Matthew Ritchie, Francesco Fioranelli, Hugh D. Griffiths, and Borge Torvik. Monostatic and bistatic radar measurements of birds and micro-drone. *2016 IEEE Radar Conference (RadarConf)*, pages 1–5, 2016.

[35] Matthew Ritchie, Francesco Fioranelli, A. Balleri, and H.D. Griffiths. Measurement and analysis of multiband bistatic and monostatic radar signatures of wind turbines. *Electronics Letters*, 07 2015.

[36] Ajeet Vishwakarma and Rajenda Prasad. Bistatic specular scattering measurements for the estimation of rice crop growth variables using fuzzy inference system at x-, c-, and l-bands. *Geocarto International*, pages 1–15, 02 2019.

[37] A Pandey, A Srivastava, and VP Singh. Bistatic scatterometer monitoring of soil moisture by microwave remote sensing at x-band. *Russian agricultural sciences*, 43(5):440–444, 2017.

[38] Surajo Alhaji Musa, raja syamsul azmir raja abdullah, Aduwati Sali, Alyani Ismail, and Asem Salah. A review of copter drone detection using radar system. 12:16–38, 03 2019.

[39] N. S. Subotic, B. Thelen, K. Cooper, W. Buller, J. Parker, J. Browning, and H. Beyer. Distributed radar waveform design based on compressive sensing considerations. In *2008 IEEE Radar Conference*, pages 1–6, 2008.

[40] Y. Yang and R. S. Blum. Mimo radar waveform design based on mutual information and minimum mean-square error estimation. *IEEE Transactions on Aerospace and Electronic Systems*, 43(1):330–343, 2007.

[41] P. Wang, H. Li, and B. Himed. A bayesian parametric test for multichannel adaptive signal detection in nonhomogeneous environments. *IEEE Signal Processing Letters*, 17(4):351–354, 2010.

[42] D. Ciuonzo, D. Orlando, and L. Pallotta. On the maximal invariant statistic for adaptive radar detection in partially homogeneous disturbance with persymmetric covariance. *IEEE Signal Processing Letters*, 23(12):1830–1834, 2016.

[43] Melvin M Weiner and PD Kaplan. Bistatic surface clutter resolution area at small grazing angles. Technical report, Rome Air Development Center, Air Force Systems Command, Griffis Air Force Base, NY 13441, 1982.

[44] J. B. Billingsley, A. Farina, F. Gini, M. V. Greco, and L. Verrazzani. Statistical analyses of measured radar ground clutter data. *IEEE Transactions on Aerospace and Electronic Systems*, 35(2):579–593, 1999.

[45] JB Billingsley and John F Larrabee. Multifrequency measurements of radar ground clutter at 42 sites. volume 2. appendices a through d. Technical report, Massachusetts Institute of Technology, Lexington Linclon Lab, 1991.

[46] J Barrie Billingsley. *Low-angle radar land clutter: measurements and empirical models*. IET, 2002.

[47] M. Greco, F. Gini, A. Farina, and J. B. Billingsley. Validation of windblown radar ground clutter spectral shape. *IEEE Transactions on Aerospace and Electronic Systems*, 37(2):538–548, 2001.

[48] JB Billingsley and JF Larrabee. Measured spectral extent of l-and x-radar reflections from windblown trees. *Proj. Rep. CMT-57; DTIC AD-A179942*, 1987.

[49] J Barrie Billingsley. Exponential decay in windblown radar ground clutter doppler spectra: Multifrequency measurements and model. Technical report, Massachusetts Institute of Technology, Lexington Linclon Lab, 1996.

[50] P. Lombardo and J. B. Billingsley. A new model for the doppler spectrum of windblown radar ground clutter. In *Proceedings of the 1999 IEEE Radar Conference. Radar into the Next Millennium (Cat. No.99CH36249)*, pages 142–147, 1999.

[51] K. S. Chen and A. K. Fung. Frequency dependence of backscattered signals from forest components. *IEE Proceedings - Radar, Sonar and Navigation*, 142(6):301–305, 1995.

[52] Jen Jao. Amplitude distribution of composite terrain radar clutter and the k-distribution. *IEEE Transactions on Antennas and Propagation*, 32(10):1049–1062, 1984.

[53] J Barrie Billingsley. Radar ground clutter measurements and models. part 1. spatial amplitude statistics. Technical report, Massachusetts Institute of Technology, Lexington Linclon Lab, 1991.

[54] HC Chan. Spectral characteristics of low-angle radar ground clutter. Technical report, Defence Research Establishment Ottawa (Ontario), 1989.

[55] G. Zhu, Y. Chen, and H. Yin. Analiysis of typical ground clutter statistical characteristics. In *2017 International Applied Computational Electromagnetics Society Symposium (ACES)*, pages 1–2, 2017.

[56] K Rajalakshmi Menon, N Balakrishnan, M Janahraman, and K Ramchand. Characterization of fluctuation statistics of radar clutter for indian terrain. *IEEE Transactions on Geoscience and Remote Sensing*, 33(2):317–324, 1995.

[57] Fawwaz Ulaby, M Craig Dobson, and José Luis Álvarez-Pérez. *Handbook of radar scattering statistics for terrain*. Artech House, 2019.

[58] J. J. Strydom, J. J. de Witt, and J. E. Cilliers. High range resolution x-band urban radar clutter model for a drfm-based hardware in the loop radar environment simulator. In *2014 International Radar Conference*, pages 1–6, 2014.

[59] A. Melebari, M. Y. A. Gaffar, and J. J. Strydom. Analysis of high resolution land clutter using an x-band radar. In *2015 IEEE Radar Conference*, pages 139–144, 2015.

[60] Robert R Boothe. The weibull distribution applied to the ground clutter backscatter coefficient. Technical report, Army Missile Command Redstone Arsenal, Alabama, 1969.

[61] D. C. Schleher. Radar detection in weibull clutter. *IEEE Transactions on Aerospace and Electronic Systems*, AES-12(6):736–743, 1976.

[62] A. Melebari, A. K. Mishra, and M. Y. Abdul Gaffar. Statistical analysis of measured high resolution land clutter at x-band and clutter simulation. In *2015 European Radar Conference (EuRAD)*, pages 105–108, 2015.

[63] S. Cost. Measurements of the bistatic echo area of terrain of x-band. Technical report, Antenna Laboratory, Ohio State University, 1965.

[64] A.R. Domville. he bistatic reflection from land and sea of x-bandradio waves-part 1. Technical report, Stanmore, England, 1967.

[65] A.R. Domville. The bistatic reflection from land and sea of x-bandradio waves-part 2 supplement. Technical report, Stanmore, England, 1969.

[66] R. Larson, A. Maffett, R. Heimiller, A. Fromm, E. Johansen, R. Rawson, and F. Smith. Bistatic clutter measurements. *IEEE Transactions on Antennas and Propagation*, 26(6):801–804, 1978.

[67] F. T. Ulaby, T. E. Van Deventer, J. R. East, T. F. Haddock, and M. E. Coluzzi. Millimeter-wave bistatic scattering from ground and vegetation targets. *IEEE Transactions on Geoscience and Remote Sensing*, 26(3):229–243, 1988.

[68] Abishek Mohan. Bistatic radar land clutter characterization at x-band. 2015.

[69] N.J. Willis. *Bistatic Radar*. Artech House radar library. Institution of Engineering and Technology, 2005.

[70] D. M. Gould, R. S. Orton, and R. J. E. Pollard. Forward scatter radar detection. In *RADAR 2002*, pages 36–40, 2002.

[71] Bassem R Mahafza. *Radar signal analysis and processing using MATLAB*. CRC Press, 2016.

[72] Mark Richards. *Fundamentals of Radar Signal Processing*. 01 2014.

[73] N.J. Willis and H.D. Griffiths. *Advances in Bistatic Radar*. Electromagnetics and Radar. Institution of Engineering and Technology, 2007.

[74] Waddah Ali Mohammed Al-Ashwal. *Measurement and Modelling of Bistatic Sea Clutter*. PhD thesis, University College London, 2011.

[75] George U Yule. Notes of karl pearson's lectures on the theory of statistics, 1884-96. *Biometrika*, 30(1/2):198–203, 1938.

[76] P. Cabalkova, D. Kubal, and M. Pelant. Comparison of clutter cancelation methods. In *2014 24th International Conference Radioelektronika*, pages 1–4, 2014.

[77] V. Duk, D. Cristallini, P. Wojaczek, and D. W. O'Hagan. Statistical analysis of clutter for passive radar on an airborne platform. In *2019 International Radar Conference (RADAR)*, pages 1–6, 2019.

[78] J. Worms, S. Mayer, A. Saam, J. Schell, T. Mathy, S. Mueller, and C. Schumacher. Neue verfahren zur schätzung der signalparamter empfangener lpr-radare. Technical Report 102717, Fraunhofer FHR, March 2016.

[79] Analog Devices Walter Kester. *Taking the Mystery out of the Infamous Formula, SNR = 6.02N + 1.76dB, and Why You Should Care*, 2019 (accessed July 10, 2020).

[80] J. Balke. Sar image formation for forward-looking radar receivers in bistatic geometry by airborne illumination. In *2008 IEEE Radar Conference*, pages 1–5, 2008.

[81] J. R. Klauder, A. C. Price, S. Darlington, and W. J. Albersheim. The theory and design of chirp radars. *The Bell System Technical Journal*, 39(4):745–808, 1960.

[82] Rohde&Schwarz Michael Simon. *Interaction of Intermodulation Products between DUT and Spectrum Analyzer*, 2019 (accessed July 9, 2020).

[83] Stepan Matejka. Analysis of intermodulation distortion in ofdm based transmitter using eer technique. *Radioengineering*, 25:390–398, 04 2016.

[84] Joseph Garry, Graeme Smith, and C.J. Baker. Direct signal suppression schemes for passive radar. pages 1–5, 06 2015.

[85] Charles Knapp and Glifford Carter. The generalized correlation method for estimation of time delay. *IEEE transactions on acoustics, speech, and signal processing*, 24(4):320–327, 1976.

[86] Jinyong Lee, Jingu Lee, Youngseh Kim, Kanghoon Kim, and Younglok Kim. Low complexity frequency offset estimation for fmcw radar. In *Proceedings of the 2nd International Conference on Advances in Computer Science and Engineering (CSE 2013)*, pages 305–308. Atlantis Press, 2013/07.

[87] Matthias Weiß. Synchronisation of bistatic radar systems. In *IGARSS 2004. 2004 IEEE International Geoscience and Remote Sensing Symposium*, volume 3, pages 1750–1753. IEEE, 2004.

[88] M. Kohler, D. O'Hagan, J. Worms, and O. Bringmann. Empirical calibration coefficient estimation in the context of multi-functional rf systems. In *2020 IEEE Radar Conference (RadarConf20)*, pages 1–5, 2020.

[89] Natur-und Verbraucherschutz des Landes Nordrhein-Westfalen Ministerium für Umwelt, Landwirtschaft. *Landeswaldbericht 2019*, 2019 (accessed July 5, 2020).

[90] V. Duk, D. Cristallini, P. Wojaczek, and D. W. O'Hagan. Statistical analysis of clutter for passive radar on an airborne platform. In *2019 International Radar Conference (RADAR)*, pages 1–6, 2019.